# THE HIGH-TEMPERATURE, HIGH-PRESSURE HOMOGENEOUS WATER-GAS SHIFT REACTION IN A MEMBRANE REACTOR

by

**Felipe Bustamante-Londono**

B.S. in Chemical Engineering, Universidad de America, Colombia, 1993

M.Sc. in Chemical Sciences, Universidad de Antioquia, Colombia, 2000

Submitted to the Graduate Faculty of

The School of Engineering in partial fulfillment

of the requirements for the degree of

Doctor of Philosophy

University of Pittsburgh

2004

**UNIVERSITY OF PITTSBURGH**

**SCHOOL OF ENGINEERING**

This dissertation was presented

by

Felipe Bustamante-Londono

It was defended on

July 1, 2004

and approved by

Irving Wender, Professor, Chemical and Petroleum Engineering Department

Götz Veser, Professor, Chemical and Petroleum Engineering Department

Anthony Cugini, Professor, U.S. DOE National Energy Technology Laboratory

George Gallaher, Professor, Sunoco Chemical Company

Dissertation Director: Robert M. Enick, Professor, Chemical and Petroleum Engineering Department

**THE HIGH-TEMPERATURE, HIGH-PRESSURE HOMOGENEOUS WATER-GAS SHIFT REACTION IN A MEMBRANE REACTOR**

Felipe Bustamante-Londono, Ph.D.

University of Pittsburgh, 2004

The transition to a hydrogen economy requires substantial reductions in the cost of hydrogen. One alternative for achieving this goal is to conduct the water-gas shift reaction under the high temperature and pressure conditions present at the coal gasifier outlet. However, the equilibrium conversion of the water-gas shift reaction at such high temperatures is quite low. Even though the thermodynamic limitation can be overcome by the introduction of a $H_2$-selective membrane reactor, no previous studies of such a membrane reactor concept have been performed. The objective of this work is to provide the fundamental background required to determine whether the high-temperature, high-pressure water-gas shift reaction in a $H_2$-selective membrane reactor, despite its theoretical simplicity and potential advantages, is a viable way to enhance the hydrogen yield.

The gas-phase reaction kinetics were studied in the presence of an inert material (quartz), a common high-temperature construction material (Inconel®600) and potential membrane materials (Pd and a Pd-Cu alloy) in an effort to assess if the reaction can proceed at rates high enough to preclude the need for added catalysts. The gas-phase mechanism previously proposed

to describe the high-temperature, low-pressure reaction was found to be valid at high-pressure conditions. Inconel®600 surfaces greatly enhanced the reaction rate. This effect is likely attributable to the formation of a catalytic chromium oxide layer on the metal surface. Fresh Pd-Cu pellets and, also, Pd and Pd-Cu surfaces after exposure to reaction conditions followed by an oxygen treatment for carbon removal displayed catalytic activity for the water-gas shift reaction. However, the catalytic effect was not as significant as that observed with Inconel®600 surfaces. These results suggest that sufficiently large reaction rates can be attained without the need of an external catalyst.

Several Pd-based membrane reactor configurations were studied. The reaction was conducted in high-reaction rate / low-permeation rate (flat disk) and high-permeation rate / low-reaction rate (tubular) membrane reactor configurations. Conversions surpassing the equilibrium limitation were attained with both configurations. The two approaches are compared. It was found that the heat released by the reaction in the tubular configuration may have a significant, enhancing effect on the reaction conversions.

## TABLE OF CONTENTS

## LIST OF TABLES

## LIST OF FIGURES

## ACKNOWLEDGEMENTS

I would like to express my gratitude to my Thesis Advisor, Dr. Robert Enick, for his encouragement and guidance throughout the project. I wish also to acknowledge my committee members: Dr. Irving Wender and Dr. Goetz Veser for having pointed me in the right direction when I stumbled at the crossroads, Dr. Anthony Cugini for having asked the tough questions, and Dr. George Gallaher for many detailed and important discussions about my work.

This project would have not been accomplished without the unfaltering assistance of the people at the U.S. DOE National Energy Technology Laboratory: Dr. Bret Howard, who did not give up in the tiresome and discouraging task of teaching me something valuable each day, Mr. Bryan Morreale, for his outstanding common sense and mechanical skills, Mr. Richard Killmeyer and Dr. Michael Ciocco, for having made everything run smoothly. The help of Shaoping Shi from Fluent Inc. and William Rogers from NETL in implementing and running the CFD simulations is gratefully acknowledged. Finally, special thanks go to the technicians of Parsons Project Services Inc. for spending countless hours recording data and trying to bear with me.

I would have not come this far without the help and encouragement of my previous mentor, Consuelo Montes de Correa, who showed me the way. Many friends made my stay in

Pittsburgh unforgettable. It would be a lack of gratitude to neglect mentioning some of them. Yannick Heintz, John Harrold, Abhishek Soni, Dirk Neuman, Kunal Jain, Sudipta Chaddoppatoday, Eilis Rosenbaum, Heather MacPherson, … However, Watson Vargas deserves especial consideration because of his continuous willingness to help me out with any question and provide any possible type of support.

Nothing in my life would have come into reality without the human virtues I learned and borrowed from my parents. Any good that there is in my life comes from them. Thanks!

# 1.0 INTRODUCTION

U.S. dependence on oil imports is expected to grow from the current 55% level to 65% by 2025[1] reflecting an increasing demand for energy. The potential instability of Middle-Eastern regimes and the growing concern for a cleaner environment have motivated the quest for alternative energy carriers. Among them, hydrogen has two important advantages. Hydrogen is an extremely promising clean energy carrier because water would be the only by-product at the point-of-use, and any other by-products (e.g. $CO_2$) generated during its manufacture could be readily captured at the hydrogen generation facility. Further, hydrogen can be produced from a wide array of feed stocks available on American soil, including coal and renewable sources (e.g. biomass). The vision of a future where hydrogen is used as an energy carrier on the production of energy in a clean and efficient way is known as 'hydrogen economy'. In 2002 the U.S. Department of Energy convened the National Hydrogen Vision Meeting to discuss the building blocks of the roadmap towards a hydrogen economy. One of the major findings of the meeting was that "the transition toward a so-called 'hydrogen economy' has already begun. We have a hydrocarbon economy, but we lack the know-how to produce hydrogen from hydrocarbons and water, and deliver it to consumers in a clean, affordable, safe, and convenient manner as an automotive fuel or for power regeneration"[2]. Moreover, the implementation of the hydrogen economy is bound to require a significant increase in the supply of hydrogen. If all vehicles in

the Los Angeles area were to change to fuel-cell technology, for instance, they would consume the equivalent to 60% of the total hydrogen consumption in the U.S. during the year 2000[3].

At present, hydrogen is used primarily for the production of ammonia and in oil refinery operations. Virtually all the hydrogen is produced from fossil fuels (natural gas, petroleum, coal)[4] involving the production of a high-temperature CO-$H_2$ mixture which is then reacted with steam, i.e. by using the Water-Gas Shift Reaction, WGSR, Reaction (1-1)[5]. Methane is the preferred raw material, with 50% of the total production of hydrogen coming from this feedstock via Steam Methane Reforming[4]. Gasification of petroleum is the second major source of hydrogen, reflecting the large consumption of hydrogen in refineries. Coal gasification is restricted to places where coal is more abundant than natural gas, partly outweighing the lower cost of the latter[6]. However, the long term projection of the increasing price of natural gas as reserves dwindle coupled with the large coal reserves in the U.S. have initiated a renewed interest in the use of carbon as a transition step towards the hydrogen economy. Therefore, intense research has been devoted to the optimization of gasification technologies.

$$CO + H_2O \leftrightarrow CO_2 + H_2 \qquad \Delta H = -41 \text{ KJ/mol} \qquad (1\text{-}1)$$

Gasification has been commercially available since the introduction of the Winkler and Lurgi processes in the 1920s and 1930s. It consists of the reaction of coal or any other carbon-based material with steam at high pressure and temperature in an oxygen-deficient environment. The process normally operates at very high temperature and pressure, e.g. 1773 K and 2.8 MPa. The use of a catalyst is not always required. Major gasification plants are located in Southern

Asia (China) and South Africa. The effluent of the gasifier (e.g., 34% $H_2$, 48% CO, 17% $CO_2$, 1% $N_2$ –on a dry basis– in a Texaco gasification process[6]) is cooled down, desulfurized and sent to the water-gas shift reactors where the WGSR is conducted at moderate temperature. The low temperature operation (<723 K) is required because of the thermodynamic limitation at high temperature stemming from the exothermic nature of the reaction. Typically, two water-gas shift reactors are used. A "high-temperature" shift, employing an iron-chromium based catalyst is conducted at 593-723 K; the effluent of this reactor is cooled and fed to the "low-temperature" shift reactor (473-523 K), packed with a more active but less thermally-stable copper-zinc based catalyst. CO conversions over 90% are obtained[6]. Pressure Swing Adsorption, or cryogenic separation further purifies the hydrogen[6].

Collot[1] summarized the findings of several DOE-sponsored system studies on the economics of hydrogen production via conventional (e.g., as described above) and new coal gasification technologies. The report indicates that current state-of-the art technology does not provide cost-competitive hydrogen with respect to the cost of hydrogen produced via Steam Methane Reforming. However, new concept plants involving integrated reaction/separation units to conduct the WGSR (i.e., a membrane reactor with a hydrogen-selective membrane) appear to be promising. Depending on the operating conditions (e.g. WGSR temperature) hydrogen production via coal gasification may become economically attractive. Moreover, the use of the membrane reactor has the potential to reduce the cost of $H_2$ production and $CO_2$ capture while increasing the overall efficiency by 30%[1]. Although the economic comparison between coal gasification and Steam Methane Reforming heavily hinges on the fluctuating cost

of methane, it is clear that new technologies should be pursued in order to obtain a viable transition step towards the hydrogen economy.

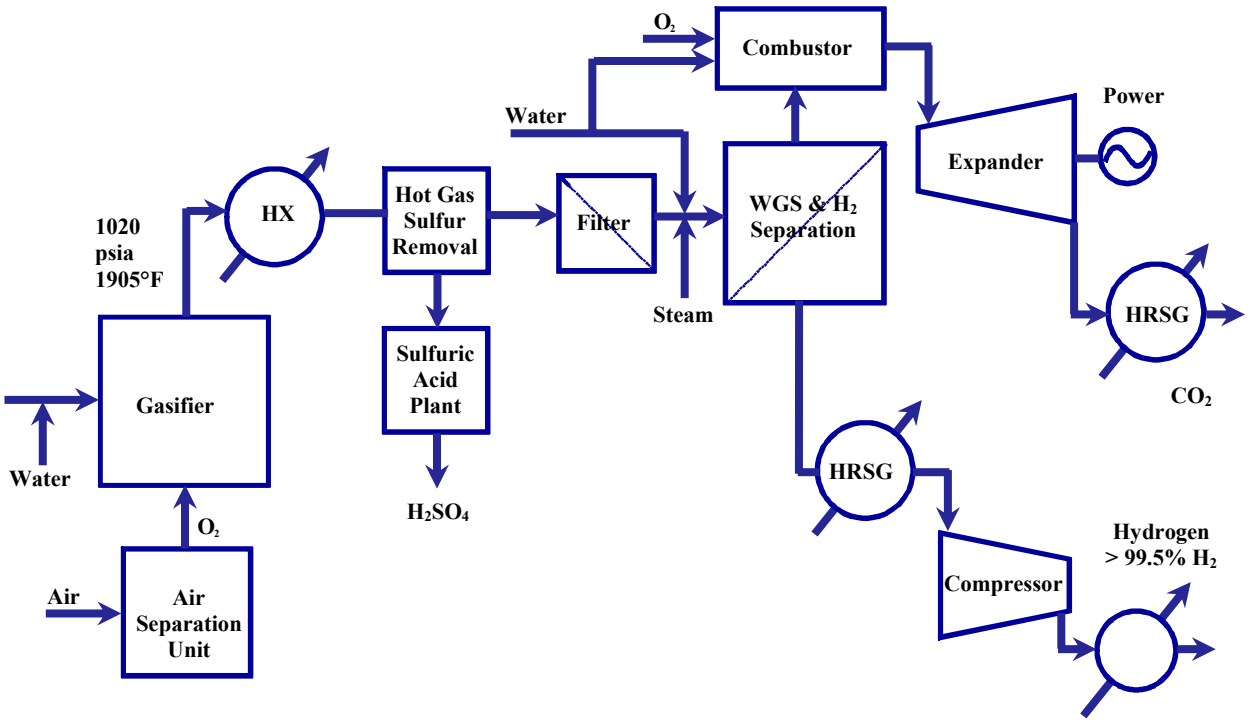


Figure 1. Schematic representation of an IGCC plant for the production of hydrogen and electricity from coal. Adapted from Reference 7.

Figure 1 depicts the schematic of an Integrated Gasification Combined Cycle, IGCC, an advanced gasification concept plant for the production of hydrogen and electricity from coal. This plant involves the use of an integrated reaction/separation unit. The effluent of the gasifier is cooled down and subjected to sulfur clean-up and then directed to the hydrogen-selective membrane reactor. The temperature of the stream is dictated by the operating temperature of the sulfur-cleaning step. Although considerable effort has been devoted to the development of high-temperature desulfurization, the technology remains elusive. The hydrogen produced via the WGSR is separated directly in the membrane reactor avoiding costly separations downstream. In

addition, the removal of hydrogen would overcome the thermodynamic limitation by means of the continuous shift of the reaction towards the products enabling the WGSR to be conducted at higher temperatures (in a sulfur-tolerant membrane reactor). A modeling study by Parsons[8] analyzed the effect of the temperature of operation of the WGSR membrane reactor. Even though the change in the cost of hydrogen is modest (5.11 $/MMBTU with the membrane reactor operating at 1034 K versus 5.06 $/MMBTU at 873 K) and the plant efficiency remains essentially unchanged (80.2% and 80.4%, respectively), the net power production is much larger when the membrane reactor is operated at high temperature (18 MW and 7 MW, respectively). Further, the flux of hydrogen through the membrane, which in general improves with increasing temperature and pressure, was shown to exert a significant effect on the economic results. As a consequence, it is expected that higher temperatures result in improved plant performance, i.e. less membrane area (an expensive capital cost) would be required. Furthermore, at high-temperature the enhanced gas-phase kinetics of the WGSR may preclude the need for a catalyst, rendering a more simple process. Therefore, a membrane reactor located at the exit of the gasifier would eventually translate into a more straightforward path to the production of hydrogen and electricity via an IGCC.

In spite of the foreseeable theoretical and economical advantages of a high-temperature, high-pressure membrane reactor for the WGSR, the technical feasibility of this process has not yet been addressed. Simulation studies conducted by Ma and Lund[9] suggest that the moderately high-temperature (~773 K) operation of a catalytic membrane reactor for the WGSR would be limited by the reaction kinetics rather than the membrane performance. No previous studies on the high-temperature, high-pressure gas-phase kinetics of the WGSR are available in the

literature, however. Furthermore, the possible effect of the membrane material on the kinetics has not been explored. The previous literature on membrane reactors for the WGSR has focused in the low-temperature regime where a catalyst is required to enhance conversions. Although conversions above the equilibrium limitation have been reported (see section 2.2), the relatively high equilibrium conversions obtained at short contact times in the low temperature regime do not allow a clear distinction between the membrane reactor and a hydrogen membrane located immediately downstream a conventional water-gas shift reactor[10]. Moreover, it is not possible to extrapolate the performance of the low-temperature, catalyst-assisted WGSR in a membrane reactor to a high-temperature, catalyst-free membrane reactor.

The apparent lack of research interest in the very high-temperature membrane reactor concept may be explained by considering several factors:

- *Membrane stability* If high-purity hydrogen is desired (for instance, for solid-oxide fuel cells), a dense membrane (i.e. a membrane with infinity selectivity towards hydrogen) is required. A number of metals (Ta, V, Zr, Nb) are known to display large diffusivities for hydrogen transport[11] and sufficiently high solubility, yielding the highest known hydrogen permeability values of any metal, including palladium. In addition, the mechanical strength of these materials makes them good candidates for high-pressure environments. However, the presence of small amounts of contaminants (e.g. oxygen) causes a notable deterioration of the hydrogen flux due to their high reactivity leading, for instance, to the formation of oxides on the surface of the metal. For this reason, palladium and palladium alloys, which exhibit infinite selectivity towards hydrogen as well as reasonably high diffusivities, are

preferred as materials for dense membranes. The high cost of palladium, though, restricts its use as a stand-alone, unsupported membrane. Ideally, a thin layer should be applied on top of a high-diffusivity, less-expensive metallic support material (e.g., Ta). The support metal can be porous (e.g., porous stainless-steel) or dense (e.g., Ta). However, intermetallic diffusion[12,13] and delamination of the thin layer[14] at high temperature hinder this approach. The use of diffusion barriers has been suggested for overcoming this problem[15] but has not been demonstrated at very high temperature.

- *Membrane compatibility* Ceramic materials display good thermal stability. Membranes characterized by large hydrogen fluxes can be made from porous ceramics and their limited selectivity can be improved by tailoring pore size. However, although these membranes are potential candidates for applications where very-high purity of hydrogen is not required, sealing ceramics to metals is a challenging issue that may deter their commercial application. In addition, high-pressure operation can adversely affect the separation factor of porous membranes. On the other hand, the use of porous ceramics as supports for thin dense layers of palladium requires a careful match of the thermal expansion of the ceramic and metallic components. Further, the difficulties of sealing the ceramic support to metallic lines must still be addressed.
- *Membrane poisoning* Sulfur compounds, primarily $H_2S$, present in a gasifier effluent stream poison palladium membranes[16,17]. In spite of the great deal of research that has been devoted to the high-temperature clean-up of sulfur, it remains a problem that would preclude the use of a membrane reactor directly at the outlet of the gasifier. Recently, Morreale and coworkers[18] at the National Energy Technology Laboratory, NETL, demonstrated that some palladium-copper alloys withstand up to 1000 ppm of $H_2S$ over a wide range of temperature

without significant loss of the hydrogen flux. A more complete explanation of palladium-copper alloys than that of McKinley[19] was provided by Morreale, who demonstrated that only the fcc phase was sulfur-resistant[20]. Currently Morreale's group is determining the minimum concentration of copper that would render a sulfur-tolerant palladium-copper membrane. These efforts are being complemented by computational chemistry simulations of the hydrogen diffusion through palladium and palladium-copper alloys at high temperatures[21,22].

The potential benefits of the high-temperature, high-pressure WGSR in the production of hydrogen from coal gasification along with the progress made to address the issues faced in the operation of membranes in harsh environments, support a more detailed study of the technical feasibility of the process. It is the objective of this work to evaluate the production of hydrogen at conditions similar to a gasifier stream, i.e. high-pressure (1.6 MPa) and very high-temperature (1173 K), with a membrane reactor that is devoid of heterogeneous catalyst particles, considering that the conjunction of an enhanced reaction rate and hydrogen permeation rate at those conditions would overcome the thermodynamic limitations, i.e. higher-than-equilibrium-conversion-in-a-conventional-reactor conversions can be achieved. Specifically, the interplay between reaction kinetics, possible catalytic effects of the reactor itself (shell and membrane surfaces) and hydrogen permeation will be addressed. A highly selective palladium membrane will be used for the membrane reactor. Future research at NETL will address the performance of a sulfur-tolerant (e.g. Pd-Cu) membrane reactor.

The work is distributed as follows. After a short background on membranes, Chapter 2.0 discusses the results of previous experimental and simulation studies on membrane reactors for the WGSR. An overview of the kinetic studies of the high-temperature WGSR is then included. Chapter 3.0 gives the detailed description of the experimental setup used in the experiments. Simulation results were used in analyzing and interpreting the experimental results. Specifically, the gas-phase mechanism of the reaction and the flow pattern and conversions in the reactor were simulated. Details are also given in Chapter 3.0. A thorough study of the high-temperature, high-pressure WGSR was conducted. This information is essential to assess whether a catalyst-free membrane reactor is viable. Experimental results on the gas-phase kinetics of the reaction are presented and discussed in Chapter 4.0. The WGSR is a reversible reaction. For this reason both the reverse (section 4.1) and the forward (section 4.2) reactions were studied. It is important to stress that these results provide important new data that can be used in the modeling of the high-temperature, high-pressure chemistry commonly encountered in industrial settings. Therefore, a correlation for the reaction rate is included. The reaction was also conducted in the presence of Inconel®600 to explore the effect of a common high-temperature construction material on the reaction kinetics. The effect of potential membrane materials (Pd and Pd-Cu alloys) on the kinetics was studied as well. Chapter 5.0 explores the behavior of the WGSR in a Pd-based membrane reactor. The effect of CO and $H_2O$ on the permeation of $H_2$ was then determined. Preliminary exploration of the effect of reaction conditions was performed. Two cases were addressed, a membrane reactor combining fast-kinetics with low hydrogen flux (e.g., small surface area, thick membrane) and vice versa. Conclusions are drawn as to the advantages and disadvantages of each approach. Finally, Chapter 6.0 summarizes the findings and provides the outlook for future work.

# 2.0 BACKGROUND

## 2.1 HYDROGEN-SELECTIVE MEMBRANES

A membrane can be defined as a thin barrier that allows preferential passage of a certain component(s) present in a mixture. Membrane separations are used in applications ranging from micro-filtration to gas permeation and can separate materials as diverse as bacteria, proteins, colloids, and gases and vapors[23]. The driving force for the permeation of the component(s) is the difference in concentration (i.e., partial pressure in gas separations) across the membrane. Membranes can be classified as polymeric, ceramic, and metallic. Ceramic membranes can be further divided in porous and non-porous (or dense). This section will briefly review some fundamental aspects of membranes for gas separation at high temperature. Therefore, polymeric membranes, that are restricted to very-low temperatures (<473 K) will not be included.

High selectivity and large permeation rate, the two key goals of membrane separations, are difficult to accomplish simultaneously. In general, high selectivity comes at expense of low permeation rate and vice versa. Both the selectivity and permeation rate are defined by the transport mechanism; porous membranes often display low selectivity and large fluxes, while the opposite is true with dense (non-porous) membranes. Porous membranes may be sub-divided by pore size into macroporous (pore diameter larger than 50 nm), mesoporous (2 – 50 nm), and microporous (<2 nm)[23]. Transport through microporous membranes is governed by *activated*

*diffusion*; basically, the different molecules diffusing through the pore have a different dynamic adsorption/desorption mechanism which results in a degree of separation. Clearly, molecules larger than the pore size will be rejected. Diffusion through mesoporous membranes is determined by *Knudsen diffusion*; if the pore diameter is smaller than the mean free path of the gas (i.e. the average distance traveled by one gas molecule between collisions), collisions with the walls will be frequent and molecules will be separated depending on their molecular weight. Consequently, hydrogen can be separated from other gases. Macroporous membranes present viscous flow which does not allow a large degree of separation. Hydrogen transport through dense metallic membranes, on the other hand, follows a completely different mechanism called the solution-diffusion mechanism. There are seven steps in this mechanism: a) Diffusion from the bulk phase, b) adsorption and dissociation on the membrane surface, c) dissolution in the metal lattice, d) diffusion through the bulk of the metal, e) transport from the metal lattice to the surface, f) re-association and desorption from the surface, and g) diffusion to the bulk phase on the permeate side of the membrane. In general, the solution-diffusion mechanism results in infinite selectivity towards hydrogen. The different transport mechanism in dense membranes translates into a different driving force. When external mass transfer limitations are negligible, flux through porous membranes is proportional to the difference in hydrogen partial pressures whereas flux through dense membranes is usually proportional to the difference of the square roots of the hydrogen partial pressures.

The affinity for hydrogen displayed by palladium has been known for a long time. In the mid 1800s it was shown that palladium absorbs large amounts of hydrogen and that hydrogen diffuses through the metal[13]. However, it was not until the first half of the 20$^{th}$ century that the

concept of palladium membranes was developed with commercial applications appearing by 1950[13]. Since then, palladium and its alloys have been extensively studied for the separation of hydrogen (see for instance refs. 24,25). Specifically, over the past two decades a growing interest in economically viable palladium membranes has driven the research towards thin, pin-hole free membranes. Great progress has been made in the production of thin (micron range), defect-free membranes on porous supports that would minimize the required amount of palladium while providing large hydrogen fluxes. Simultaneously, the area of palladium membrane reactors has received significant attention. Gryaznov and coworkers have demonstrated the advantage of this concept for a number of hydrogenation, dehydrogenation and coupled hydrogenation - dehydrogenation reactions[26]. The interest in palladium and palladium-alloy membranes stems from the infinite selectivity towards hydrogen. Although considerable research has been conducted in the field of porous membranes and high fluxes can be realized, extremely high selectivity has yet to be attained. Moreover, simulation studies of membrane reactors suggest that membrane reactors based on dense membranes may outperform membrane reactors based on porous membranes, especially at high pressures[27]. Therefore, this study will focus only on the use of palladium-based membrane reactors, although porous membranes remain a viable alternative technology.

### 2.1.1 Effect of contaminants on the permeation of hydrogen through palladium-based membranes

To assess the viability of palladium-based membranes for membrane reactors, it is essential to know the effect of other gases present in the gas mixture on the performance of the membrane. It has been reported that the presence of trace amounts of $H_2S$ can seriously impair the

permeation of hydrogen through palladium membranes[16,17]. A membrane must also retain permeance when exposed to other gasifier contaminants such as HCl, COS, $NH_3$, $O_2$, and Hg. Other gases (CO, $CO_2$, $H_2O$, $CH_4$) will also be present in the gasifier effluent stream at very high concentrations. Several studies have addressed the effect of such gases on Pd membranes.

Li and coworkers[28] studied the effect of CO and $H_2O$ on the permeation of hydrogen through thin Pd films supported on porous stainless steel; the tests were conducted at 653 K. They found that the addition of steam or CO in the range 2 - 15% has a considerable effect on the hydrogen flux. The adverse effect of steam, although reversible, appears to be more pronounced than that of CO. The WGSR is conducted in the presence of both CO and $H_2O$, however, and their results do not delineate the combined effect of high CO and steam concentrations. Amandusson and coworkers[29] showed that the reduction of hydrogen permeability due to the adsorption of CO at low temperature (<573 K) and sub-atmospheric pressure displays a strong temperature dependence, the effect being higher at low temperatures. On the other hand, Amano and coworkers[30] reported that large concentrations of CO or $CO_2$ (50% v/v) at near-atmospheric pressures have negligible effect on the permeation of hydrogen in the temperature range 473-723 K. These studies indicate that a small effect of CO, $CO_2$ and $H_2O$ on the permeation of hydrogen through Pd membranes at high-temperatures may occur, but it is relevant to ascertain whether such an effect occurs at the high-temperature and high-pressure conditions present in a post-gasifier stream.

## 2.2 THE WATER-GAS SHIFT REACTION IN A MEMBRANE REACTOR

The concept of membrane reactor and its applications has been extensively studied and several reviews[31,32,33,34] and books[23] have been published on the subject. The interest in membrane reactor technology derives from its potential enhancement of productivity and selectivity. The membrane in the reactor can fulfill one or several functions. It can be used, for instance, in the separation of one of the products (e.g., increasing the yield in equilibrium-limited reactions or offsetting separation units), in the controlled addition of one reactant (e.g., in partial oxidations), or in providing a contact medium for the reactants (e.g., three-phase reactors). The membrane could display activity for the reaction of interest, giving rise to the classification of membrane reactors as "catalytically active" or "inert".

Several reactions have been carried out in membrane reactors with hydrogen selective membranes, primarily dehydrogenations and steam methane reforming. The rate and selectivity of hydrogenation reactions have been reported to increase with the use of a palladium membrane reactor as well[34], where hydrogen diffuses through the membrane to the reactant side. This approach provides an alternate route to the use of solvents and catalysts, and to the dissolution of molecular hydrogen in liquid-phase reactions. Other examples of palladium catalytic membrane reactor-assisted reactions are hydrogen transfer reactions[34].

It has been shown that the WGSR is favored by the use of a palladium membrane that accounts for the separation of the hydrogen formed in the reaction. Pioneering work on Pd-based membrane reactors for the WGSR was done by Kikuchi and coworkers[35,36]. The reaction was carried out at 673 K over a commercial iron-chromium catalyst. The membrane was a very thin

palladium layer (~10 μm) deposited on a microporous glass tube. Conversions in the 80-92% range were reported, whereas the equilibrium limit was just 78%. A slight increase in the reaction pressure (0.1 to 0.5 MPa) improved the conversion from 92 to 99% as a result of the higher driving force for hydrogen permeation. Moreover, the industrial practice of using an excess of steam --beyond the amount required to prevent coking of the catalyst-- to drive the otherwise non-favorable equilibrium towards the products could be avoided with the membrane reactor. Basile and coworkers[37,38,39,40] have actively pursued a similar membrane reactor concept. When comparing the performance of several methods to deposit thin films on porous ceramic supports they found that a high selectivity towards hydrogen was essential to accomplish a shift in the equilibrium, otherwise the simultaneous diffusion of CO to the sweep side reduces the reactor conversion. Conversions higher than the equilibrium limit were attained only for defect-free Pd or Pd/Ag membranes (i.e. membranes allowing only hydrogen to flow through). CO conversion was maximized at 595 K, demonstrating the trade-off between the reaction rate (increasing with temperature) and the equilibrium conversion (decreasing with temperature).

Damle and coworkers[41] modeled the WGSR in a porous membrane reactor. Diffusion through the membrane followed the Knudsen mechanism. Their results showed that in order to achieve a significant shift in the equilibrium, the pressure ratio across the membrane should be large (>5). Moreover, they pointed out that as a consequence of the separation factor being inversely proportional to the total pressure (e.g., at high pressure the mean free path is smaller while the pore diameter does not change) the enhancement of conversion would be adversely affected at high pressure ratios across the membrane. However, the penalty for hydrogen

dilution due to back diffusion into the reaction side could become significant at lower trans-membrane pressure differences.

In summary, previous work showed the importance of achieving large hydrogen selectivity in order to enhance the hydrogen yield for the WGSR in a membrane reactor. In addition, experimental and modeling results suggested that a high pressure drop across the membrane would positively impact the performance of the reactor. However, the previous experimental studies on membrane reactors for the WGSR were conducted at relatively low pressures. It is therefore relevant to study the performance of the reactor at higher pressures because of the increased flux of hydrogen through the membrane brought about by the higher driving force. This improved performance might offset the slow reaction rate with the non-catalytic system proposed in this research (slow kinetics will render a small partial pressure of hydrogen inside the reactor and a smaller driving force). This possibility was not accounted for in the previous literature on the WGSR in membrane reactors, where attainment of high hydrogen concentrations (concentrations of products are higher due to the more favorable equilibrium conversions at low temperature) was assumed inside the reactor due to the presence of highly active catalysts.

## 2.3 KINETIC STUDIES OF THE HIGH-TEMPERATURE, GAS-PHASE WATER-GAS SHIFT REACTION

There is a large body of literature on the kinetics of the catalyzed forward water-gas shift reaction, fWGSR, at low temperatures (up to 873 K)[42]. Studies of the kinetics of the forward or reverse water-gas shift reaction at higher temperatures (>873 K) are scarce, however. The low

equilibrium conversions of CO that can be achieved in conventional reactors operating at high temperatures may explain this lack of data. However, due to the role played by the WGSR as a side-reaction in high-temperature environments, several investigations were conducted in the kinetics of the high-temperature, low-pressure reaction in the 1930s through the 1960s. More recently, the increased interest in the oxidation of organic compounds in supercritical environments has prompted interest in the kinetics of the WGSR in supercritical water[43,44,45,46,47]. These supercritical studies, however, will not be covered in the background provided here.

### 2.3.1 The Reverse Water-Gas Shift Reaction

Several investigations of the high temperature (>1148 K), low pressure (< 0.101 MPa), homogeneous, uncatalyzed reverse water-gas shift reaction, rWGSR, have been conducted. Bradford[48] proposed that the reaction would follow the simple gas-phase chain-reaction mechanism given below (M indicates any gas-phase collision partner). The chain is initiated by the gas-phase dissociation of hydrogen, (2-1). Propagation steps are represented by reactions (2-2) and (2-3). The termination step corresponds to the gas-phase re-association of $H_2$, (2-4), consuming the chain carriers.

$$H_2 + M \xrightarrow{k_1} 2H + M \qquad (2\text{-}1)$$

$$H + CO_2 \underset{k_{-2}}{\overset{k_2}{\rightleftharpoons}} CO + OH \qquad (2\text{-}2)$$

$$OH + H_2 \underset{k_{-3}}{\overset{k_3}{\rightleftharpoons}} H_2O + H \qquad (2\text{-}3)$$

$$2H + M \xrightarrow{k_{-1}} H_2 + M \qquad (2\text{-}4)$$

It can be shown that the condition of low conversion (i.e. negligible effect of the opposing reaction) and the assumption of a stationary state for the concentrations of the intermediates (H and OH concentrations do not change significantly with respect to time) lead to the following rate expression, equation (2-5),

$$r_r = \frac{d[CO]}{dt} = (\frac{k_1}{k_{-1}})^{1/2} k_2 [H_2]^{1/2} [CO_2] \qquad (2\text{-}5)$$

Therefore, the rate constant for the rWGSR may be expressed as shown in equation (2-6).

$$k_r = (\frac{k_1}{k_{-1}})^{1/2} k_2 \qquad (2\text{-}6)$$

Consequently, the expression for the rate of reaction in terms of $k_r$ becomes,

$$r_r = \frac{d[CO]}{dt} = k_r [H_2]^{1/2} [CO_2] \qquad (2\text{-}7)$$

The temperature-dependence of the rate constant, $k_r$, may be described by the Arrhenius equation

$$k_r = k_{0,r} e^{-Ea,r/RT} \qquad (2\text{-}8)$$

Graven and Long[49] studied the rWGSR in the temperature range 1148-1323 K. Their results support a gas-phase mechanism (the quartz vessel did not exhibit any influence on the

kinetics as demonstrated by the invariance of the rate when the reactor was packed with quartz), consistent with the Bradford mechanism. Tingey[50] studied the rWGSR over an extended temperature range (673-1473 K) and pointed out that at high-temperature (>1073 K), the reaction would follow the Bradford mechanism but would follow a different mechanism at lower temperature. Kochubei and Moin[51] concentrated on the high-temperature regime (1023-1523 K), corroborating Tingey's results and suggesting that the low temperature mechanism would involve some kind of surface interaction. Results from both investigations were in very good agreement, with both obtaining lower values for the rate of reaction than Graven and Long[49]. Tingey suggested that the higher reaction rate reported by Graven and Long[49] may have been caused by traces of oxygen in their feed stream that acted as a homogeneous catalyst, but was unable to substantiate that claim. An Arrhenius representation of the rate constant values predicted from each correlation in the 1123 – 1223 K temperature range is given in Figure 2; Table 1 provides the corresponding pre-exponential constant and activation energy. The prediction of the Karim and Mohindra[52] model of the water-gas shift reaction as twelve, simple, reversible, intermediate reaction steps involving nine species at temperatures up to 2500 K which used kinetic data available at the time is also presented. Given the disagreement among these reported values, the first objective of the kinetic study was to investigate the rWGSR kinetics under low-pressure conditions in quartz reactors. In addition, all of these studies were performed in highly diluted reaction gas mixtures at ambient pressure, without exploring the influence of pressure on the reaction rate and kinetics.

Table 1. Kinetic expressions for the reverse WGSR – literature correlations. $r_r = (k_{0,r} e^{-Ea,r/RT})[H_2]^{\alpha}[CO_2]^{\beta}$

| Reference | T (K) | P MPa | α | β | $E_{a,r}$ kJ/mol | $k_{0,r}$ $(L/mol)^{\alpha+\beta-1}$ $s^{-1}$ |
|---|---|---|---|---|---|---|
| Graven and Long[49] | 1148-1323 | 0.1 | 0.5 | 1.0 | 234.3 | $2.9 \times 10^{9}$ |
| Kochubei and Moin[51] | 1023-1523 | 0.1 | 0.5 | 1.0 | 326.4 | $6.4 \times 10^{12}$ |
| Tingey[50] | 1073-1323 | 0.1 | 0.5 | 1.0 | 318.0 | $1.2 \times 10^{13}$ |
| Tingey[50] | 673-1073 | 0.1 | 0.333 | 1.0 | 164.2 | $7.6 \times 10^{4}$ |
| Karim and Mohindra[52] | <2500 | 0.1 | 0.5 | 1.0 | 397.5 | $2.3 \times 10^{16}$ |

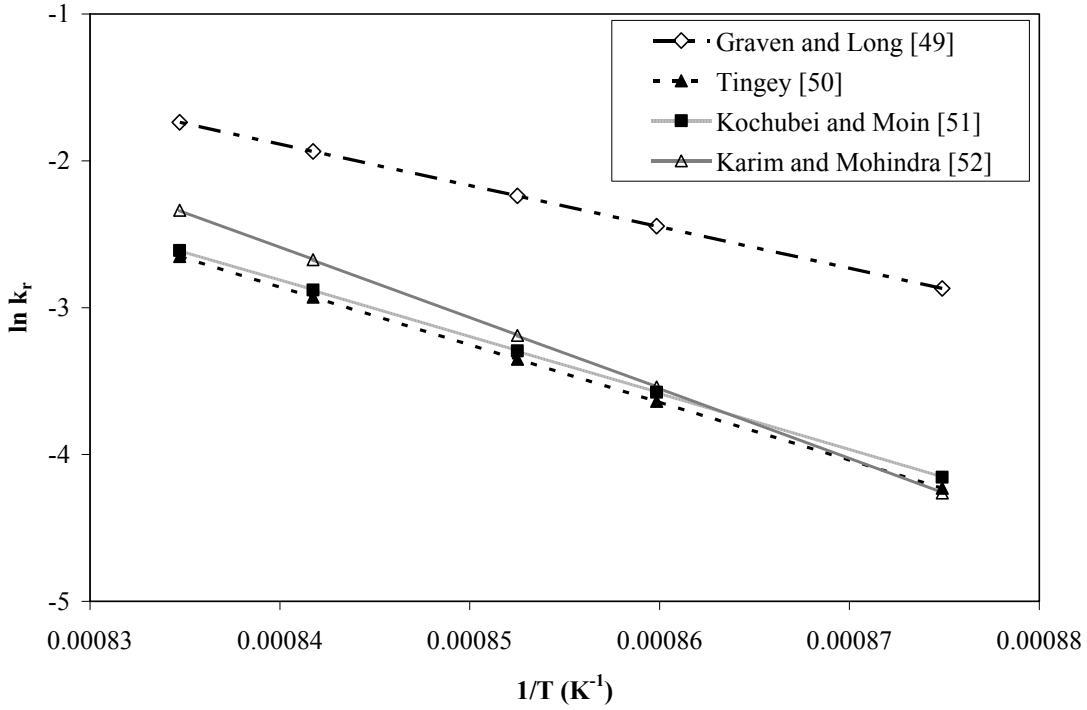


Figure 2. Arrhenius representations of rate constant expressions for the reverse WGS reaction obtained using a quartz reactor, r = $k[CO_2][H_2]^{0.5}$, $k$ $[L^{0.5}mol^{-0.5}s^{-1}]$; results of previously published literature.

### 2.3.2 The Forward Water-Gas Shift Reaction

Investigations on the kinetics of the fWGSR are less common than those on the kinetics of the reverse WGSR, perhaps due to the experimental difficulty posed by handling water vapor as a reactant. Only one complete kinetic study of the high-temperature fWGSR is available in the literature[49]. Some partial investigations were performed early, however, to explore the effect of the fWGSR in the oxidation of CO in the presence of water vapor[48,53,54].

The gas-phase, chain-reaction mechanism proposed by Bradford[48] can be used to describe the forward WGSR[49]. Reaction (2-9) provides the chain initiation by the reaction of $H_2O$ with any gas-phase molecule (designated by M). Reactions (2-10) and (2-11) are the propagation steps, while reaction (2-12) is the termination step.

$$H_2O + M \xrightarrow{k_9} H + OH + M \qquad (2\text{-}9)$$

$$CO + OH \underset{k_{-10}}{\overset{k_{10}}{\rightleftharpoons}} H + CO_2 \qquad (2\text{-}10)$$

$$H_2O + H \underset{k_{-11}}{\overset{k_{11}}{\rightleftharpoons}} OH + H_2 \qquad (2\text{-}11)$$

$$H + OH + M \xrightarrow{k_{-9}} H_2O + M \qquad (2\text{-}12)$$

The stationary-state approximation for the concentration of the chain-carriers (H and OH) leads to the following expression for the rate of reaction, Equation (2-13), under the conditions of low conversions:

$$r_f = \frac{d[CO_2]}{dt} = (\frac{k_9}{k_{-9}} k_{10} k_{11})^{1/2} [CO]^{1/2} [H_2O] \quad (2\text{-}13)$$

The rate constant for the fWGSR is then (Equation (2-14)),

$$k_f = (\frac{k_9}{k_{-9}} k_{10} k_{11})^{1/2} \quad (2\text{-}14)$$

And the rate can be expressed as,

$$r_f = k_f [CO]^{1/2} [H_2O] \quad (2\text{-}15)$$

Graven and Long's[49] investigation of the high-temperature, low-pressure *forward* WGSR yielded a reaction rate expression consistent with equation (2-15). Experimental results for the energy of activation and pre-exponential factor were 65.5 kcal/mol [274.1 kJ/mol] and 7.97E12 $(cm^3/mol)^{0.5}$ $s^{-1}$, respectively. Although Graven and Long's is the only experimental report on the energy of activation and pre-exponential factor published in the literature, their results can be compared with the reports of other investigators if some assumptions are made. Specifically, assuming equation (2-15) to be valid under the experimental conditions reported by Hadman and coworkers[53] (gas-phase reaction, low-pressure, 973-1073 K), the pre-exponential factor and energy of activation can be estimated from their reaction rate results, giving 2.22E14 $(cm^3/mol)^{0.5}s^{-1}$ and 76.3 kcal/mol [319.2 kJ/mol], respectively. These parameters predict rate constant values lower than those predicted by Graven and Long (Figure 3). Although Graven and Long's results on the reverse WGSR would appear to be biased towards the prediction of larger rate constants (Figure 2), it is not clear from the literature if this would also be the case for the forward WGSR. There remains, therefore, a discrepancy as to what are the appropriate

kinetic parameters (energy of activation, pre-exponential factor) for the forward WGSR. Consequently, this investigation attempted the kinetic study of the fWGSR both at low and high pressure conditions.

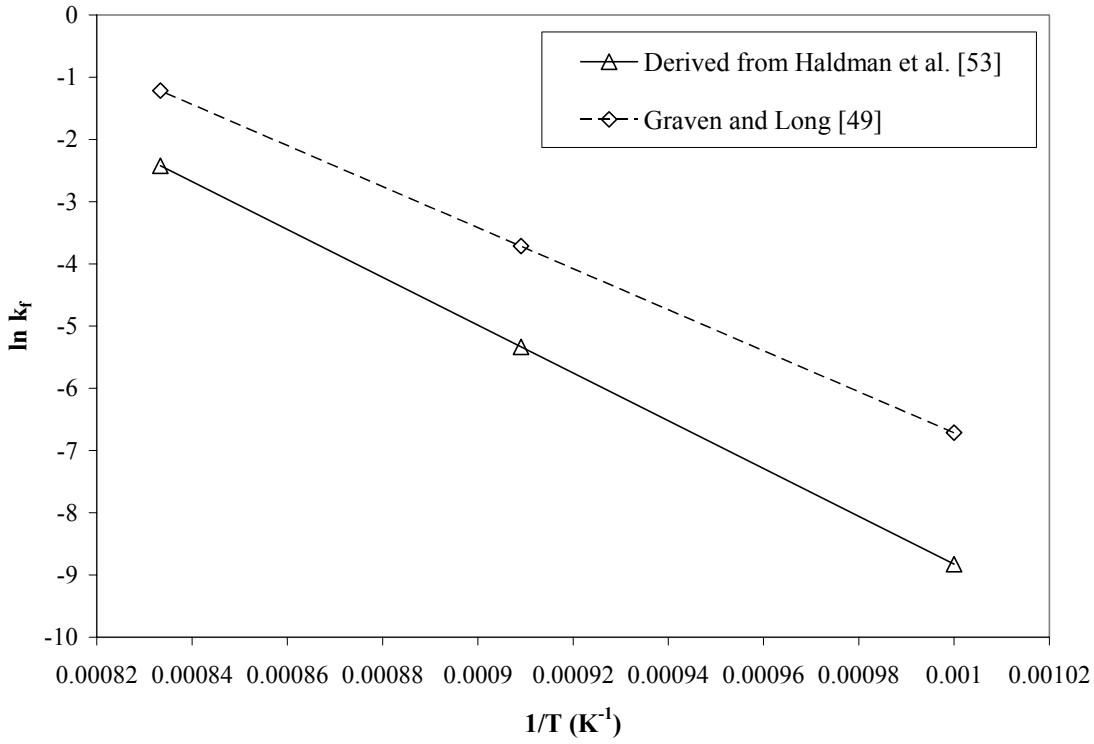


Figure 3. Arrhenius representations of the fWGSR rate constant – experimental results. Rate values were extracted from Hadman et al.[53] and Equation (2-15) was used to evaluate the pre-exponential factor and energy of activation.

# 3.0 EXPERIMENTAL AND SIMULATION DESIGN AND METHODS

## 3.1 EXPERIMENTAL SET-UP

### 3.1.1 Kinetic experiments

*HMT unit* All the experimental work was conducted in the Hydrogen Membrane Testing facility at the U.S. DOE National Energy Technology Laboratory. The Hydrogen Membrane Testing unit, HMT, designed to attain high-pressure (up to 3.0 MPa), and high-temperature (up to 1198 K) conditions was used. Due to safety concerns, operations were not conducted at pressures greater than 2.0 MPa. Figure 4 gives a schematic of the configuration for of the HMT unit for the kinetic experiments. The reactor (details given below) was placed in the center of a cylindrical heater located inside a purged containment vessel (to prevent explosions hazards if a leak develops). The reaction temperature was controlled with a ceramic resistance heater using a control loop with a coaxially mounted, dual element type-K thermocouple (TI), which was placed approximately 3 mm from the reactor. The reaction pressure was controlled with a stainless steel pressure control valve (PCV) employing a control loop with a pressure indicator (PI). An Iconic Genesis process control program provided the process control for the unit. It was not possible to use an additional thermocouple to determine the outlet temperature of the reactor due to the catalytic effect of the metal sheaths. The existence of a temperature profile, however, was verified with hydrogen, carbon dioxide, nitrogen, or helium flowing through the

system. Under typical low-pressure experimental conditions, the temperature within the reaction zone varied by ±8 K along its length from the average temperature that was used in the evaluation of the data.

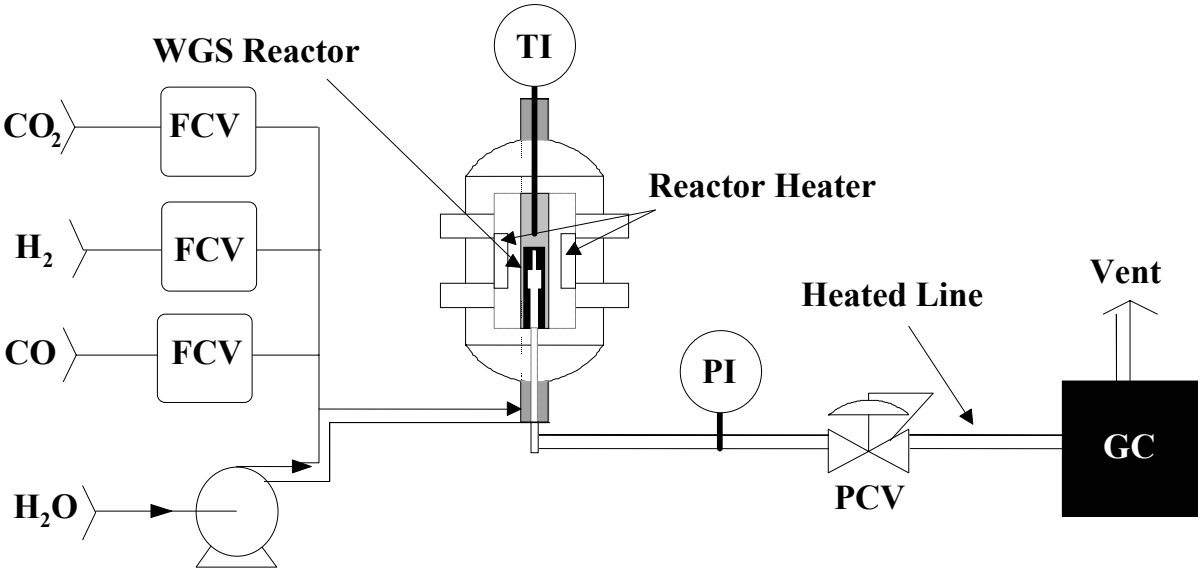


Figure 4. Overview of the experimental set-up used in the kinetic measurements.

*Reactor Feed* The flow rate of the feed gases, $H_2$, CO, or $CO_2$ (99.999%) was controlled with Brooks 5850i mass flow controllers (FCVs) and verified with a bubble flow meter. De-ionized liquid water, pumped by an ISCO 500D pump, was injected into a CO or He stream through 0.004" ID tubing. Tubing upstream and downstream the reactor was heated to about 423 K in order to prevent condensation of water. This temperature imposed a maximum to the partial pressure of steam in the high-pressure experiments. Typically, the highest molar concentration of water under these conditions was 30%. An oxygen trap was located in the feed gas line ($H_2$, CO, $CO_2$) before the reactor to eliminate the pronounced catalytic influence of $O_2$ on the reaction. Argon was continually bubbled through the water reservoir to prevent diffusion of air

into the water stream. The concentration of $O_2$ was below detectable limits for all the experiments. Only CO and $H_2O$ (*forward* WGSR) or $CO_2$ and $H_2$ (*reverse* WGSR) were fed to the system. The kinetic studies were conducted using either equal amount of the two reactants in the feed mixture introduced to the reactor over a range of flow rates or feed mixtures in which the concentration of one reactant was held constant while the concentration of the other was varied. In the latter case, the different partial pressures were accomplished by adjusting feed gas composition and total pressure, i.e. no diluent gas was admitted to the system.

*Reaction Zone* A quartz reactor or Inconel®600 reactor was located in the HMT-1 unit. The geometry of these reactors is illustrated in Figure 5 (a) and (b), respectively, and the dimensions of the reaction zone are provided in Table 2. When the quartz reactor was operated at elevated pressure, part of the feed inlet line was directed to the annular space between the Inconel®600 and the quartz as a means of preventing stresses across the quartz reactor walls. The pre-heated feed gases entered the reaction zone and flowed upward toward the top of the narrow inner tube that led to the reaction zone exit. Residence times of 0.3 - 0.5 s were chosen for the reactions conducted in the quartz reactor at low pressure. Typically, this yielded conversions which were great enough to assure accurate calculation of conversion, e.g. 0.3 - 0.8 % in the reverse WGSR. Residence times of 2 - 10 s were realized at high-pressure conditions because of the increased gas density. Comparable residence times were selected when the Inconel®600 reactor was used.

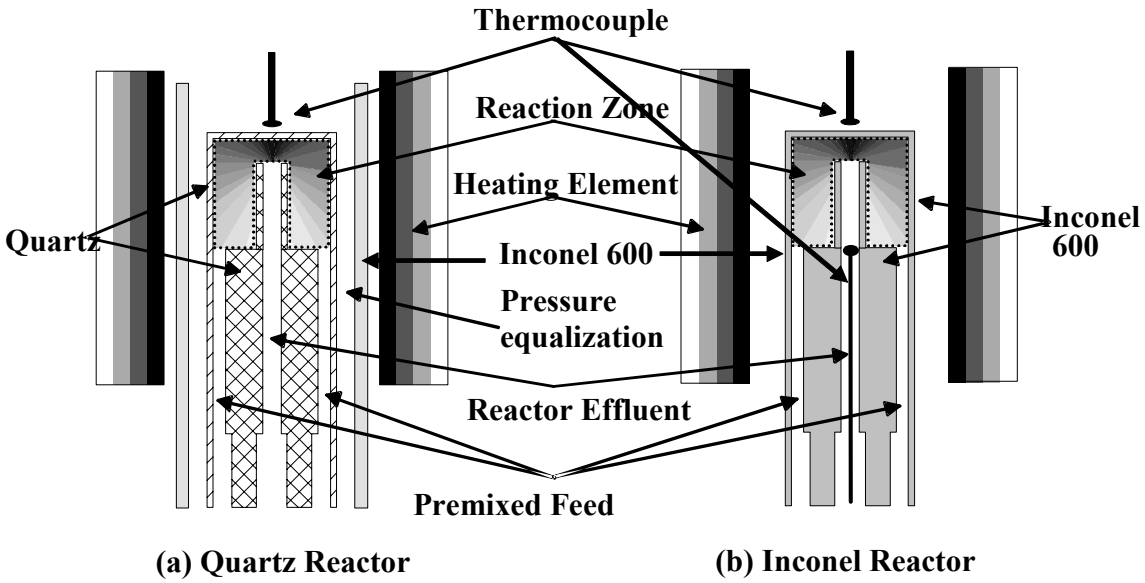


Figure 5. Detail of the reactor configuration employed in the kinetic experiments (packing not shown).

Table 2. Dimensions of the reaction zone of Quartz and Inconel®600 reactors.

| | Quartz | Inconel®600 |
|---|---|---|
| Reactor Height (cm) | 1.9 | 2.54 |
| Reactor ID (cm) | 1.1 | 1.35 |
| Inner Tube Height (cm) | 1.4 | 1.91 |
| Inner Tube ID (mm) | 1.85 | 2.87 |
| Inner Tube OD (mm) | 3.85 | 4.14 |
| Annular Gap, Reactor (mm) | 3.57 | 4.66 |
| Volume ($cm^3$) | 1.81 | 3.38 |

*Effluent Gas Stream* The effluent of the reactor was analyzed with a Gas Chromatograph, GC, equipped with a Thermal Conductivity Detector detector. Helium or argon were used as carrier gases. The GC column, HayeSep® D (porous polymer), allowed the separation and quantification of $H_2$, CO, $CO_2$ and $H_2O$ in the range of concentrations of interest. The only detectable products in the quartz experiments were CO and $H_2O$ (*reverse* WGSR), or $CO_2$ and $H_2$

(*forward* WGSR). Contrary to what was observed in the *reverse* WGSR where the $CO/H_2O$ ratio was close to unity for all experiments (the ratio expected from the stoichiometry of the WGSR), a $CO_2/H_2$ ratio greater than one was commonly observed during the *forward* WGSR experiments in the quartz reactor. The $CO_2/H_2$ ratio at the reactor outlet was typically in the range of 1.1 – 1.4, but ratios as high as 1.9 were also observed. Formation of carbonaceous particles after the reaction suggested that the higher CO conversion could be attributed to the CO disproportionation, or Boudouard, reaction, reaction (3-1).

$$2CO \leftrightarrow C + CO_2 \qquad (3\text{-}1)$$

The build-up of carbon particles, which was observed to have some catalytic effect on the reaction, was minimized by flowing a 2 mole % $O_2$/Ar stream after each experiment that was used to obtain conversion data for the *forward* WGSR. The introduction of oxygen removed any traces of carbon that had deposited within the reactor via the formation of $CO_2$. This topic is further discussed in Section 4.2. In the experiments carried out in the Inconel®600 reactor formation of methane, along with $CO_2$ and $H_2$, was observed and quantified.

Given the possibility that the Boudouard reaction could consume an appreciable amount of CO, thereby increasing the $CO_2/H_2$ ratio at the exit of the reactor to values greater than could be attained if the fWGSR alone were occurring, the use of CO conversion would over-predict the rate of reaction and rate constant. Therefore (unless specified otherwise) the reaction rates were evaluated from the $H_2O$ conversion ($X_{H2O}$), $H_2O$ concentration at the outlet ($C_{H2O}$) and residence time ($\tau$) according with Equation (3-2). (At low conversions, this CSTR design equation is valid

for CSTR or PFR.) Once the CO and $H_2O$ concentration exponents of the rate expression were elucidated, the rate constant was calculated from the rate expression and the rate value.

$$-r_{H2O} = [H_2O]\frac{X_{H2O}}{1-X_{H2O}}\frac{1}{\tau} \qquad (3\text{-}2)$$

Reaction rates for the *reverse* WGSR were evaluated from the $CO_2$ conversion, $CO_2$ concentration and residence time using the corresponding form of Equation (3-2). Rates calculated from $H_2$ were found to be identical. Once the $CO_2$ and $H_2$ concentration exponents of the rate expression were elucidated, the rate constant was calculated.

For experiments with larger conversions (in the range 2 – 10%), an integrated form of the PFR reactor design equation[55], Equation (3-3) (illustrated for the *reverse* WGSR, equation (2-7)), was used to determine the rate constant.

$$\tau = \int_{C_A}^{C_{Ao}} \frac{d[CO_2]}{-k[CO_2][H_2]^{1/2}} \qquad (3\text{-}3)$$

### 3.1.2 Hydrogen permeation experiments

Researchers at NETL have conducted a thorough investigation of the performance of palladium membranes at high temperature and pressure[56]. Hydrogen permeation studies in this project were restricted to the determination of the effect of CO and $H_2O$ in the permeance of hydrogen through palladium membranes. In addition, the possible influence of mass transfer limitations

under the experimental conditions tested was addressed. A thick (1 mm) pure-palladium (>99.9%, Alfa Aesar) disk was mounted in the permeation chamber shown in Figure 6. Gas mixtures of known concentrations of $H_2$ and He, $H_2$ and CO, or $H_2$ and $H_2O$ were fed to the membrane. Hydrogen that permeated through the membrane to the sweep side was removed by a stream of argon. The use of a sweep stream facilitated maintaining a low partial pressure of hydrogen in the permeate side (to maximize the driving force) and carrying the hydrogen to the GC for quantitative analysis. In addition, the analysis of the sweep stream allowed for the detection of leaks in the membrane. The retentate stream (e.g., feed side) was directed to, and quantified by, the gas chromatograph. The composition of the retentate and permeate (sweep) streams was determined simultaneously with a dual-column GC.

The palladium disk (1 mm thick) was placed on top of a porous support and welded to Inconel®600 tubes (see Figure 7). The porous support (porous Hastelloy, average pore size of 0.5 μm), was used as a means of giving mechanical strength to the membrane. A passivation layer (porous $\alpha$-$Al_2O_3$) was applied in the interface between the two materials prior to welding to prevent intermetallic diffusion. The transport resistance posed by the relative large pores in the porous support and passivation layer should be negligible compared to the diffusion of hydrogen through the thick palladium membrane.

The hydrogen flux through the membrane was quantified as follows. According to the solution-diffusion mechanism that governs the transport of hydrogen through dense metallic membranes, hydrogen diffuses as hydrogen atoms. Hence, the flux can be evaluated from the Fick's law (Equation (3-4)),

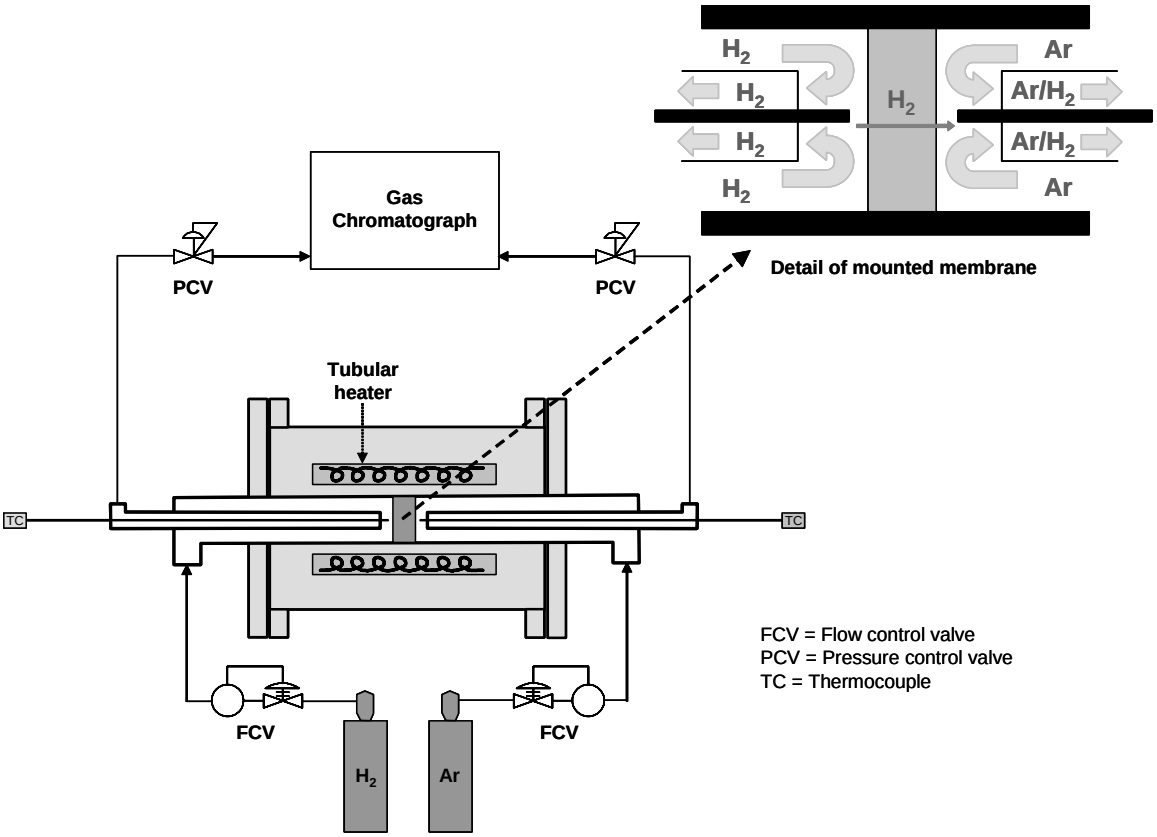


Figure 6. Experimental set-up for permeation experiments. Both the feed and sweep effluents are directed to the GC.

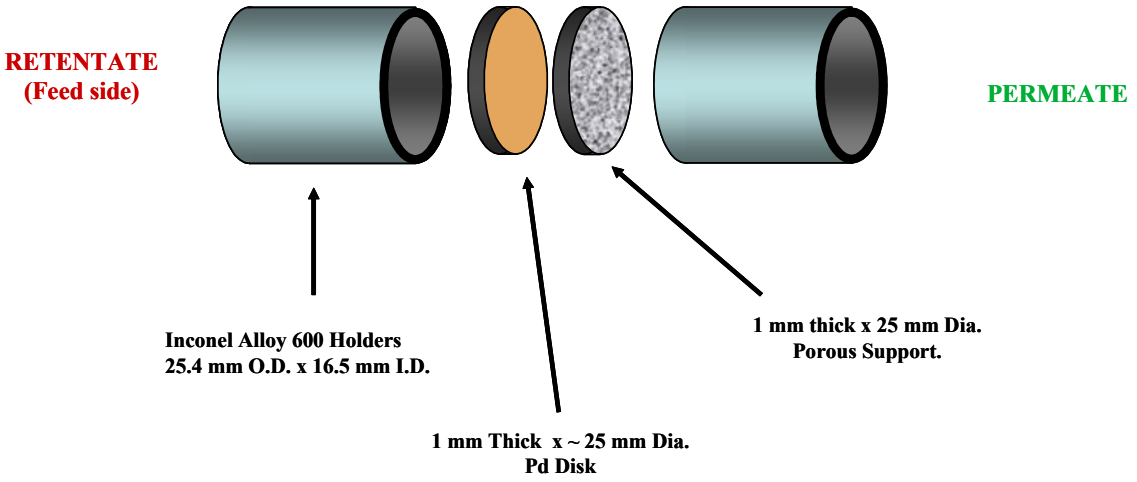


Figure 7. Assembly of the 1-mm Pd membrane for the permeation and membrane reactor experiments.

$$J_H = -D\frac{d[H]}{dx} \tag{3-4}$$

Where [H] represents the concentration of hydrogen *atoms* in the metal lattice. In thick palladium membranes (i.e., > 10 μm) the rate-determining-step is the permeation through the membrane itself[57]. Therefore, the hydrogen adsorption and dissociation at the surface can be considered to be at equilibrium giving rise to the Sievert's law[13] (Equation (3-5)),

$$[H] = K_s P_{H2}^{0.5} \tag{3-5}$$

The Sievert's constant, $K_s$, represents the solubility of atomic hydrogen in the metal lattice for dilute solutions with minimum hydrogen-hydrogen interactions. Substituting Equation (3-5) into Equation (3-4), with the assumption that the diffusion coefficient is independent of concentration, and integrating leads to Equation (3-6),

$$J_H = 2J_{H2} = -\frac{DK_S}{l}(P_{H2,feed}^{0.5} - P_{H2,sweep}^{0.5}) \tag{3-6}$$

where $l$ denotes the thickness of the membrane and $K_S$ is the hydrogen solubility in the metal. The hydrogen flux through the membrane (i.e., $J_{H2}$) can be related to the partial pressure difference across the membrane by the introduction of the permeance, defined as

$$K = \frac{DK_S}{2l} \tag{3-7}$$

The permeance provides an objective criterion to compare the performance of hydrogen membranes under different operating conditions (e.g., driving force). The flux is then given by Equation (3-8),

$$J_{H2} = -K(P_{H2,feed}^{0.5} - P_{H2,sweep}^{0.5}) \tag{3-8}$$

## 3.2 SIMULATION METHODS

### 3.2.1 Simulation of the gas-phase mechanism

Concentration-time profiles of each one of the six species (H, OH, $H_2$, $CO_2$, CO, and $H_2O$) involved in the gas-phase reaction were determined by the numerical solution of the system of non-linear ordinary differential equations derived from the Bradford mechanism. This simulation describes the reaction as it would take place in an ideal isobaric and isothermal (i.e. constant density) batch reactor. Reactions (2-1) - (2-4) were used in describing the *reverse* WGSR while reactions (2-9) – (2-12) were used for the *forward* WGSR. Basically, an ODE was written for each species. For example, the rate of change in the concentration of OH radicals in the *reverse* WGSR mechanism is given by (Equation (3-9)),

$$\frac{dC_{OH}}{dt} = k_2 C_H C_{CO2} - k_{-2} C_{CO} C_{OH} - k_3 C_{OH} C_{H2} + k_{-3} C_{H2O} C_H \tag{3-9}$$

Where $C_i$ = Concentration of species $i$

It was essential to use a stiff integrator and minimize the step size (e.g., $<10^{-4}$). MatLab®R12 (ODE23s) was used for this task. Reproducibility of the results was validated with other numerical software (Maple®). Rate constants and third-body efficiencies were taken from the GRI database[58]; however, the third-body efficiency for reactions (2-9) and (2-12) was corrected to reflect the original source[59,60] because of what appears to be a typographical error in the GRI data. Where no third-body efficiency values were available, the efficiency was assumed to be 1.0. Table 3 summarizes the rate parameters used in the simulation and Figure 8 gives an example of the concentration profile.

Table 3. Rate parameters used in the simulation of the gas-phase mechanism.

| Reaction | Rate Constant ($cm^3/mol/s$), or ($cm^6/mol^2/s$) | Third-body efficiencies |
|---|---|---|
| $OH + H_2 \rightarrow H + H_2O$ | $2.16E+08 * T^{1.51} * \exp(-3430/R/T)$ | N.A. |
| $OH + CO \rightarrow H + CO_2$ | $4.76E+07 * T^{1.23} * \exp(-70/R/T)$ | N.A. |
| $H + H + H_2 \rightarrow H_2 + H_2$ | $9.00E+16 * T^{-0.6}$ | N.A. |
| $H + H + H_2O \rightarrow H_2 + H_2O$ | $6.00E+19 * T^{-1.25}$ | N.A. |
| $H + H + CO_2 \rightarrow H_2 + CO_2$ | $5.50E+20 * T^{-2}$ | N.A. |
| $H + H + CO \rightarrow H_2 + CO$ | $1.00E+18 * T^{-1}$ | N.A. |
| $H + OH + M \rightarrow H_2O + M$ | $2.20E+22 * T^{-2}$ | $H_2$: 0.73<br>CO, $CO_2$: 1<br>$H_2O$: 3.65 |

Other kinetic models based on a more comprehensive network of elementary steps and intermediates, such as the model for the oxidation of $H_2$ and CO in sub- and supercritical water proposed by Holgate and coworkers[46], could be used to describe the WGSR reaction. A simulation of such a network was performed and the results were nearly identical to the Bradford

mechanism. Therefore, the Bradford mechanism was considered to be an adequate representation of the WGSR under the conditions studied.

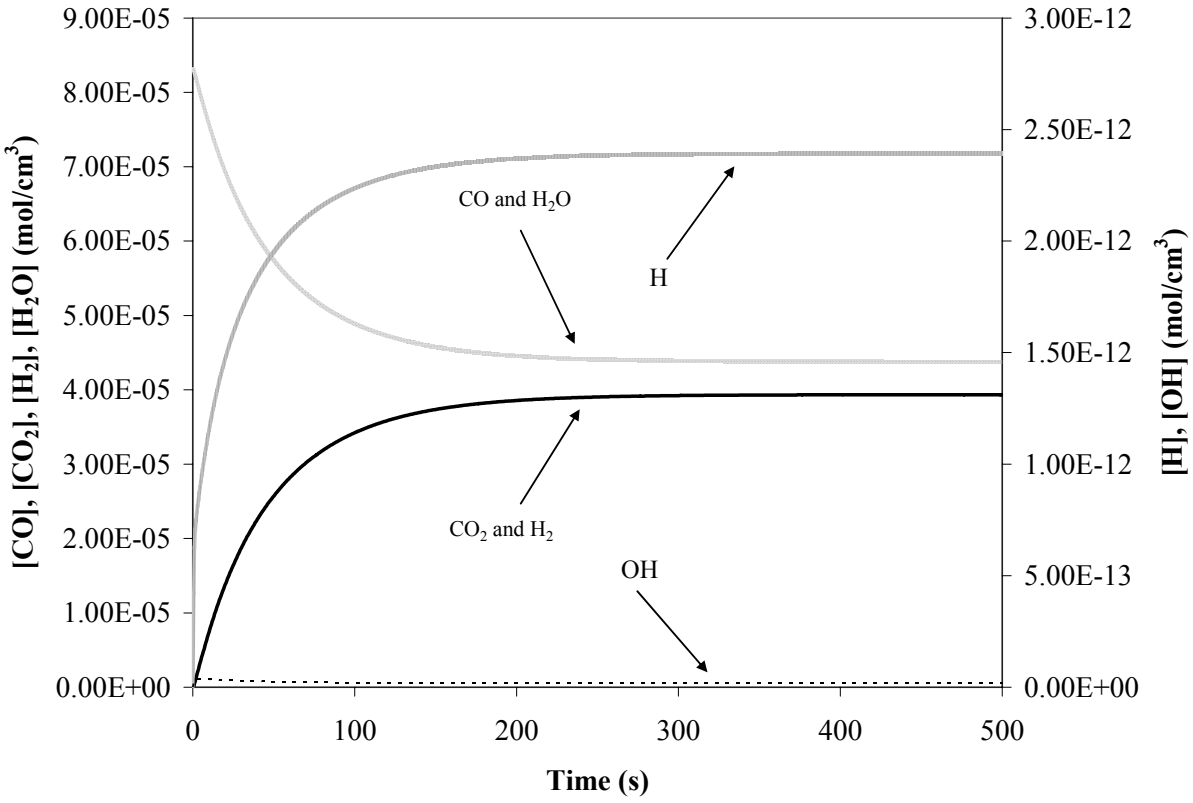


Figure 8. Concentration-time profile obtained from the numerical solution of the Bradford mechanism. *Forward* WGSR, T = 1173 K, P = 1.6 MPa, $y_{H2O,0} = y_{CO,0}$, $y_{CO2,0} = y_{H2,0} = 0$.

### 3.2.2 Simulation of the reaction conversions with the *forward* WGSR approaching equilibrium

The rate expression derived from the Bradford mechanism, Equation (2-15), is restricted to low conversions and lacks thermodynamic consistency. Even though it can accurately describe the

rate of reaction at low conversions, it is not adequate for the design of reactors attaining near-equilibrium conversions. A rate expression that accounts for the opposing reaction and the equilibrium limitation is required. Therefore, simulations were carried out to determine whether Equation (3-10), a simple modification of equation (2-15) that incorporates the effect of the reverse reaction, similar to the expressions utilized to describe the heterogeneous fWGSR[42], would be suitable to for the gas-phase reaction at large conversions. Specifically, the concentration-time profiles obtained in section 3.2.1 were compared with the prediction from Equation (3-10); the rate constant was calculated by replacing the values reported in the GRI database in Equation (2-14).

$$r = \frac{d[CO_2]}{dt} = k[CO]^{0.5}[H_2O](1-\beta) \qquad (3\text{-}10)$$

With β defined as

$$\beta = \frac{[CO_2][H_2]}{[CO][H_2O]}\frac{1}{K_{eq}} \qquad (3\text{-}11)$$

The equilibrium constant is obtained from the correlation reported by Singh and Saraf[61],

$$\ln(K_{eq}) = \frac{1}{1.987}\left(\frac{9998.22}{T} - 10.213 + 2.7456*10^{-3}T - 0.453*10^{-6}T^2 - 0.201\ln T\right) \qquad (3\text{-}12)$$

Figure 9 illustrates the conversions calculated from the numerical solution of the mechanism and those evaluated from Equation (3-10). The equilibrium conversion predicted by

Equation (3-10) agrees very well with the simulation of the mechanism. At low and high conversions both the rate expression and the simulation yield almost equal results. The difference in the results at the intermediate range of conversions is lower than 15%. In addition, the simulation of the reaction as a non-reversible reaction indicates that the effect of the opposing reaction, i.e. *reverse* WGSR for the conditions described in the figure, is small at conversions less than 20 – 25%.

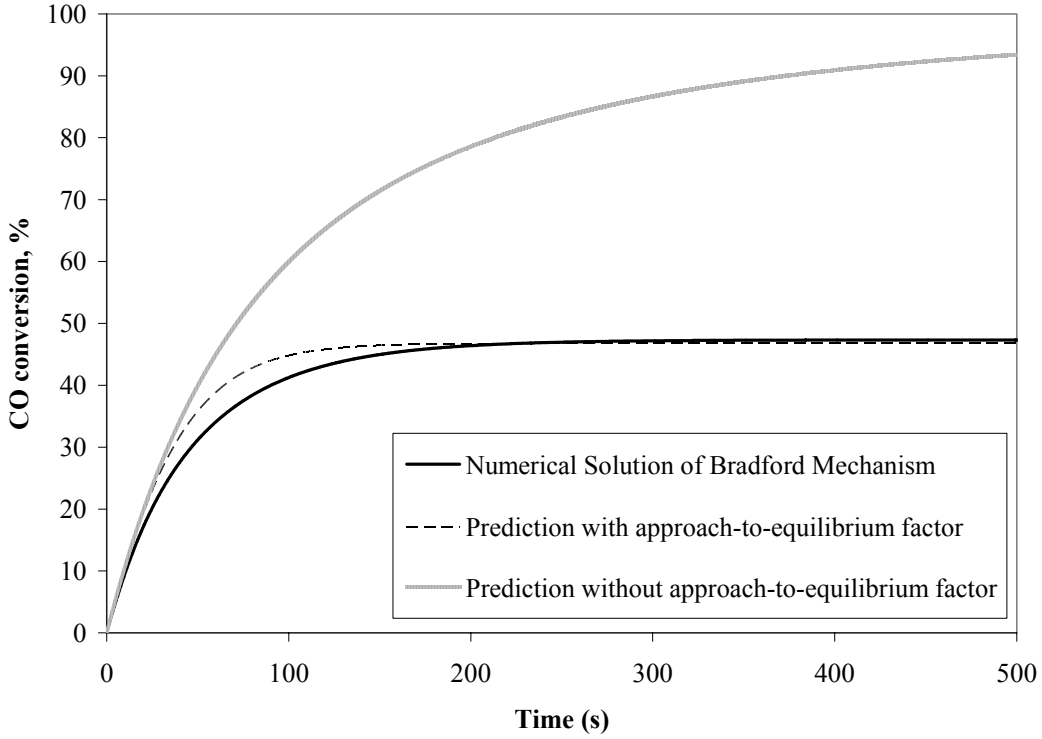


Figure 9. Prediction of CO conversion using the approach-to-equilibrium factor. Conversions evaluated from the rigorous solution of the mechanism are given for comparison. Conditions are similar to those in Figure 8.

### 3.2.3 Computational Fluid Dynamics (CFD) simulations

Fluent software was used to model the flow pattern in the reactor configuration employed in this investigation, as well as in the reactors described in previous literature reports. In particular, the

Residence Time Distribution (RTD) plots along with the expected conversions were evaluated to rule out the role of non-idealities in the discrepancies among kinetic results. The simulations were implemented and run by William Rogers (NETL) and Shaoping Shi (Fluent Inc.). Details are given in APPENDIX A.

### 3.2.4 Simple model of the gas-phase WGSR in tubular membrane and traditional reactors

*The WGSR in a Membrane Reactor* The gas-phase WGSR was modeled in a tubular membrane reactor with a thin, unsupported Pd membrane. The reaction was assumed to take place inside the tube while the hydrogen permeated through the membrane was removed by a sweep gas flowing in the shell side. Three different cases were considered, namely, a very large sweep flow rate (i.e., a zero partial pressure of hydrogen in the sweep side), counter-current, and co-current flow of the sweep gas. The basic assumptions of the model are as follows,

- Tube side performs like an isothermal PFR.
- Laminar regime (this assumption is consistent with the flow capabilities of the system).
- One-dimensional model.
- Steady State (i.e. flux through the mass transfer boundary layer is equal to the flux through the membrane).
- Mass transfer resistance, if any, is concentrated in the boundary layer in the tube side (sweep gas flow rate can be varied at ease).
- Infinite membrane selectivity (i.e. only hydrogen diffuses through the membrane); transport through the membrane is *diffusion-limited*.

- Gas-phase kinetics described by using Equation (3-10); catalytic effects of the membrane can be accounted for by increasing the rate constant in the gas-phase rate expression (for qualitative estimations).

The equations describing the system are presented in APPENDIX B. The model can be solved both in co-current and counter-current flow. Numerical solutions of the concentration – distance profiles were obtained with MatLab®R12.

*The WGSR in a traditional reactor* The WGSR is slightly exothermic. A temperature rise should be expected at large conversions if the heat of reaction is not efficiently removed. The increase in temperature would translate into a further increase in the reaction rate. Although the larger reaction rate would be desirable so to minimize the reactor volume in a conventional reactor, the decrease in equilibrium conversion would eventually result into lower conversions than if the reaction were carried out isothermally. On the contrary, the temperature rise would favor the operation of a membrane reactor provided the final temperature does not exceed the capabilities of the membrane itself. Therefore, a simple model to evaluate the temperature increase in a tubular, non-membrane reactor was written. The model was not intended to provide a detailed quantitative description of the experiments. Rather, the effect of the relevant parameters (i.e. overall heat transfer coefficient) on the performance of the traditional reactor would permit to gain some insight on the expected behavior of the membrane reactor. Details are given in APPENDIX B.

# 4.0 KINETICS OF THE HIGH-TEMPERATURE, HIGH-PRESSURE WGSR

## 4.1 KINETIC STUDY OF THE HIGH-TEMPERATURE REVERSE WGSR IN QUARTZ REACTORS

*Low-pressure rWGSR in a Quartz reactor* Equimolar feeds of $CO_2$ and $H_2$ were introduced at a total pressure of 0.1 MPa to the empty quartz reactor that is illustrated in Figure 5a. The power law exponents of the $H_2$ and $CO_2$ were assumed to be 0.5 and 1.0, respectively, in agreement with Equation (2-7). The Arrhenius representation of the reaction rate data for this low-pressure rWGSR over the 1148 – 1198 K temperature range is found in Figure 10. The calculated energy of activation and pre-exponential factor are given in Table 4. Corresponding values by Graven and Long[49] and Tingey[50] are given as comparison.

Table 4. Kinetic expressions for the rWGSR – experimental results. $r_r = (k_{0,r} e^{-Ea,r/RT})[H_2]^{\alpha}[CO_2]^{\beta}$

| Reference | T (K) | P MPa | $\alpha$ | $\beta$ | $E_{a,r}$ kJ/mol | $k_{0,r}$ $(L/mol)^{\alpha+\beta-1}$ $s^{-1}$ |
|---|---|---|---|---|---|---|
| Empty reactor, low-P | 1148-1198 | 0.1 | 0.5 | 1.0 | 222.2±3.9 | $1.21 \times 10^{9}$ |
| Empty reactor, high-P | 1148-1198 | 1.6 | 0.5 | 1.0 | 218.4±5.1 | $6.65 \times 10^{8}$ |
| Packed reactor, high-P | 1063-1138 | 1.6 | 0.5 | 1.0 | 355.6±1.5 | $3.0 \times 10^{14}$ |
| Graven and Long[49] | 1148-1323 | 0.1 | 0.5 | 1.0 | 234.3 | $2.9 \times 10^{9}$ |
| Tingey[50] | 1073-1323 | 0.1 | 0.5 | 1.0 | 318.0 | $1.2 \times 10^{13}$ |
| Kochubei and Moin[51] | 1023-1523 | 0.1 | 0.5 | 1.0 | 326.4 | $6.4 \times 10^{12}$ |

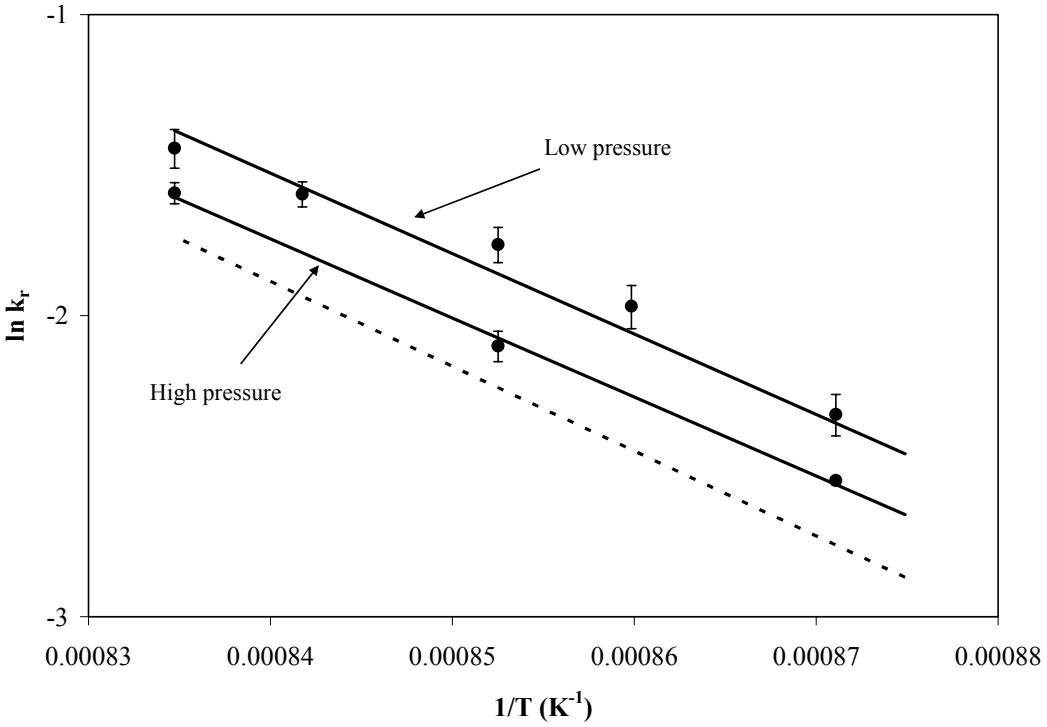


Figure 10. Arrhenius representations of rate constant expressions obtained in this study for the *reverse* WGSR at low and high-pressure in the empty quartz reactor, r = $k[CO_2][H_2]^{0.5}$, $k_r$ $[L^{0.5}mol^{-0.5}s^{-1}]$. Actual data points and errors are included. Graven and Long[49] low pressure correlation -dotted line- provided for reference.

The low-pressure rWGSR rate constant from this study was approximately 40% greater than that reported by Graven and Long[49] as illustrated in Figure 10. The activation energy of 53.1 ± 0.9 kcal/mol [222.2 ± 3.7 kJ/mol] was slightly less than the value of 56 kcal/mol [234.3 kJ/mol] reported by Graven and Long. The measured reaction rate constant values were roughly four times greater than those reported by Tingey[50] and Kochubei and Moin[51], however, as shown in Figure 2 and Figure 10 and Table 4. Thus, the low-pressure results for the empty reactor were in closer agreement with the results of Graven and Long[49] than the results of the other prior investigations.

*High-pressure rWGSR in a quartz reactor* The power law exponents of the $H_2$ and $CO_2$ were found to be 0.5 and 1.0, respectively (see Figure 11 and Figure 12). Equimolar feeds of $CO_2$ and $H_2$ were then introduced at a total pressure of 1.6 MPa to the empty quartz reactor. A stream of a pressure equalization gas, $CO_2$, was also maintained at 1.6 MPa in the space between the outer surface of the quartz reactor and the inner wall of the Inconel®600 pressure vessel. The activation energy of 52.2 ± 1.2 kcal/mol [218.4 ± 5.0 kJ/mol] was slightly smaller than the low-pressure result of 53.1 ± 0.9 kcal/mol [222.2 ± 3.7 kJ/mol] and the reaction rate constant slightly larger than that reported by Graven and Long, Figure 10 and Table 4. The high-pressure results for the empty reactor were also in good agreement with the Graven and Long[49] finding.

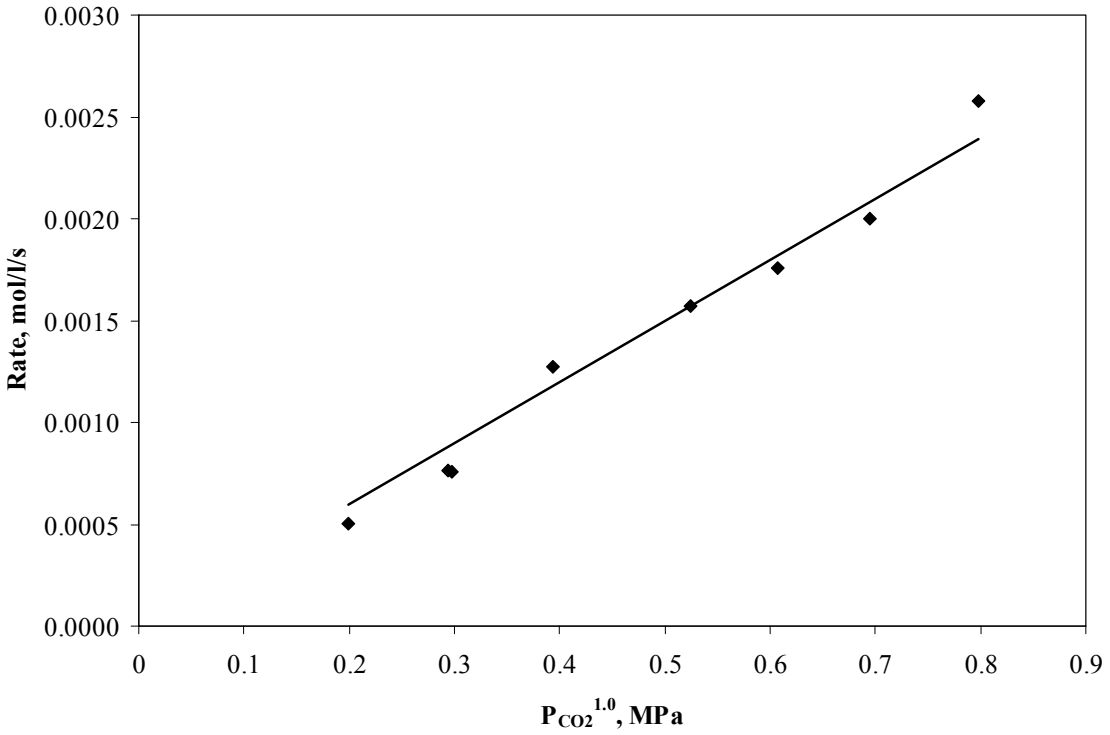


Figure 11. Dependence of the reaction rate of the *reverse* WGSR on the concentration of $CO_2$. Partial pressure of $H_2$ was maintained at 0.8 MPa. All experiments were performed at 1173 K. Residence time = 1.92 ± 0.15 s.

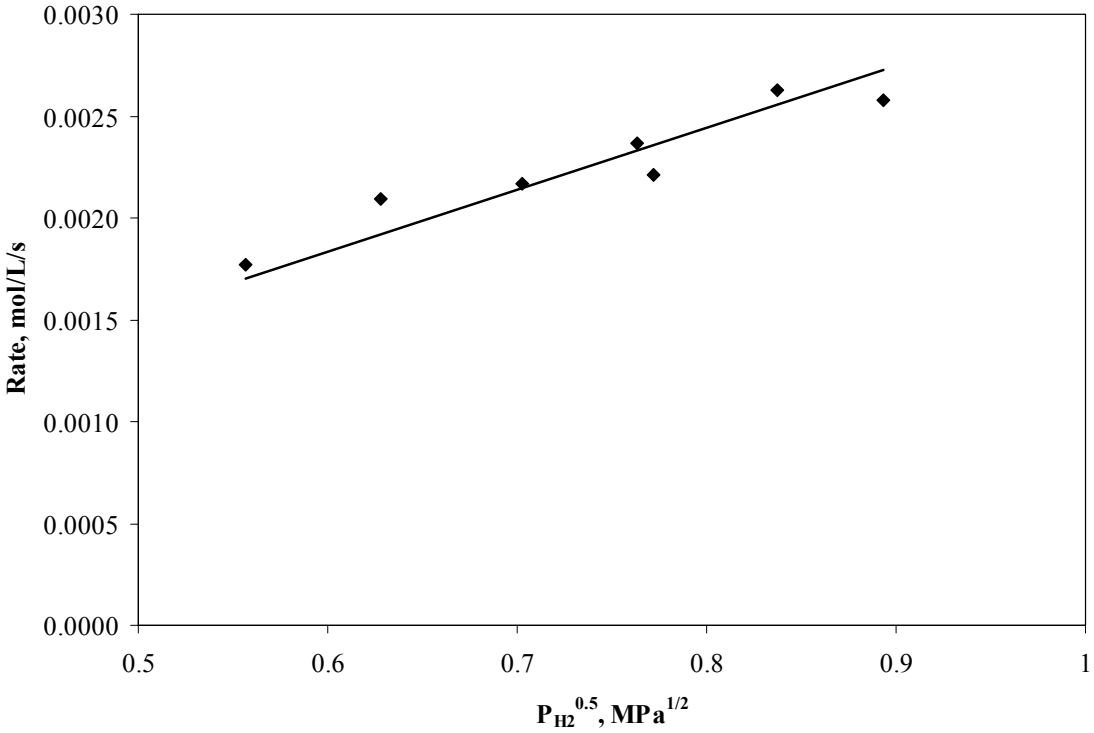


Figure 12. Dependence of the reaction rate of the *reverse* WGSR on the concentration of $H_2$. Partial pressure of $CO_2$ was maintained at 0.8 MPa. All experiments were performed at 1173 K. Residence time = 1.85 ± 0.08 s.

*Effect of reactor geometry on quartz reactor results* An attempt was made to determine the cause of the differences between the low-pressure rate constant correlations illustrated in Figure 2 and Figure 10. Tingey[50] suggested that the relatively high reaction rate constant values reported by Graven and Long[49] may have been caused by the presence of oxygen in the feed stream, but the rate constants derived from the empty quartz reactor were comparable to those of Graven and Long and no detectable amounts of $O_2$ were found in the $CO_2$ or $H_2$ feed streams or the pre-mixed feed stream. Each one of the previous investigations utilized an entirely different reactor configuration. In Graven and Long's reactor[49], $CO_2$ and $H_2$ were introduced to the reactor along with a diluent gas ($N_2$) to control partial pressures. Their cylindrical quartz reactor

(3.4 cm diameter, 6.4 cm length) was designed to minimize dead zones inside the reactor. This was accomplished with the use of tangential feed and withdrawal lines (1.5 mm ID). Tingey's reactor[50], on the other hand, consisted of a cylindrical quartz tube (3.3 cm ID, 27.1 cm length) that contained a co-axial quartz insert (2.2 cm ID, 21.0 cm length), resulting in a long annular flow section that was preceded and followed by short cylindrical sections (3.3 cm ID, 6.1 cm combined length). Coaxial capillary tubing served as feed and effluent channels for the reactor. The absence of the co-axial quartz insert resulted in very poor reproducibility of the results. Kochubei and Moin[51] designed empty quartz reactors (ID ranging from 0.6 – 6.5 cm) that employed a static mixer to mix the pre-heated $H_2$ and $CO_2$. The effluent gases were withdrawn from a capillary tube (1.5 mm ID) extending in the same axial direction as the cylinder, but located along the outside edge of the reactor.

CFD calculations were performed to determine if the reactor geometry could have influenced the kinetic results. Comparisons of the flow patterns of a non-reacting gas, the residence time distributions of a non-reacting mixture, and the conversion of the rWGSR under identical conditions were made for the NETL empty quartz reactor and the Graven and Long[49], Tingey[50], and Kochubei and Moin[51] reactors.

*Flow Patterns and Residence Time Distributions* In each representation of the flow patterns within the reactor, Figure 13– Figure 16, the length of the vector is proportional to the velocity of the particle at the origin of the vector. The direction of the vector indicates the direction in which the particle located at the origin of the vector is moving. In some cases, as noted in the figure legends, portions of the reactor in which the fluid is moving at extremely high velocity are

represented by a white field (rather than a group of extremely long vectors) for the sake of clarity.

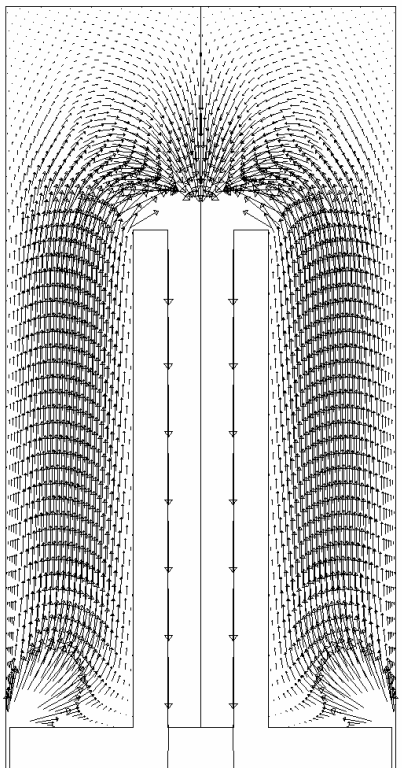

Figure 13. Flow field in the empty quartz reactor used in this study; axisymetric. Feed from narrow annulus along the perimeter of the bottom of the reactor; product withdrawal from the co-axial tube in the middle. White flow field in outlet section is high velocity flow field.

The empty quartz reactor was characterized by upward flow through the large annular gap within the reaction zone followed by a flow reversal at the top of the reactor. The gas then flowed vertically downward through the inner tube. There is a very small stagnant zone above the exiting port. This is manifested in the tailing of the Residence Time Distribution, RTD, plot, Figure 17, which exhibits a distribution broader than that expected for a laminar flow reactor with axial dispersion[55].

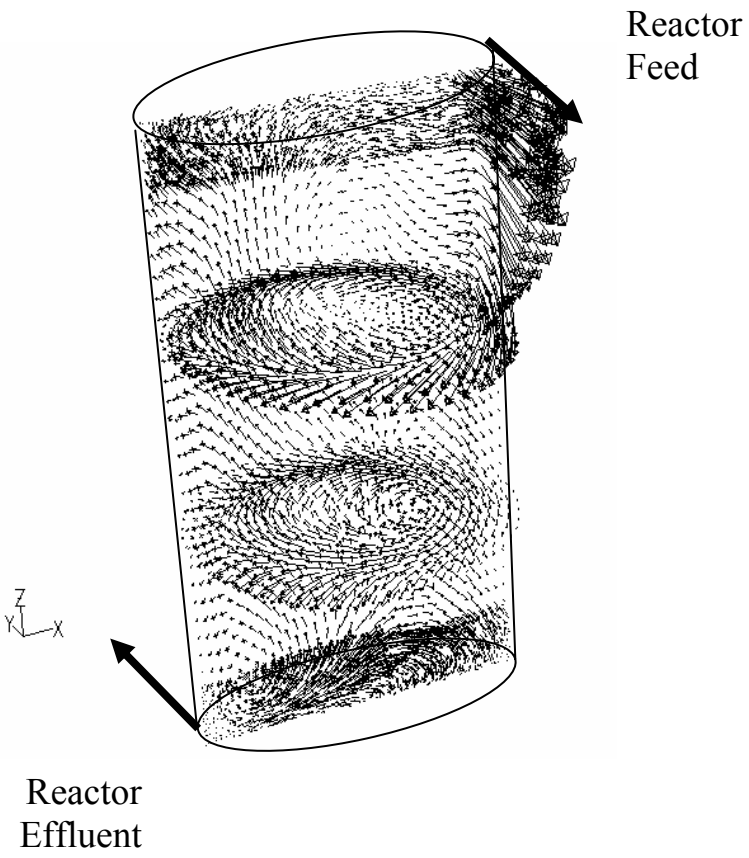


Figure 14. Reactor used by Graven and Long; non-axisymmetric cylindrical reactor; tangential feed entering at the top, right hand corner of the xz plane; tangential withdrawal of products through narrow tube at the bottom left hand corner of the xz plane; the 2 circular xy cross-sections are 1/3 and 2/3 of the way up the reactor in the z-direction.

The tangential feed and withdrawal of the Graven and Long reactor induced circular flow that formed vortices within the reactor as shown by the velocity vectors along the edge of the two xy-planes in Figure 14. The performance of this reactor is very similar to an ideal CSTR as the RTD shows (Figure 18).

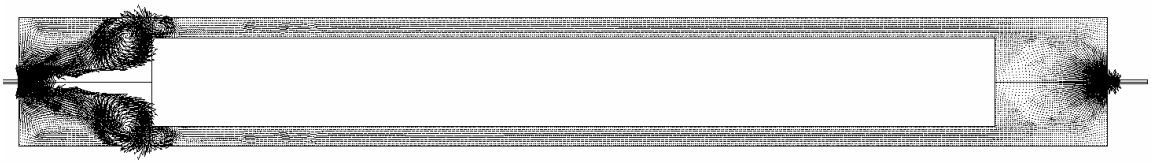

feed zone annular section product zone

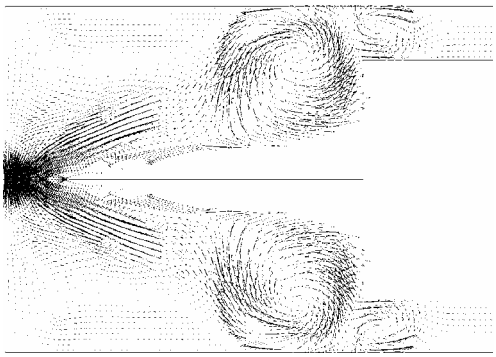

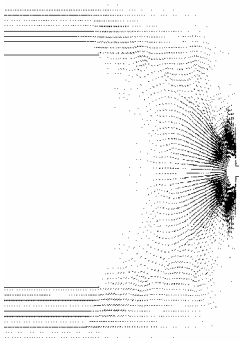

feed zone detail product zone detail

Figure 15. Tingey reactor; axisymmetric; detail of feed and product sections provided; white rectangle represents a solid quartz cylinder; white flow field in feed section is high velocity flow field.

The Tingey reactor also had a very high sweep efficiency, Figure 15. Small recirculation zones formed at the entrance of the annular section of the reactor, but the majority of the reactor volume was retained in this annular section where the reactor performed like a tubular laminar flow reactor. The flow of gases out of the annulus and toward the product port had small stagnant zones along the surfaces and no re-circulation zones. The RTD plot, Figure 17, is representative of a laminar flow reactor with dispersion, being very close to the ideal PFR behavior.

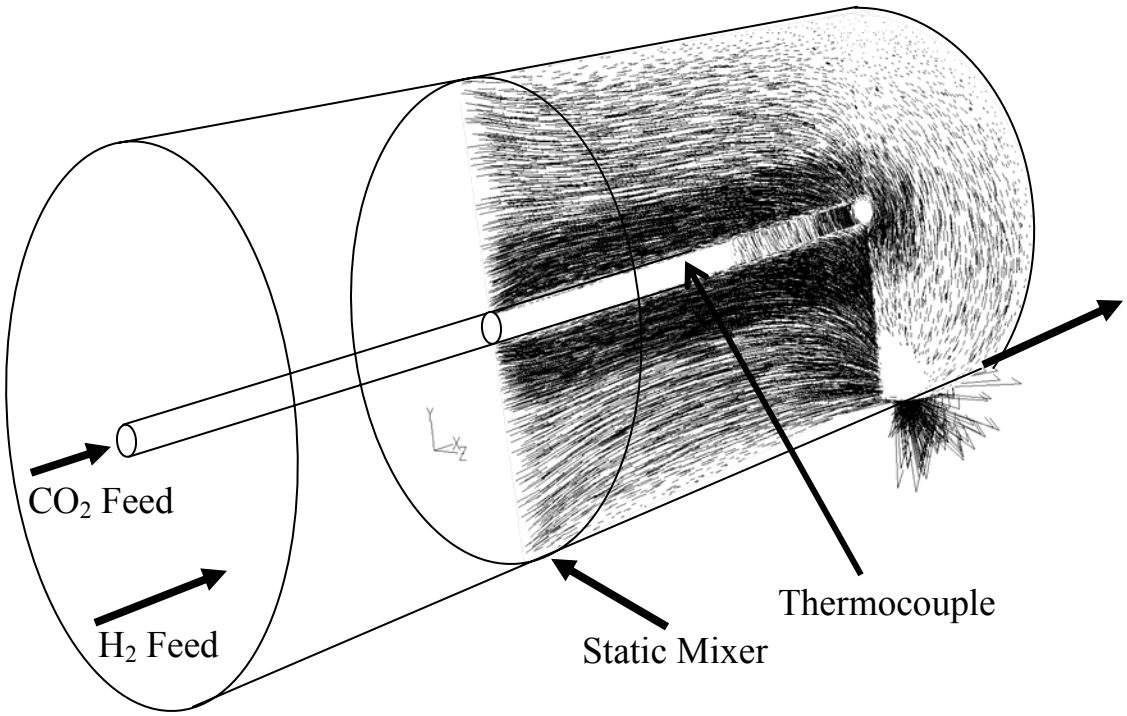


Figure 16 Kochubei and Moin; non-axisymmetric cylindrical reactor; axial feed along entire cross-section on the left-hand side of the reactor; product withdrawn through a narrow tube at the bottom right corner of the xz plane; white field in the center of the xz plane is a thermocouple; velocity vectors on a xy circular plane normal near the right-hand side of the reactor also shown; white field in this plane near the bottom corresponds to high fluid velocity near the exit tube.

The flow field of the Kochubei and Moin reactor, Figure 16, was similar to a laminar flow reactor. It exhibited high sweep efficiency and had no significant recirculation or stagnant zones, Figure 16. However, the broader RTD and its slight displacement towards lower times (Figure 17) confirms the channeling observed in the flow field at the bottom part of the reactor (Figure 16). There is a small effect of the stagnant zone as well, observed in the tailing of the RTD. It was assumed that the static mixer on the left-hand side of the reaction zone mixed the $CO_2$ and $H_2$ feed streams perfectly and instantly as they entered the reactor zone.

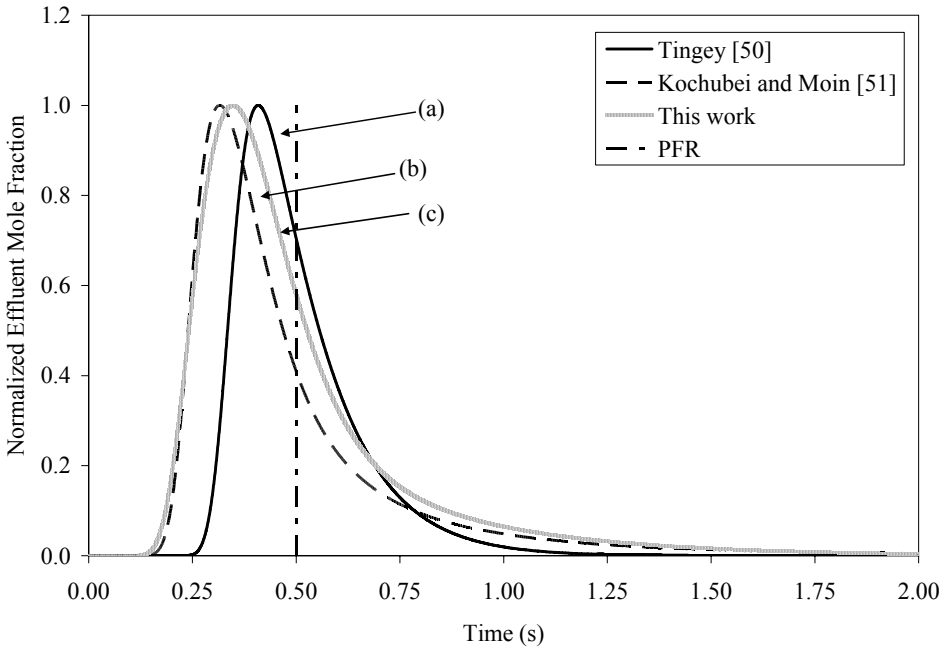


Figure 17. Residence Time Distribution plots for the reactors used in (a) Tingey[50], (b) Kochubei and Moin[51] and (c) this study. Nominal residence time is 0.5 s. Ideal case (PFR) reactor is included as comparison.

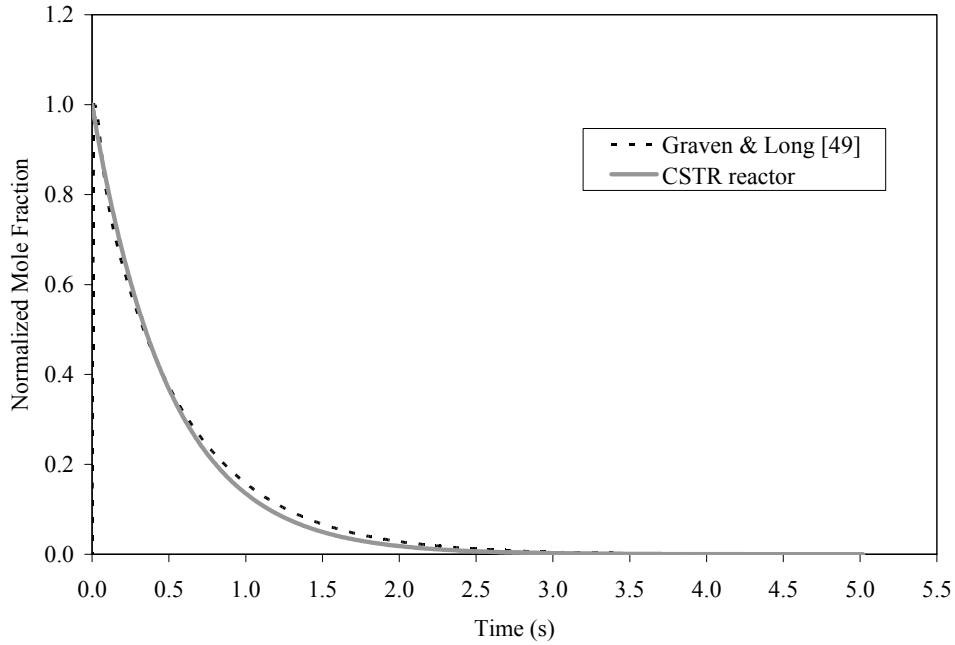


Figure 18. Residence Time Distribution plots for Graven and Long[49] reactor. Ideal CSTR reactor given as comparison.

Despite the almost ideal behavior observed in the reactors used by Graven and Long[49] and Tingey[50], there was a four-fold difference in the reaction rate constants reported by these investigators suggesting that the discrepancy was not related to the geometry of the reactor.

*Conversions of the rWGSR* The influence of reactor geometry on the kinetics results was also determined by modeling the rWGSR in each reactor. The rate of reaction was determined from Equation (2-7). The rate constant was obtained from Equation (2-6) using the values reported in the GRI database[58]. The reaction conditions were 1173 K, 0.1 MPa, equimolar feed of $CO_2$ and $H_2$, and a nominal residence time of 0.5 seconds. The results, shown in Table 5, indicate that the outlet concentrations were within 7% of one another, confirming that the reactor geometry was not responsible for the differences observed in the reported reaction rate expressions.

Table 5. CFD conversions of the four reactors assuming identical operating conditions and rate of reaction. Conditions: 1173 K, 0.1 MPa, residence time 0.5 s, inlet molar fractions of $CO_2$ and $H_2$ are 0.5.

| Reactor | $CO_2$ conversion, % |
|---|---|
| Graven and Long[49] | 0.0990 |
| Tingey[50] | 0.1017 |
| Kochubei and Moin[51] | 0.0990 |
| This work | 0.1053 |

*Effect of pressure on the quartz reactor results* Because all prior studies had been performed at ambient pressure conditions and there was a slight difference between the low-pressure and high-pressure results in this study, the effect of elevated pressure conditions employed in this study on the reaction kinetics was considered. The low-pressure experimental results of Tingey[50] and

Kochubei and Moin[51] are in excellent agreement with the value obtained from the Bradford mechanism by using the values for the rate constant of the elementary steps reported in the GRI database[58] in Equation (2-6): $k_1$, $k_{-1}$ and $k_2$, the rate constants of the initiation step (2-1), termination step (2-4), and forward reaction of propagation step (2-2), respectively. The ratio $k_1/k_{-1}$ represents the equilibrium constant of the hydrogen dissociation reaction, Reactions (2-1) and (2-4), and therefore is not pressure-dependent. Conversely, reaction (2-4) is known to display pressure-dependence[62,63,64] with the rate constant being proportional to the total pressure. However, the pressure dependence is very weak (less than 10%) under the temperature range of interest in this study. Therefore, the very small difference between the low-pressure and high-pressure results of this study was probably due to experimental uncertainties rather than changes in the reaction mechanism. Further, the difference of the low-pressure results from this study and the Tingey[50] and Kochubei and Moin[51] results cannot be attributed to the pressure difference.

*Effect of H and OH Not Being at Stationary State Conditions within the Reactor* The concentration of H and OH radicals within the reactor may not have been invariant as was assumed in the derivation of the expression for the overall rate constant, Equation (2-6). This effect was addressed to some extent in the prior investigations of the low-pressure rWGSR. Graven and Long[49] noted an induction period for the rWGSR, a common feature in chain-reaction chemistry. Kochubei and Moin[51] kept the $H_2$ stream at the reaction temperature for a time long enough (15 - 1000 s) to achieve a stationary state concentration of H (i.e., the equilibrium concentration from the $H_2$ dissociation (Eq. (2-1) and (2-4))) before mixing it with $CO_2$ at the reactor inlet. This is illustrated in the left hand side of Figure 16. Tingey[50] stated that the geometry of the reactor was changed to minimize the observed induction period which was

attributed to heating and cooling times as well as the time to achieve invariant concentrations of H and OH radicals within the reactor.

The possibility of changing concentrations of H and OH under our experimental conditions of rapid heating of a pre-mixed feed was studied using ChemKin® (Chemkin® is a software package for solving complex chemical kinetics problems. The application Creslaf, which models laminar flow in a tubular channel with homogeneous/heterogeneous kinetics was used. The transport data of all the species have either been calculated or collected from available web libraries.) The empty quartz reactor of this study, Figure 13, was modeled with a tubular laminar flow reactor of comparable dimensions (1 cm diameter, 1.6 cm long). The residence time of the simulations was maintained at values similar to the observed in the experiments by adjusting the volumetric flow rate. The elementary steps of the Bradford gas-phase mechanism were used as the input for ChemKin® and rate constant values were taken from the GRI database. Figure 19 shows the average molar fraction of H as a function of the distance along the reactor. The simulation indicates that the results in this study may have been influenced by the non-stationary state concentration of H which would vary significantly along the first fourth (0 - 0.4 cm) of the NETL reactor (1.6 cm total length). In the temperature range corresponding to the experiments, 1148 - 1198 K, the steady-state concentration of H was attained only at the latter section of the reactor, confirming that the initial transient period of [H] and [OH] values must be accounted for in determining the actual rate parameters of the reaction.

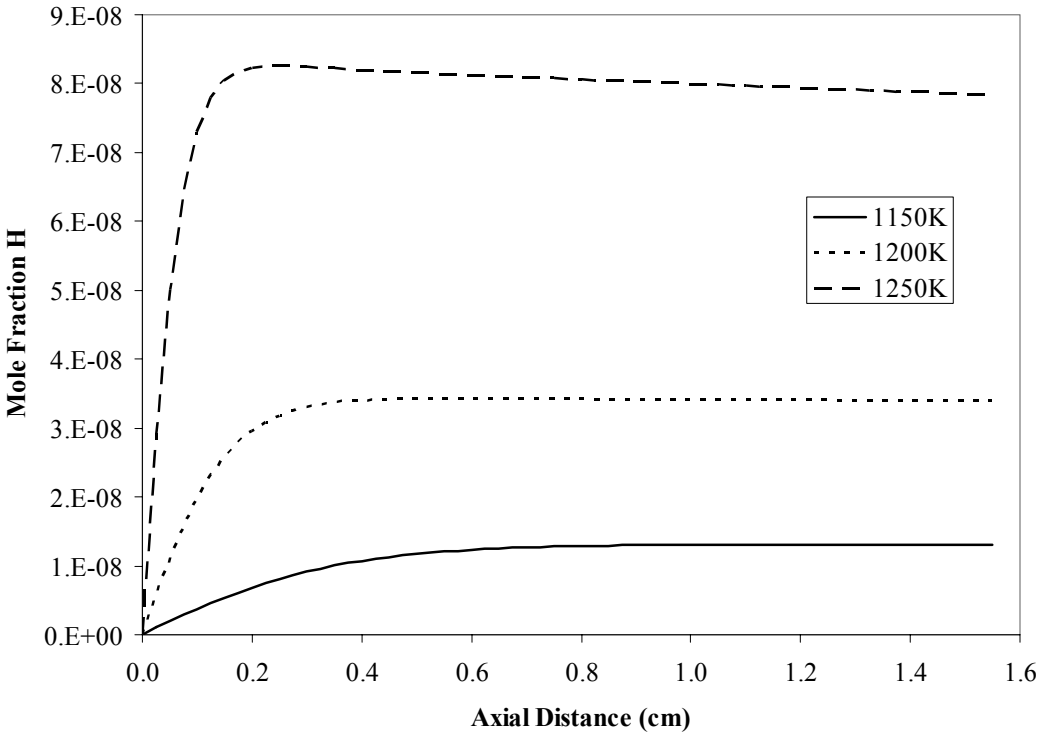


Figure 19. ChemKin® simulation of the rWGS in a tubular reactor. Inlet molar flowrates: $CO_2$ = $H_2$ = 50 sccm. Reactor diameter, 1 cm. Pressure, 1.6 MPa.

The Bradford mechanism was solved numerically to determine whether this induction period might have a significant effect on the overall reaction at low conversions. Stiff integrators (ODE23s from MatLab®) were used to solve the concentration-time profiles for each one of the six species involved in the reaction mechanism (see section 3.2.1). Figure 20 shows the concentration-time profile of H as a function of reaction time at 1250 K and 1.6 MPa, confirming the results from the ChemKin® simulation. The simulation was run until a $H_2$ conversion of 10% was obtained, which was low enough to minimize the effect of the opposite reaction. There was a continuous increase in [H] until the stationary state value was achieved at time greater than 0.5 s (conversion at t = 0.5 s is 1.86 %) suggesting that the period during which [H] changes plays a significant role in the gas-phase kinetics, especially for low reaction times/conversions. On the

other hand, [OH] (not shown) did not attain a stationary-state value even at large reaction times. However, its concentration was more than two orders of magnitude lower than [H] reflecting the preeminent role of [H] as chain carrier in agreement with Equation (2-6).

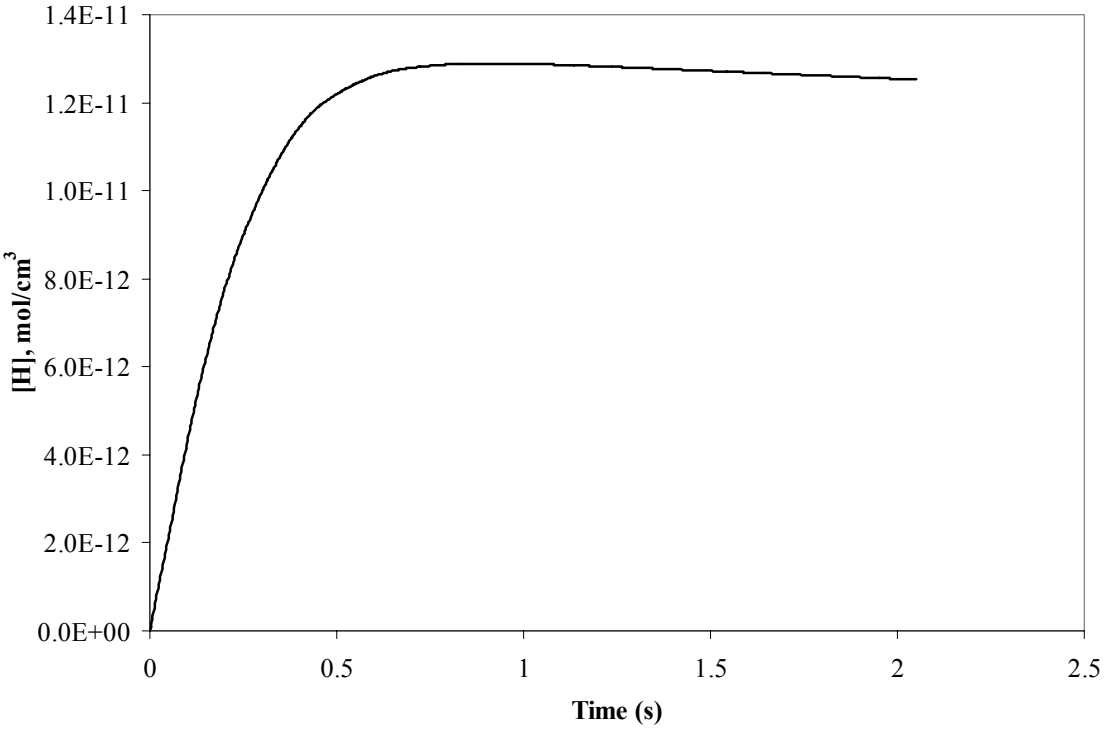


Figure 20. Concentration vs time profile for H species. $y_{CO2,0} = y_{H2,0}$, $y_{CO,0} = y_{H2O,0} = 0$, T = 1250 K, P = 1.6 MPa, final conversion is 10%.

The reaction rate expression derived from the Bradford mechanism is:

$$r_r = \frac{d[CO]}{dt} = k_2[CO_2][H] - k_{-2}[CO][OH] \qquad (4\text{-}1)$$

Equation (4-1) reduces to Equation (2-5) under steady-state concentrations of H and OH. The second term on the right hand side can be neglected for the early stages of the reaction because the concentration of CO is close to zero, $k_2$ and $k_{-2}$ are of the same order of magnitude, and [OH] is several orders of magnitude smaller than [H]. The reaction rate can therefore be simplified to Equation (4-2).

$$r_r = \frac{d[CO]}{dt} = k_2[CO_2][H] \tag{4-2}$$

From Equation (4-2) and Figure 20, it can be concluded that as the reaction commences, the rate of reaction *increases* (rather than decreases) with residence time because the increase in [H] is more significant than the decrease in $[CO_2]$. Once an invariant concentration of [H] is attained, however, the rate of reaction decreases with residence time as $CO_2$ is consumed.

If the reaction rate data is collected during this initial period and analyzed using Equation (2-7), (the rate expression obtained under the assumption of stationary [H]) the rate constant will be given by Equation (4-3) (obtained from combining Equations (2-7) and (4-2)). This rate constant will be an *apparent* rate constant rather than the *effective* rate constant of the rWGSR (Equation (2-7)).

$$k_r = k_2 \frac{[H]}{[H_2]^{1/2}} \tag{4-3}$$

The effect of the changing concentrations of H and OH on the magnitude of the reaction rate constant was determined for conditions of 1250 K and 0.1 MPa to provide an indication of

the significance of the non-stationary state condition on the interpretation of the results. The reaction rate constant was determined using (a) Equation (4-3) and [H] and [$H_2$] values from the simulation during the initial non-stationary period (for instance, t < 0.5 s in Figure 20), (b) results from the simulation when stationary [H] is imposed at the beginning of the reaction (i.e., inlet [H] is the equilibrium value at that temperature), (c) results directly from the simulation of the Bradford mechanism where the simulation is allowed to run long enough for both the non-stationary state and stationary state regimes to be manifest, i.e. until stationary-state is achieved (the rate constant was determined by linear regression from runs varying the inlet [$H_2$] and [$CO_2$]), (d) the experimental correlation for the rate constant obtained in this study by analyzing our experimental rate data with Equation (2-7), (e) the GRI data in Equation (2-6), (f) the correlation of Tingey[49], and (g) the correlation of Kochubei and Moin[51]. Results are presented in Table 6. The simulation results that account for the changing concentrations of H and OH, entry (b), are of the same order of magnitude as our experimental results, entry (d), suggesting that if [H] varies during an experiment but this change is not accounted for (i.e. equation (2-7) is used to solve for $k_r$), then the $k_r$ values will overestimate the effective rate constant. This is a likely cause for the discrepancies between the data reported in this study and that of Tingey[50] and Kochubei and Moin[51]. Further, their rate constant values, entries (f) and (g), are in very good agreement with the simulation where steady-state [H] was fixed at the inlet of the reactor, entry (c). The presence of the non-stationary period where [H] has not yet attained its equilibrium value might also explain the results of Graven and Long, whose rate constant values lie between our correlation and the predicted value from the steady-state Bradford expression, Equation (2-6).

Table 6. Estimation of $k_r$ values at 1250 K and atmospheric pressure. γ is the global reaction order.

| | Conditions | $k_r$ $(cm^3/mol)^{\gamma-1}\ s^{-1}$ |
|---|---|---|
| a | Non-stationary [H] | 325 |
| b | Mixed, non-stationary and stationary [H] | 79 |
| c | Stationary [H] | 7.1 |
| d | This work | 44 |
| e | GRI, stationary [H] | 7.3 |
| f | Tingey[50] | 9.1 |
| g | Kochubei and Moin[51] | 9.0 |

An attempt to further verify that the presence of a non-stationary state regime at the reactor inlet caused an overestimation of the reaction rate constant was then made. It is well known that quartz surfaces act as radical quenchers for reactions involving H radicals. This would cause an increase in the rate of the chain termination via the additional wall reaction consuming H radicals. Simulations of the intrinsic kinetics (MatLab®) suggested that such an increase would bring the [H] to a stationary state earlier during the reaction. However, the value of the stationary [H] is lower than the predicted from the pure gas-phase reaction. This should render an energy of activation similar to the Bradford value, but with a smaller pre-exponential value. Such a possibility was studied using simulations (ChemKin®) and an experiment with a quartz-packed quartz reactor. The temperatures were chosen in the interval where surface reactions appear to have some effect on the rWGSR, i.e. 1073 - 1123 K[50,51].

The radical quenching effect was modeled by adding the surface reactions suggested in the work of Aghalayam and coworkers[65] to the Bradford mechanism. However, the kinetic parameters available, i.e. the sticking coefficient, only provide an upper bound for the effect of

radical quenching. Consequently, the simulation predicted a large inhibition in the rate of reaction even at high temperature (>1148 K) where such inhibition has not been observed experimentally[49,51]. Therefore, no reliable estimation could be obtained from these calculations.

Figure 21 presents the experimental results from the quartz reactor packed with small cylinders of quartz that increased the quartz surface area by a factor of three. The experimental correlation, Table 4, was extrapolated to the 1123 - 1223 K temperature range to facilitate the comparison with our previous empty reactor results. CFD simulations of this packed reactor, in which the packing was modeled as porous media, yielded macroscopic flow patterns nearly identical to those shown in Figure 13. The rate constant for the quartz-packed quartz reactor was similar to the results of Tingey[50] and Kochubei and Moin[51]. This observation appears to corroborate the hypothesis that the suppression or minimization of the period of the reaction where [H] increases considerably, brought about by the radical-quenching effect of the quartz surface at moderate temperature, prevents an over-estimation of the rate constant. However, we could not reconcile the observation of Kochubei and Moin[51] of a small enhancement in the reaction rate brought by the addition of quartz packing. The high inlet [H] in the work of Kochubei and Moin would reduce the impact of the radical quenching, however. Further, the removal of H radicals from the gas-phase could eventually drive the chain initiation step towards the production of H, decreasing the concentration of $H_2$.

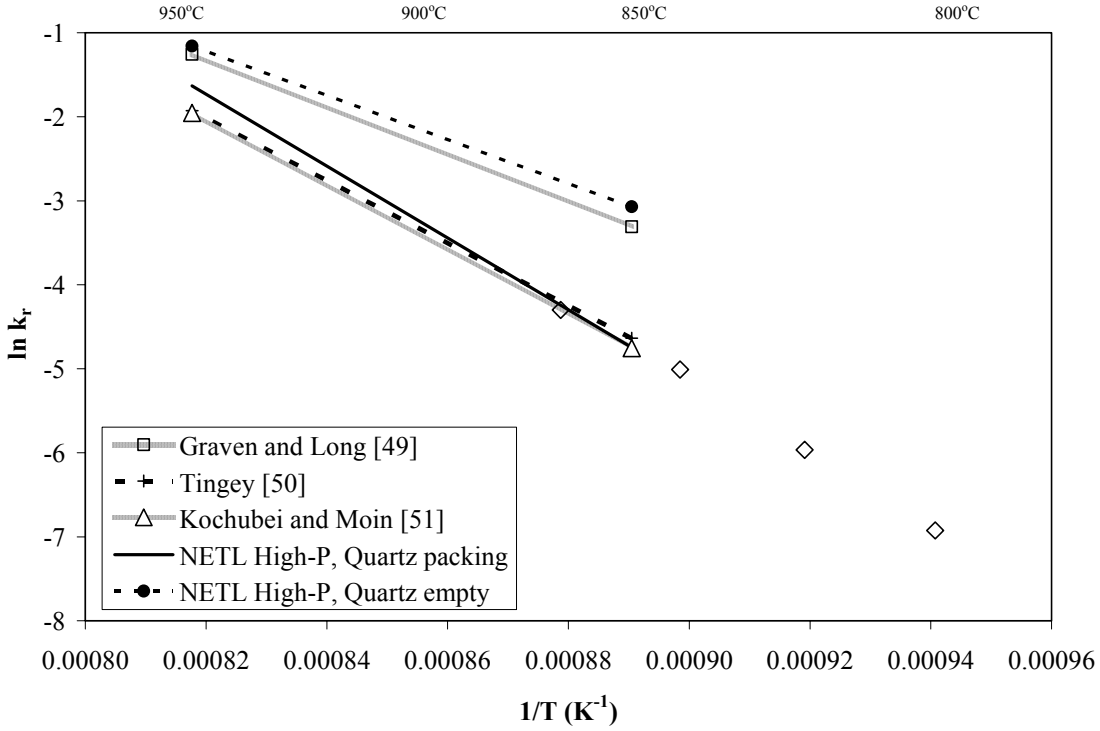


Figure 21. Arrhenius representation of rate constant for the high-pressure (1.6 MPa) reverse WGS reaction in the quartz packing reactor, $r_r = k_r[CO_2][H_2]^{0.5}$, $k_r$ $[L^{0.5}mol^{-0.5}s^{-1}]$. The actual data points are represented by open diamonds, while the solid line represents their extrapolation to higher temperatures.

## 4.2 KINETIC STUDY OF THE HIGH-TEMPERATURE FORWARD WGSR IN QUARTZ REACTORS

*Low pressure experiments* While studying the high-temperature, low-pressure fWGSR, it was critical to minimize the deposition of carbon inside the reactor. Figure 22 shows that if the reaction was conducted for a long period of time at a low $CO/H_2O$ ratio, a continuous increase of the rate of reaction was observed and significant deposits of carbon were detected throughout the reactor subsequent to the experiment. As illustrated in that figure, this effect was not significant until 10 hours had elapsed, after which the reaction rate increased steadily. Hadman and

coworkers[53] reported a similar effect, although they attributed it to the reactor surface becoming active for the reaction. Further, Long and Sykes[54] reported that extracted charcoal (ash content lower than 0.04%) displayed a catalytic effect on the fWGSR. However, their results indicate that at high temperature (1100 K) the rate exponents for CO and $H_2O$ approached those derived from the Bradford mechanism (Equation (2-13)). Ingles[66] conducted a similar study using purified carbon (ash content, 0.15 wt %) instead of coal, confirming the observation of Long and Sykes[54] on the apparent predominance of the gas-phase mechanism at higher temperature.

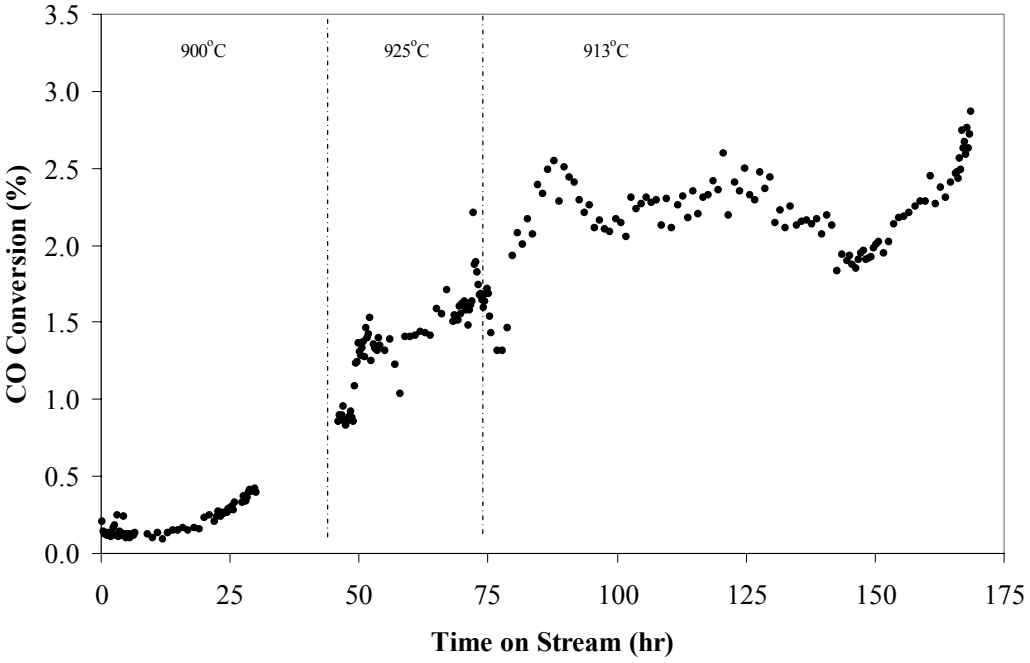


Figure 22. Increase of reaction rate with time on stream, fWGSR in a quartz reactor. P = 0.1 MPa. Residence time, 0.22 s. Inlet composition, $y_{CO} = 0.85$, $y_{H2O} = 0.15$, $y_{CO2} = y_{H2} = 0$. Only data collected during the initial reaction period (t<8 hours) were used in the kinetic study because they were considered to be unaffected by the accumulation of carbon.

Carbon is most likely due to the Boudouard reaction, Reaction (3-1). This reaction is exothermic and consequently is favorable at the moderately high temperatures predominating before the inlet of the reactor. In fact, visual inspection of the reactor revealed that the carbon deposits coated a 5 cm long section of quartz surfaces in the pre-heating section of the reactor, corresponding to the bottom of reactor detail shown in Figure 5a. The carbon particles found inside the high temperature reaction zone, where conditions did not favor the formation of carbon via the Boudouard reaction, were loose and the quartz surfaces were clean. This suggests that the carbon particles in the reaction zone actually formed in the pre-heating reaction zone and were carried by the gas flow into the reaction zone. All the kinetic data used in the elucidation of the fWGSR rate expression presented hereafter were recorded during periods of less than eight hours. Then a 2% $O_2$/Ar mixture was fed to the system until no $CO_2$ was detected, indicating that any carbon residue that had deposited was no longer present in the reactor. Before switching back to the reactant mixture ($CO/H_2O$), inert gas (Ar) was fed to the reactor for two hours to ensure a complete sweep of $O_2$ from the reactor. Although the inside of the reactor was clean, some residual carbon remained in the preheating section (temperature < 873 K); however, control experiments did not show conversion at that low temperature.

The high-temperature, low-pressure fWGSR was conducted in a quartz reactor, Figure 5a. The exponents of the CO and $H_2O$ concentrations in the rate expression were assumed to be 0.5 and 1.0, respectively, (the exponents predicted in Equation (2-13)) during the analysis of these low pressure experimental results. Rate constants were determined as a function of temperature, Figure 23. The scatter of the low-pressure rate constant data was primarily attributable to fluctuations in the volumetric flow rate of low-pressure steam through the reactor.

The rate constants appear to be similar to the low-pressure results reported by Graven and Long[49] and larger than the rate constant values evaluated from the Bradford mechanism and the GRI data. However the scatter of the low pressure data and the low conversions obtained (e.g., less than 0.2 %) prevent the estimation of a reliable correlation for the rate constant.

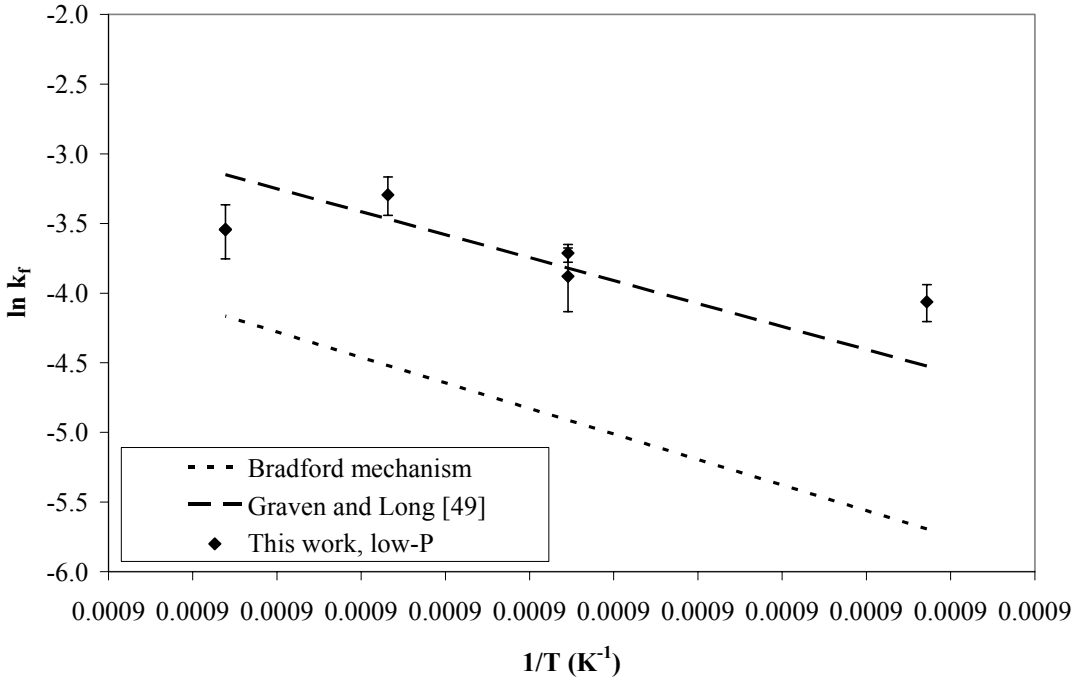


Figure 23. Comparison of the low pressure fWGSR results from this study with the results of Graven and Long[49] and the results obtained using Equation (2-14), which is based on the Bradford mechanism and individual reaction rate constants from the GRI database. Units of $k_f$ are $[(cm^3/mol)^{0.5}\ s^{-1}$.

*High-pressure experiments* High-pressure experiments were conducted to confirm the exponent values of the rate expression. The best concentration exponents for CO and $H_2O$, as obtained from linear regression, were 0.49 and 0.97, respectively. These values were very close to the values of 0.5 and 1.0 associated with the Bradford mechanism ( Figure 24 and Figure 25).

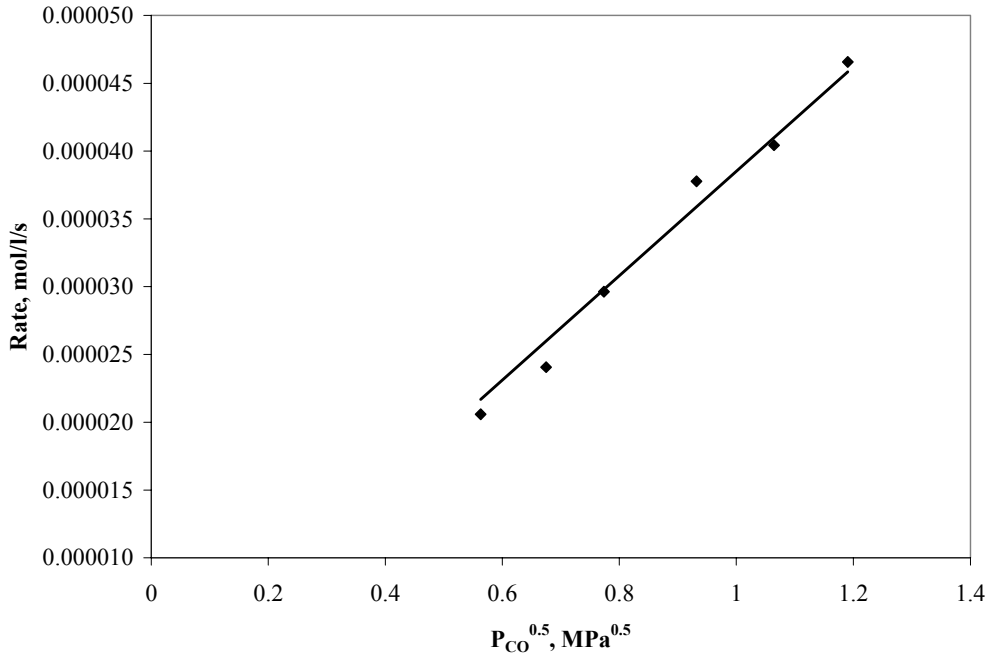


Figure 24. Rate expression exponent for CO. T = 1106 K. $P_{H2O}$ was kept constant at 0.2 MPa while the total pressure was varied from 0.4 MPa to 1.6 MPa; residence times were in the range 0.5 – 2.5 s.

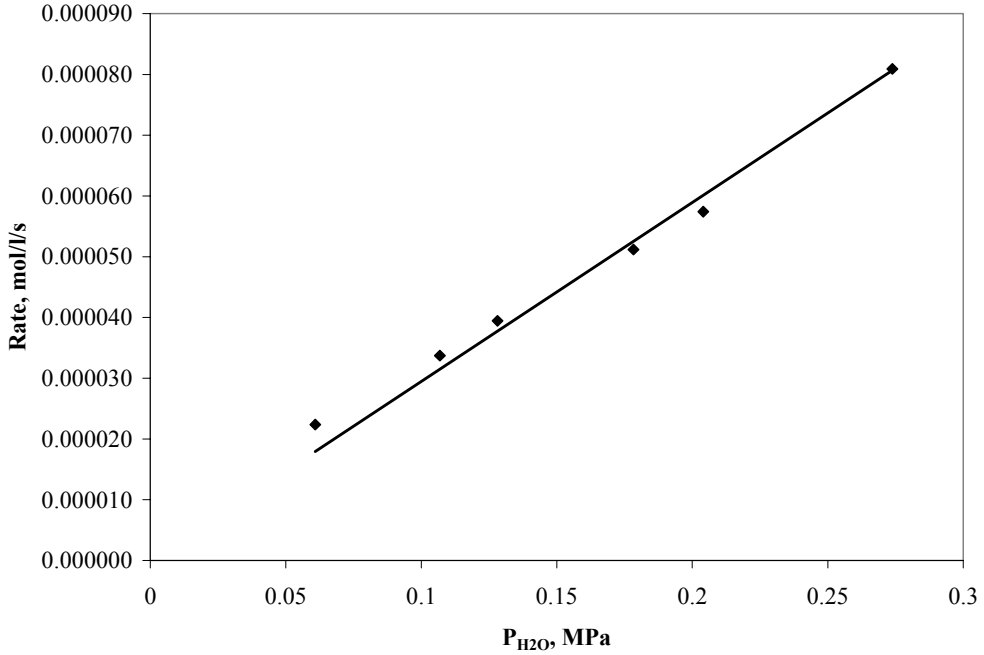


Figure 25. Rate expression exponent for $H_2O$. T = 1121 K. $P_{CO}$ was kept constant at 0.97 MPa while the total pressure was varied from 1.03 MPa to 1.25 MPa; residence times were in the range 1.3 – 2 s.

Having established the exponents of the CO and $H_2O$ concentrations in the reaction rate expression, the temperature dependence of the rate constant value was determined between 1071 and 1121 K. The results are provided in Figure 26 and Table 7. The activation energy of the NETL correlation is 60.6 kcal/mol [253.6 kJ/mol]; 17% less than the value of 72.8 kcal/mol [304.6 kJ/mol] associated with the Bradford mechanism/GRI database correlation and 7.6% less than the value of 65.6 kcal/mol [274.5 kJ/mol] reported by Graven and Long. The rate constant values of the NETL high-pressure correlation are intermediate to the Graven and Long correlation and the results obtained from the Bradford mechanism/GRI database using Equation (2-14). Finally, the effect of the high pressure on the reaction rate appears to be not significant.

Table 7. Kinetic expressions for the fWGSR – experimental and literature results. $r_f = (k_{0,f} e^{-Ea,f/RT})[CO]^{1/2}[H_2O]$

| Reference | T (K) | P MPa | $k_{0,f}$ $(cm^3/mol)^{0.5}\ s^{-1}$ | $E_{a,f}$ kJ/mol |
|---|---|---|---|---|
| Hadman et al.[53]* | 973 - 1073 | 0.1 | 2.22E14 | 319.2 |
| Graven and Long[49] | 1073 - 1373 | 0.1 | 7.97E12 | 274.5 |
| Bradford mechanism and GRI rate constants | 1100 - 1300 | 0.1 | 7.68E13 | 304.6 |
| This work | 1071 - 1121 | 1.6 | 4.82E11 | 253.6 |

* The rate constant was evaluated from the reaction time and conversion data reported in the reference, using the Bradford exponents for CO and $H_2O$.

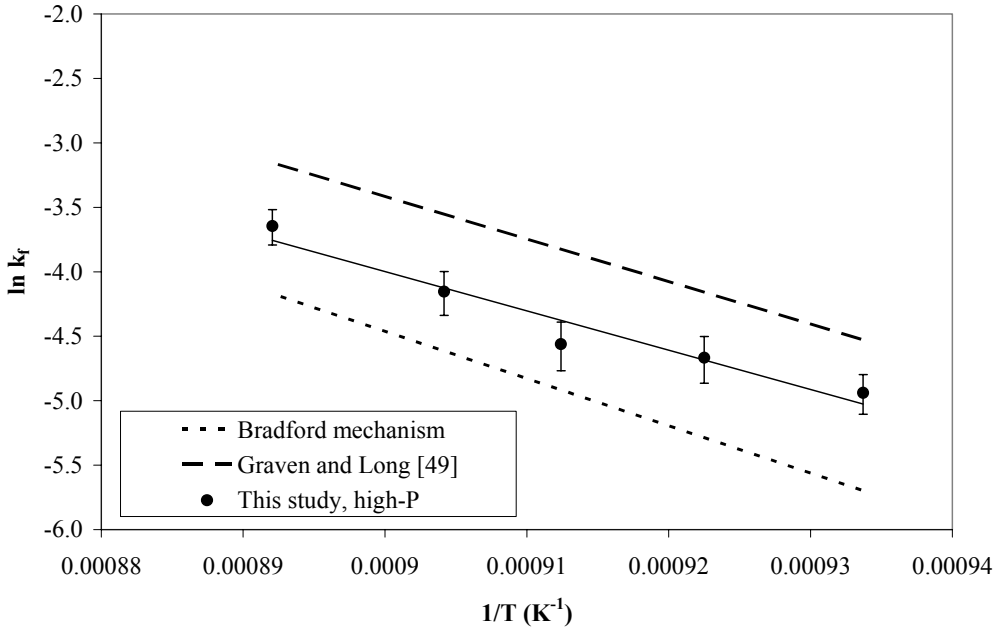


Figure 26. Arrhenius plot of the high-temperature, high-pressure (1.6 MPa) fWGSR in a quartz reactor. Units of $k_f$ are [$(cm^3/mol)^{0.5}$ $s^{-1}$]. Experimental correlation by Graven and Long and expected value from the Bradford mechanism are given as comparison.

The study of the kinetics of the high-temperature gas-phase reverse WGSR (section 4.1) showed that the experimental energy of activation reported in this study, as well as the value reported by Graven and Long[49], were significantly smaller than that predicted from the Bradford mechanism, whereas the rate constants were larger than the values derived from the mechanism. The difference was traced to the induction period where the increasing concentration of chain carriers with time would invalidate the assumptions used in the derivation of the rate constant from the gas-phase mechanism. A similar behavior, i.e. an induction period that would lead to the wrong prediction for the energy of activation, could be expected from the fWGSR. Simulation of the gas-phase Bradford mechanism for the fWGSR using stiff numerical solvers confirmed that under our experimental conditions (e.g., low reaction time) neither H nor OH would achieve their stationary-state value, as shown in Figure 27. Moreover, if the

concentration-time profiles from the simulations are used to evaluate the rate constant under conditions similar to the experiments (i.e., inlet concentrations, reaction time, reaction rate exponents), the resultant energy of activation (Ea ~ 340 kJ/mol) is *larger* and the rate constant *lower* than the corresponding values predicted from the mechanism. On the contrary, if the simulation is run under the constraint of inlet concentrations of H and OH close to their stationary-state values, rate constants that are in excellent agreement with the derivation from the Bradford mechanism are predicted. The results are summarized in Figure 28. This would indicate that there was an absence of a significant induction period in our experiments, i.e. a relatively high inlet concentration of H and/or OH radicals was achieved. Therefore we attempted to ascertain how such conditions could be established under our experimental conditions of rapid heat-up of the mixed feed gases.

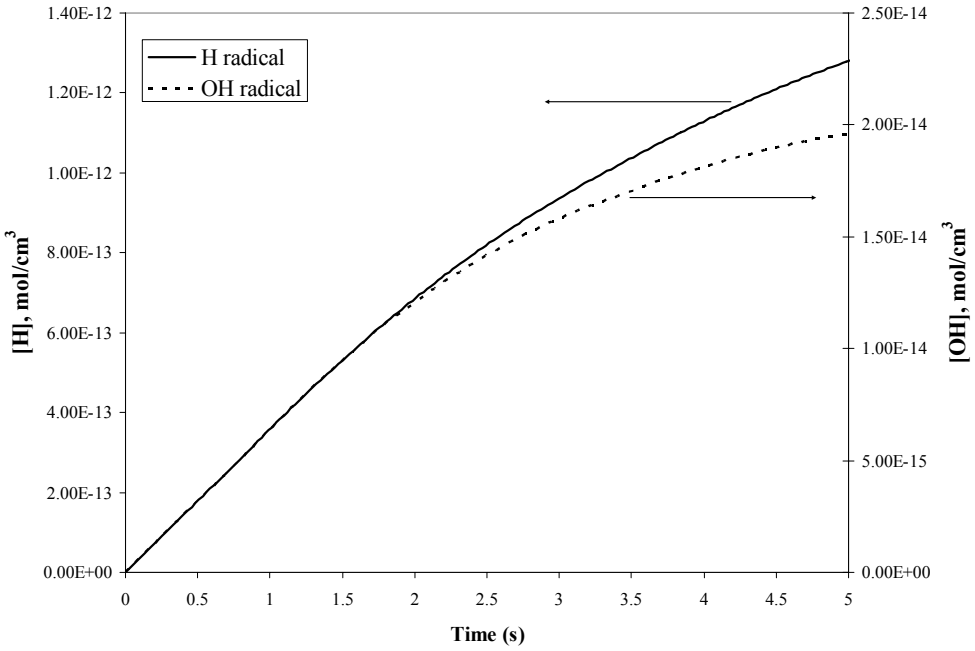


Figure 27. Concentration-time profiles for H and OH species as a function of reaction time as obtained by numerical solution of the Bradford mechanism. Temperature (1173 K), pressure (1.6 MPa), and inlet molar fractions ($y_{CO,0} = 0.77$, $y_{H2O,0} = 0.23$), similar to the experiments.

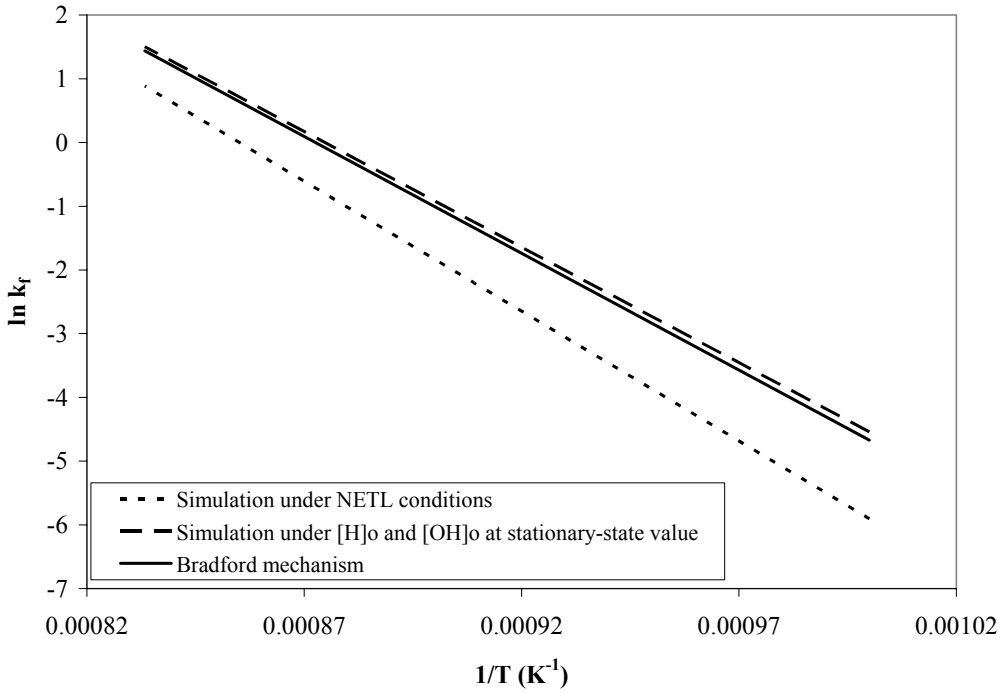


Figure 28. Arrhenius representation of the rate constant of the high-temperature fWGSR when the Bradford mechanism is solved numerically with and without forcing stationary state values for the concentration of H and OH at the inlet of the reactor. Correlation from Equation (2-14) (solid line) is given for reference. Units of $k_f$ are [$(cm^3/mol)^{0.5}$ $s^{-1}$].

The simulations also showed that at the temperature and residence time present in the preheating section, the formation of H and OH radicals from the gas-phase collisions of $H_2O$, Reaction (2-9), is extremely low and exerts a negligible effect on the high-temperature reaction. The interaction with the quartz walls in the preheating section would not give rise to a high concentration of radicals in the gas-phase because quartz would rather act as a radical quencher than as a radical source under the experimental conditions studied here[67]. On the other hand, Ingles[66] suggested that the enhancing effect of carbon could be explained by its acting as chain initiator for the gas-phase reaction. In fact, steam is known to adsorb on the loosely bound atoms in graphitic surfaces. Some early experimental work has suggested that the dissociation of the $H_2O$ molecule into H and OH is an intermediate step in the reaction between carbon and steam[68].

Recent computational chemistry simulations carried out by Zhu and coworkers[69] also suggest the dissociation of steam as an important step on the water-gas shift reaction on carbon surfaces. Although desorption of H or OH from the surface would provide a source of radicals at the inlet of the reactor, reducing the induction period, the results of Zhu and coworkers indicate that this is not energetically favorable.

A more detailed characterization of the carbon that coated the quartz surfaces of the preheating section was conducted in an attempt to determine why there was not a significant induction period and why our reaction rates were slightly greater than expected from the Bradford mechanism. X-Ray Diffraction, XRD, analysis showed the carbon deposit to be somewhat graphitic. Scanning Electron Microscopy combined with Energy Dispersive Spectroscopy, SEM-EDS, analysis revealed the presence of small amounts of nickel and iron dispersed throughout the carbon. Iron agglomerates in particles of irregular shape (approximately 30 μm in diameter), while nickel appears to be finely dispersed submicron particles. XRD study of the sample indicated the presence of iron silicate and metallic nickel in the carbon. It is recognized that silica is volatile in the presence of steam at high temperatures[70] which could lead to the formation of $Fe_2(SiO_4)$. Figure 29 illustrates the SEM image of one section of the deposit. Although the information extracted from analyzing one zone may not be representative of all the carbonaceous deposits, the results can provide insights into the behavior of the system. Three different zones are observed: a clean quartz surface, a thin iron layer on top of the quartz surface, and a layer of carbon deposit on top of the iron layer. A closer inspection of the last layer showed the presence of finely dispersed nickel particles. With our current instrumental resolution, it is not possible to determine whether the nickel is on or underneath the carbon surface but the latter option seems more likely. Additionally, analysis of loosely bound

carbon deposits downstream in the reaction zone (i.e., perhaps transported by the flow), Figure 30, did not show the presence of nickel or iron. A likely source of the nickel (and iron) deposited in the preheating section could be the formation of nickel (and iron) carbonyls in the CO-rich stream in the inlet stainless steel tubing as reported by Miksa and Brill[71]. Nickel carbonyl would then readily decompose in the hotter quartz tubing. Sykes and coworkers[72] studied the decomposition of nickel and iron carbonyls (formed in the cold end of stainless steel lines) on the surfaces of gas-cooled nuclear reactors at high pressure (4.1 MPa) and moderately-high temperature (623 – 973 K). They reported that nickel carbonyl promotes the deposition of carbon by forming nucleation centers in the form of small nickel particles. Once the centers are covered by carbon, the deposition process is stalled. Iron carbonyls, on the other hand, do not exert the same effect and the iron is present as agglomerates of small particles. This qualitatively agrees with our experimental observation. Moreover, the presence of nickel finely dispersed in carbon could explain why there appeared to be no significant induction period and why the conversions obtained in this study were slightly greater than those expected from the Bradford mechanism. Figuereido and Trimm[73] reported that the presence of nickel dispersed on carbon had a strong catalytic effect on the rate of carbon gasification by steam, with small conversions to $H_2$ and $CO_2$ at temperatures as low as 867 K. As the reaction rate and rate constant were evaluated using the conversion of water, formation of small amounts of hydrogen on the carbon deposited on the preheating section would lead to the over-prediction of the conversions and the rate constant.

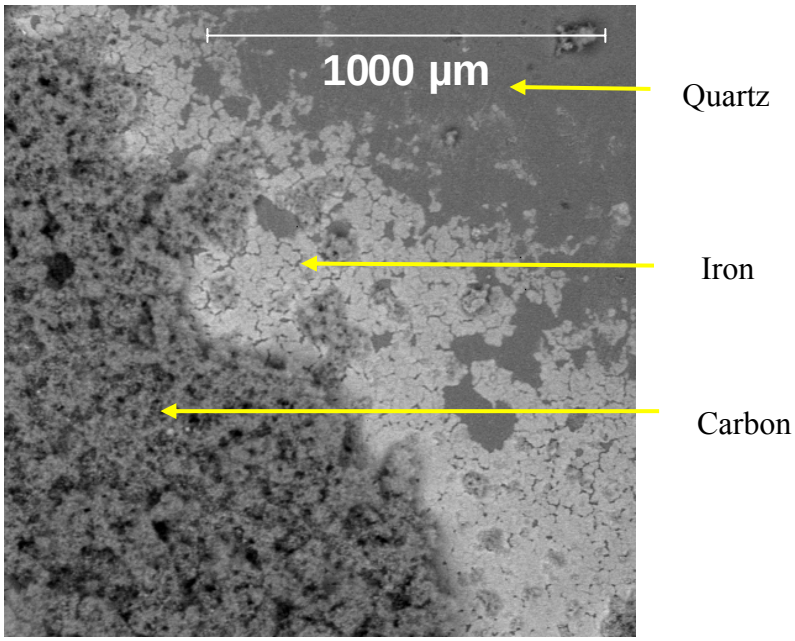


Figure 29. SEM-EDS characterization of the carbon deposit on the preheating section.

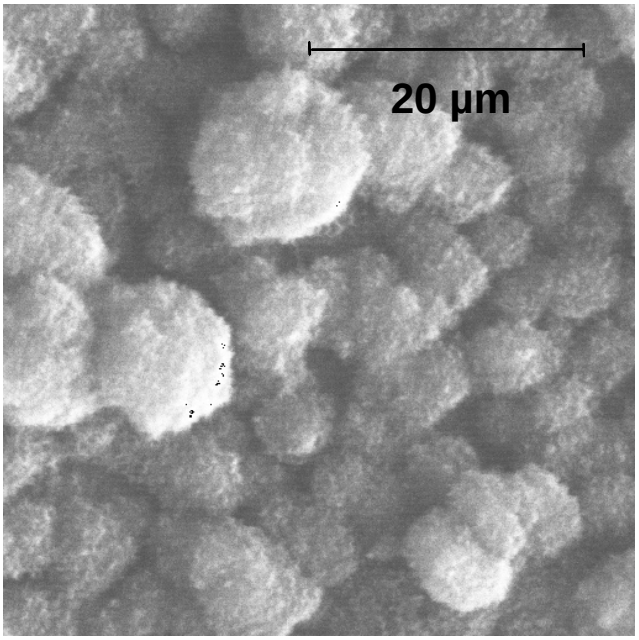


Figure 30. SEM image of the carbon particles deposited at the inlet of the reactor.

## 4.3 THE WGSR IN INCONEL®600 REACTORS

### 4.3.1 Reactant conversions

*Low-pressure reverse WGSR in an Inconel®600 reactor* The rate of reaction in quartz vessels provides an understanding of the intrinsic kinetics of the WGSR. However, industrial application of this technology will occur in vessels where the reacting gases will be exposed to the metal surfaces within the reactor. Therefore, the catalytic wall effects on the rate of the rWGSR were evaluated for empty and packed Inconel®600 reactors at 1173 K and 0.1 MPa using an equimolar feed of $CO_2$ and $H_2$. Conversions were very high (10-40%), given the short residence time (< 0.5 s) and the equilibrium limitation of 55%, as shown in Figure 31. These levels of conversion were approximately two orders of magnitude greater than those observed using the quartz reactor, which were less than 0.1% under the same experimental conditions. This result implied that the metal walls of the Inconel®600 reactor catalyzed the reaction. An increase in the Inconel®600 surface area was achieved by packing the reactor with Inconel®600 rings. As shown in Figure 31, the conversions were twice that observed with the empty Inconel®600 reactor. However, this difference could also be due to poor reactant mixing in the Inconel®600 reactor. In fact, these experiments were initially performed in a system where $CO_2$ and $H_2$ were fed separately into the reactor in an attempt to minimize the contact time with metallic surfaces. Subsequent experiments described in this section were carried out in the reactor configuration illustrated in Figure 5b where reactants were mixed before the inlet of the reactor.

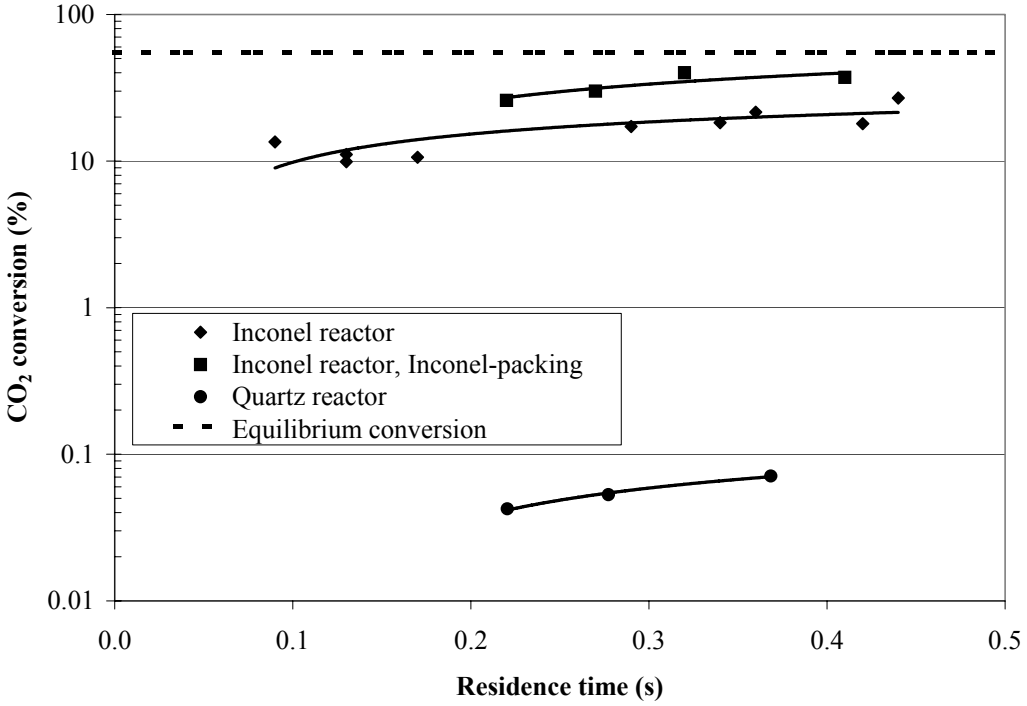


Figure 31. Reverse water-gas shift reaction in an Inconel®600 reactor. T = 1173 K, P = 0.1 MPa, $y_{H2,0} = y_{CO2,0}$, $y_{CO,0} = y_{H2O,0} = 0$. Equilibrium conversion at these conditions is 55%.

*High-pressure reverse water gas shift reaction in an Inconel reactor* The rWGSR was also conducted at high-pressure conditions in the Inconel®600 reactor depicted in Figure 5b over a wide temperature range using equimolar feeds of $CO_2$ and $H_2$. Longer residence times were employed (8-10 sec) because of the increase in gas density and limitations on the maximum flow rate of the reactor effluent, e.g. ~ 300 sccm. Results are presented in Figure 32 along with the predicted gas-phase conversions, e.g. in a quartz reactor. The rate of reaction in the Inconel®600 reactor was significantly greater than that obtained in the quartz reactor, especially at low temperature. Moreover, near-equilibrium conversions were attained at temperatures greater than 873 K in the Inconel®600 reactor. These results confirm the observations obtained under low-pressure conditions, Figure 31, namely that Inconel®600 surfaces catalyze the rWGSR. Levels

of conversion were so high that accurate kinetic expressions could not be derived for the reverse WGS reaction in an Inconel®600 reactor; however, an attempt to obtain a quantitative description of the catalytic effect of Inconel®600 was conducted (see section 4.3.4). Although a residence time of 10 s was used in this study, the residence time needed to achieve this level of conversion may have been substantially less, especially at higher temperature.

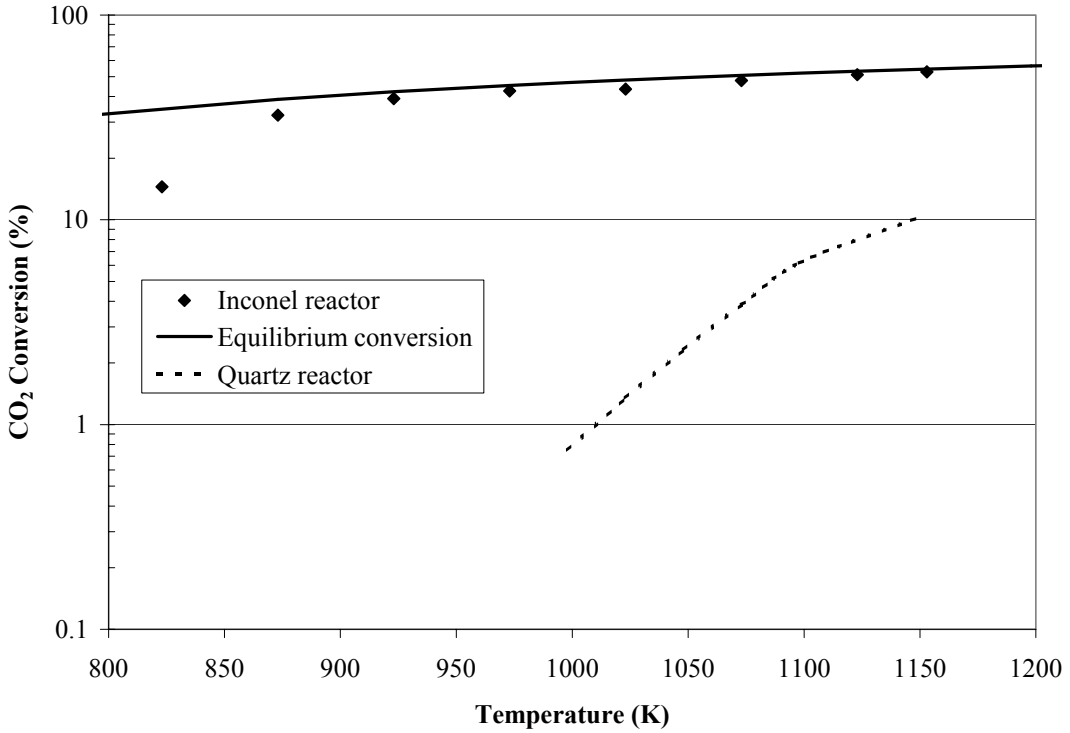


Figure 32. Reverse water-gas shift reaction in an Inconel®600 reactor. P = 1.6 MPa, $y_{H2,0}$ = $y_{CO2,0}$, $y_{CO,0}$ = $y_{H2O,0}$ = 0. Conversions in the quartz reactor were estimated with Tingey's high and low temperature correlations[50]. Residence time in the range 8-10 s.

*Low-pressure forward WGSR in an Inconel reactor* The forward WGSR was also conducted in an Inconel®600 reactor. Low-pressure conditions were used to determine the approach to equilibrium at low residence times. Figure 33 shows that for residence times of 0.5 – 1 s equilibrium conversions are attained for temperatures as low as 973 K in the Inconel®600

reactor. Further, the fact that the conversions correspond to the equilibrium conversions at the reactor temperature suggest that, both for the reverse and forward WGSR in our experimental apparatus, the extent of reaction downstream from the reactor is negligible.

These results indicate that if the design of a membrane reactor with a metal shell incorporates reaction rates based on correlations obtained with quartz reactors, then the reaction rate will be underestimated and the reactor volume overestimated if any part of the membrane reactor is reaction-rate limited. Further, this catalytic effect may mitigate or eliminate the need to introduce a packed bed of heterogeneous catalyst particles into the reactor.

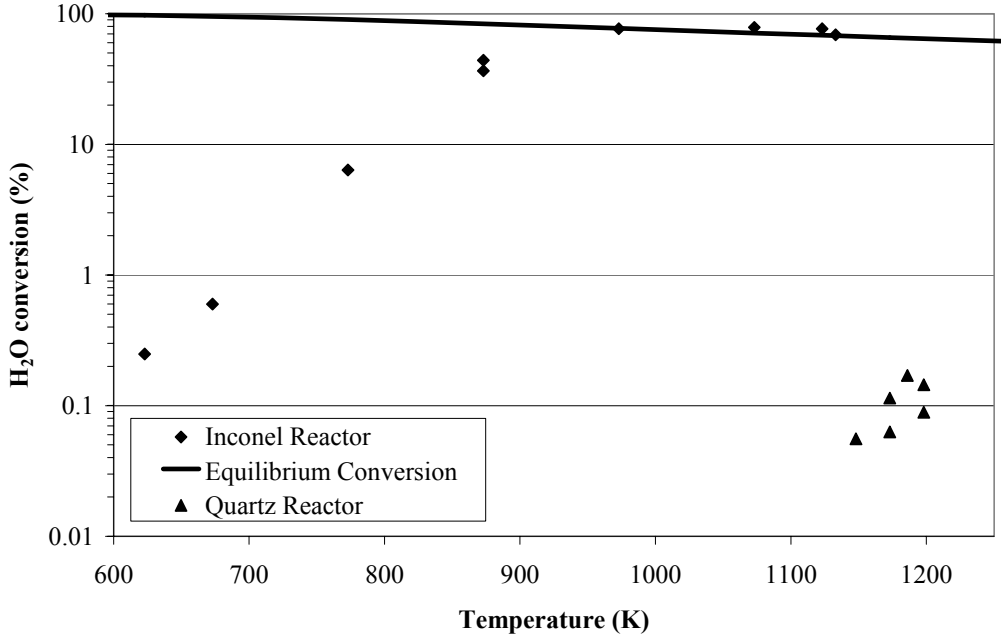


Figure 33. Low-pressure (0.1 MPa) fWGSR in an Inconel®600 reactor. Inlet composition, $y_{CO}$ = 0.77, $y_{H2O}$ = 0.23. Residence time below 0.5 - 1s.

### 4.3.2 Characterization of Inconel®600 surfaces after the WGSR

Both the low-pressure and high-pressure results indicated that the Inconel®600 catalyzed the WGSR. Two rings of Inconel®600 packing (approximate composition, 72% Ni, 17% Cr, and 10% Fe) were analyzed by SEM-EDS before and after their use in the low-pressure rWGSR, Figure 34. Significant loss of Ni and/or enrichment of Cr occurred in the Inconel®600 surface after exposure to the rWGSR environment. (The Al, Si, and Ti detected in the rings reflect the composition of the Inconel®600; the source of the Ca is not known but could be due to surface contamination.) A probable cause of Ni loss is the so-called "metal dusting". This type of corrosion is characterized by mass loss due to the formation of carbon deposits in $H_2$-CO-$H_2O$ environments in the temperature range 673-1073 K*. The carbon diffuses into the metal and the nickel migrates to the surface forming small pure-nickel particles. Inconel®600 has been reported to be susceptible to this kind of attack[74]. Although the mass loss in Inconel®600 associated with "metal dusting" is more considerable than for other high-Ni alloys, the damage appears to be more superficial[75]. The formation of carbon deposits could be attributable to the Boudouard reaction (Eq. (3-1)), due to the somewhat large CO concentrations present in the system.

However, the catalytic effect of Inconel®600 is manifest both with the reverse and forward WGSR in spite of the lower CO concentration and larger CO/$H_2O$ ratio in the former, i.e. the forward WGSR would provide a more favorable environment for the deposition of carbon

* The transfer of Ni from the stainless steel tubing to the quartz reactor inlet described in section 2.3.2 is not caused by metal dusting. In metal dusting, the extraction of Ni is associated with carbon deposition rather than with the formation of nickel carbonyls.

and occurrence of metal dusting. This prompted a more careful examination of the Inconel®600 tube after the reaction to gain insight on the interactions between the metallic surface and the gas mixture. For instance, it is known that Ni-rich alloys can form self-healing passivation layers of chromium oxide by treatment in wet environments at high-temperature (1373 K)[76]. Therefore, the loss of nickel from the surface of the Inconel®600 rings could also be due to the formation of such a passivation layer. SEM-EDS and XRD characterization of the reactor wall were used to explore this possibility. The surface composition was contrasted with the bulk composition in different sections of the reactor. Three samples (e.g., 1 cm long rings) were cut from the Inconel®600 walls after the fWGSR for this purpose. The cross section of the samples was polished for the SEM-EDS study. Some samples were then pressed flat for subsequent XRD study. The first ring was taken from the reaction zone (close to the top of the reactor, Figure 5b), the second from the preheating annular space close to the border of the heater, and the last one from the cold end of the reactor. The piece extracted from the reaction zone (i.e., the inner surface in the high-temperature section of the reactor) revealed the formation of a thin chromium-rich layer on the surface of the material (Figure 35a); the bulk composition corresponds to that of Inconel®600. Due to the partial overlap of oxygen and chromium peaks in the SEM-EDS it is not possible to establish whether the chromium was present as an oxide. However, XRD confirmed the presence of chromium oxide in addition to Inconel®600. Consequently, the chromium oxide is most likely in the form of a layer on the surface of the material. On the contrary, analysis of the outer surface (not exposed to the reaction gases) by XRD showed the presence of a thinner layer composed of chromium oxide, nickel oxide, nickel-chromium oxide, and possibly nickel-chromium-iron oxide, attributable to high-temperature atmospheric oxidation. Therefore, the formation of the relatively thick (in the micron size range)

chromium oxide layer on the inside wall is due to the high-temperature WGSR environment. Further, the depletion of nickel from the Inconel®600 rings would be also attributable to this cause. The second sample was extracted from the region where carbon deposits were more significant, i.e. the preheating section. The SEM-EDS analysis showed that the Ni/Cr ratio was lower on the surface than in the bulk of the wall. Moreover, surface damage is observed on the inner wall (Figure 35b). Closer analysis of the surface revealed that the composition is not homogeneous. There are peak-shaped areas that are Ni-rich (e.g., Ni/Cr ratio is significantly higher than in the bulk of the material) separating valley-shaped Cr-rich zones. The former appear to be growing from the surface. This behavior is consistent with carbon diffusion into the Inconel®600 causing metal dusting on the surface. Indeed, SEM-EDS inspection of the carbonaceous deposit demonstrated the presence of Ni as finely dispersed sub-micron size particles. Consequently, the metal dusting occurs primarily at the preheating section and not at the reaction zone. In other words, when the reactor operates at very high temperature (~1173 K) the gases will encounter a chromium oxide surface on the reaction zone and not metallic nickel. Finally, the ring from the cold end did not exhibit any difference between the Ni/Cr ratio on the surface and that of the bulk; additionally, no evidence of surface attack was found. Therefore, it is possible to speculate that the catalytic effect displayed by Inconel®600 is due to the chromium oxide layer formed on the reactor walls.

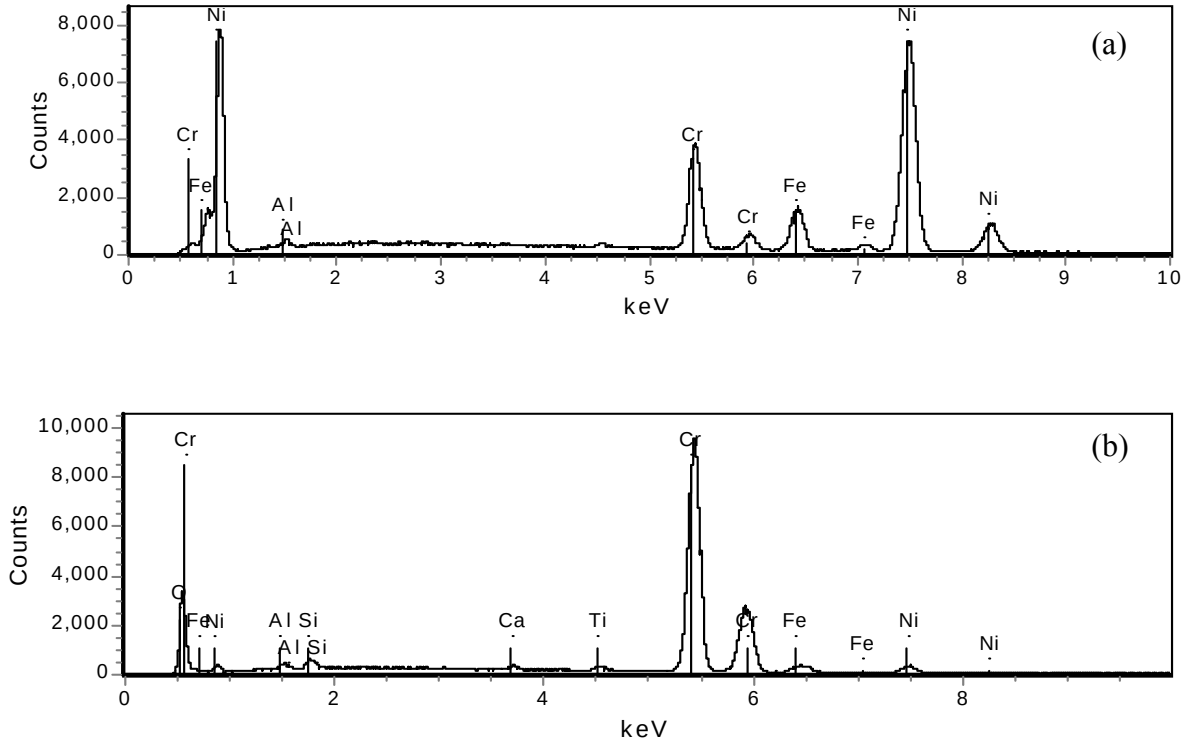


Figure 34. SEM-EDS analysis of the Inconel®600 rings before (a) and after (b) exposure to *reverse* WGSR environment.

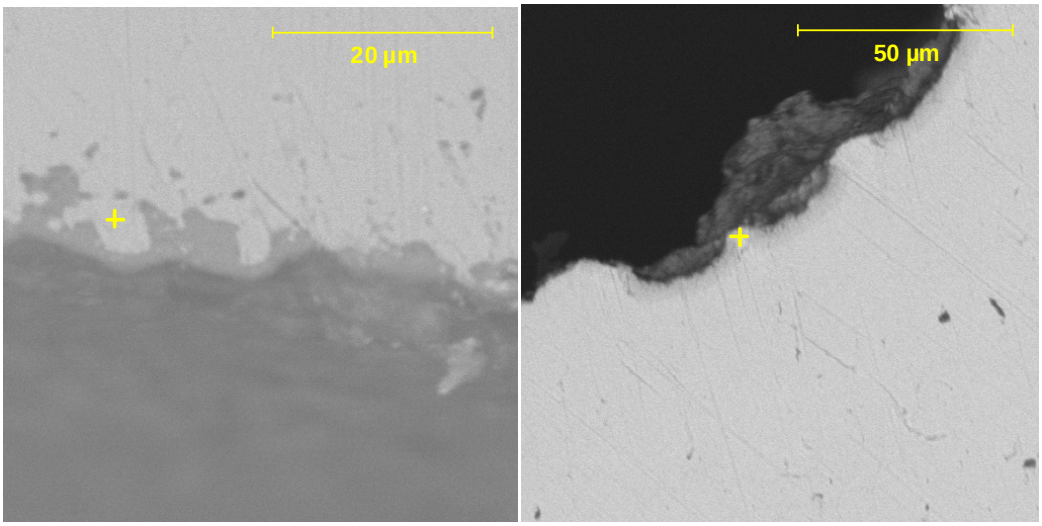


Figure 35. SEM cross-sectional image (backscatter mode) of the Inconel wall in the reaction section (a) and in the preheating section (b). The light grey area on the normal plane on image (a) corresponds to Inconel (Ni, Cr, Fe), and the dark grey area to chromium oxide. The darker areas on image (b) correspond to coke deposit. The pattern of valley-like shape separated by peak-like formations is repeated throughout the wall surface.

### 4.3.3 Side reactions in the WGSR in Inconel®600 reactors

Aside from the Boudouard reaction, the formation of methane was observed both for the reverse and forward WGSR in the Inconel®600 reactor. The concentration of methane at the outlet of the reactor exhibited temperature dependence reaching a maximum value at 1023 K, as shown in Figure 36 for the *reverse* WGSR (results for the forward reaction were similar). Methane formation in a CO-$CO_2$-$H_2$-$H_2O$ system is possible via reactions (4-4) – (4-7). The fact that the CO/$H_2O$ ratio decreases and the $CO_2/H_2$ ratio increases noticeably at 1023 K suggests that reaction (4-4) and/or (4-6) are playing an important role in the process. Removal of $H_2$ from the system led to complete suppression of methane formation. However, at the temperature at which the methane formation is maximum (973 – 1023 K) the conversion of CO via the Boudouard reaction is both kinetically and thermodynamically favorable, which would explain the formation of significant amounts of carbon. Therefore, methane would be formed by reaction of carbon and hydrogen, Reaction (4-7). This reaction, which is not thermodynamically favored at high-temperature, would be responsible for methane formation even at the temperature range where carbon formation is not favored due to the reactivity of the carbon-nickel deposits on the colder preheating section. This qualitatively agrees with the data collected during the experiments described in section 5.1. Methane production was observed when a CO/He stream was switched to $H_2$/He. Moreover, the concentration of methane at the outlet of the reactor was significantly larger than that expected from the equilibrium concentration of reaction (4-7) at the temperature of the reactor.

$$CO + 3H_2 \leftrightarrow CH_4 + H_2O \quad (4\text{-}4)$$

$$CO_2 + 2H_2 \leftrightarrow CH_4 + 2H_2O \quad (4\text{-}5)$$

$$2CO + 2H_2 \leftrightarrow CO_2 + CH_4 \quad (4\text{-}6)$$

$$C + 2H_2 \leftrightarrow CH_4 \quad (4\text{-}7)$$

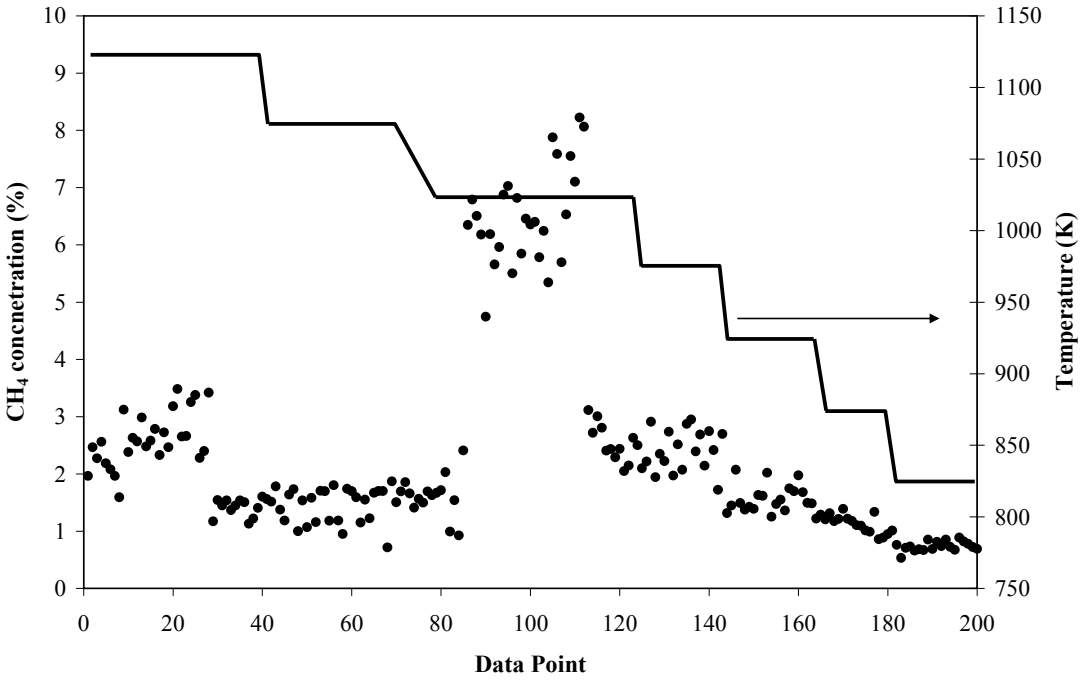


Figure 36. Side reactions in the WGS in an Inconel®600reactor. Formation of methane as a function of temperature. P = 1.6 MPa, $y_{H2,0} = y_{CO2,0}$, $y_{H2O,0} = y_{CO,0} = 0$. Residence time in the range 8-10 s. Samples were collected at 15 or 30 minutes intervals.

### 4.3.4 Attempt to determine the kinetic parameters of the WGSR on Inconel®600

The work in this project was directed primarily to the hydrogen-selective membrane reactor concept. A full kinetic study of the catalytic effect of Inconel®600 surfaces on the reaction rate was considered to be beyond the scope of the project. However, many industrial applications

deal with high-temperature, high-pressure streams where the water-gas shift reaction might have a large impact. As a consequence, knowledge of the effect of common construction materials on the water-gas shift reaction is desirable. Therefore, a simple series of tests was conducted to determine whether the Hydrogen Membrane Testing units, HMT, at NETL were suitable for the high-temperature, high-pressure kinetic study of the heterogeneous catalytic effect of common construction materials. Specifically, it was studied whether conversions low enough to preclude the effect of the opposing reaction but large enough to yield reproducible, kinetically-relevant results could be accurately determined for packing of known shape and surface area.

The quartz reactor depicted in Figure 5a was filled with quartz and Inconel®600 packing. Small cylinders —length, 3.5 or 4.2 mm— of Inconel®600 and quartz, respectively, were cut from solid rods (2 mm diameter) of each material. The total surface area of the Inconel®600 pellets was 3 $cm^2$. This surface area was selected so that conversions remained below 10% at the desired flow rate. (The surface area target was based on extrapolation from the conversions obtained in previous experiments where the Inconel®600 reactor -surface area, 18$cm^2$- was filled with quartz packing.) The quartz packing (in a ratio of approximately 3 quartz rods per Inconel®600 rod) was added trying to ensure a homogeneous distribution of the Inconel®600 packing throughout the volume of the reactor. The presence of quartz, being inert for the water-gas shift reaction at very-high temperature, should diminish the influence of mass-transfer limitations without affecting the kinetic activity of the Inconel®600.

A $CO/H_2/H_2O$ mixture was used for these experiments. The stream concentration, 29.0% CO / 55.5% $H_2$ / 15.5 % $H_2O$, was similar to the outlet composition of a gasifier. The HMT was

modified to accommodate a water-trap at the reactor outlet to condense the water. This was necessary to prevent the condensation in the lines stemming from the increased dew point at the operating pressure (the experiments were conducted at 2.8 MPa). Therefore, conversions were evaluated from the outlet CO and $CO_2$ concentrations after steady state was reached. Table 8 shows the conversions observed. The expected gas-phase conversion for the same residence time, inlet concentrations, and temperature is given for comparison.

The conversions in the Inconel®600-packed reactor are larger than the expected gas-phase conversions which clearly confirms the catalytic effect of the Inconel®600. The results follow the expected trend of decreasing conversions with decreasing pressure. A preliminary estimation of the energy of activation from the rate data gives the value 71 kJ/mol which is significantly lower than the corresponding energy of activation for the gas-phase reaction. A direct comparison of this result with commercial catalysts is not possible in view of the different temperature regime and packing structure (e.g., possible influence of mass-transfer limitations in our results). In addition, experimental set-up improvements are required to increase the accuracy of the result. Specifically, large variations in the flow rate at high-pressure were observed.

Table 8. Very-high pressure (2.8 MPa), high-temperature WGSR in an Inconel®600 & Quartz-packed Quartz reactor. All experiments carried out at the same residence time (~ 0.6 s).

| Temperature (K) | Conversion (%) | Error (%) | Gas-phase conversion (%) |
|---|---|---|---|
| 1073 | 0.62 | 2.3 | 0.003 |
| 1123 | 0.77 | 2.0 | 0.011 |
| 1173 | 1.20 | 1.7 | 0.035 |

## 4.4 EXPLORING THE EFFECT OF MEMBRANE MATERIALS (Pd AND A Pd-Cu ALLOY) ON THE GAS-PHASE WGSR

To isolate and assess the potential catalytic effect of membrane materials on the WGSR, a conventional (i.e. non-membrane) quartz reactor was packed with pure palladium or palladium-copper alloy (80 wt % Pd) in the form of small cylinders (2 mm diameter, 3 mm length). Surface-to-volume ratio was the same for the two types of packing. Corresponding experiments with the quartz reactor filled with quartz packing of similar dimensions did not show any effect of the packing on the reaction rate at the conditions studied (i.e., very high-temperature).

### 4.4.1 The Water-Gas Shift Reaction in the presence of palladium packing

Figure 37 shows the CO conversion of a series of tests conducted in the Pd-packed, quartz reactor. The 'x' axis indicates the order in which the tests were performed. Each set of data represents the average of the steady-state conversions recorded. In all cases the reaction was run for several hours after steady state was attained which was typically within the first hour of operation. However, the fresh packing displayed a slight trend of increasing conversions with time on stream during the initial hours of testing. The first data set shows a moderate increase in the reaction rate when the reactor is packed with Pd. This increase is very small and could be within experimental error (e.g. small deviations in the actual temperature inside the reactor). Studies on the behavior of the WGSR in supported catalysts stress the importance of the redox behavior of the catalyst/support system[77]. Consequently, at the high temperature (1173 K) and net reducing environment ($CO/H_2O$ ratio ~ 5) present during the reaction, no oxidation of Pd should be expected and the smooth Pd surface should behave like the quartz packing. However,

a significant increase in CO conversion is observed after treating the Pd packing in 2% $O_2$/Ar overnight (data set 2, Figure 37). Also, continuous testing for a large period of time (24 hr) without $O_2$/Ar treatment does not have the same effect on the observed conversions (data sets 3 and 4, Figure 37). Moreover, Figure 37 also shows that the repeated switching between oxidizing ($O_2$-rich) and reducing (CO-rich) environments enhances the reaction even further (data set 2 versus data set 3). On the other hand, this enhancing effect appears to be both directly proportional to the duration of the $O_2$ treatment and irreversible. Figure 38 compares the conversions observed in switching from high-pressure (data set 1) to low-pressure (data set 2) with a long (66 hr) intermediate $O_2$/Ar treatment. Despite the decrease in pressure, which should translate into lower conversions due to the lower residence time and inlet concentrations, conversions in the low-pressure regime are significantly larger.

The complexity of the Pd – $O_2$ system is recognized by the many papers written on the subject (see, for instance, Refs. 78,79,80). Pd-$O_2$ interactions are thought to lead to the formation of several oxygen-containing species --chemisorbed oxygen on the surface, surface palladium oxide, and bulk palladium oxide. Wolf and coworkers[80] modeled the behavior of polycrystalline Pd under oxidation/reduction cycles and suggested a complex relationship between these three types of Pd-O interaction. Even though PdO is not expected to be stable at low-pressure and temperatures greater than 973 K, some remaining chemisorbed O could still be present at the surface[80]. If these oxygen species are responsible for the enhancement on conversions, a sweeping of the reactor with a reducing atmosphere should somewhat decrease the conversions and partly restore the conversions observed with the fresh Pd packing. An attempt was made to study this possibility.

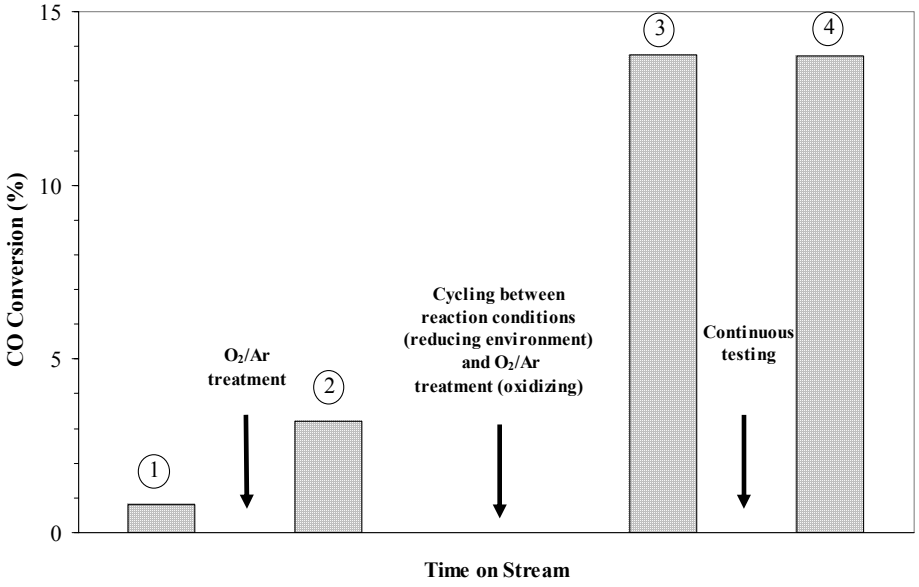


Figure 37. CO conversions for the forward WGSR in a Pd-packed, quartz reactor. P, 0.1 MPa. T, 1173 K (data sets 1 and 2) or 1123 K (data sets 3 and 4). $\tau$, 0.25 s. $y_{CO,0} \sim 0.64$, $y_{H2O,0} \sim 0.46$. Gas-phase conversions are below 0.3%. CO equilibrium conversion is 30 - 35%.

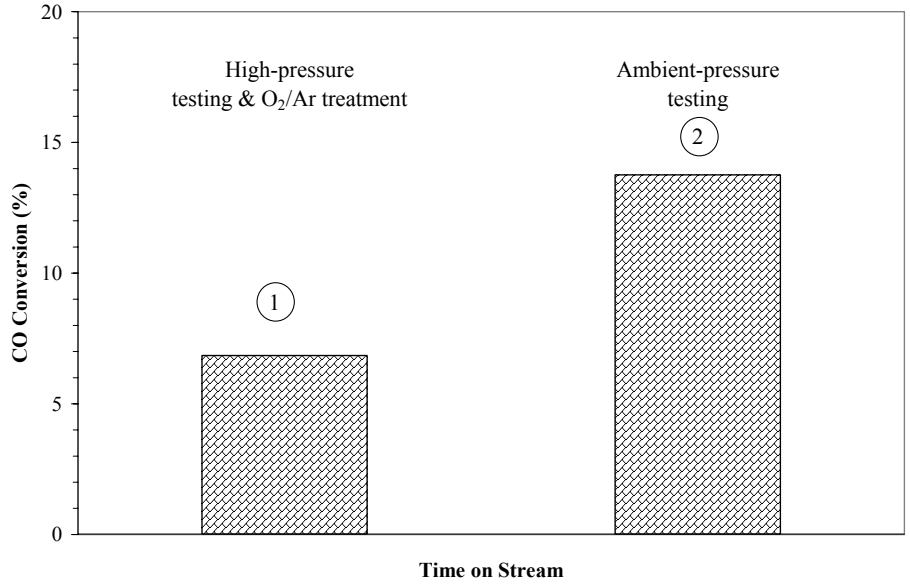


Figure 38. Effect of the duration of the $O_2$/Ar treatment on the conversions observed in the Pd-packed reactor. Packing was treated in the oxidizing environment for 66 hr between the two data sets. T = 1123 K. $\tau$: 0.22 s (low-pressure), 1.7 s (high-pressure). $y_{CO,0} \sim 0.78$ (data set 1) or 0.68 (data set 2). Gas-phase conversions, 0.3 - 0.75%. CO equilibrium conversion is 21% for data set 1 and 29% for data set 2.

After the $O_2$/Ar treatment, the reactor was flushed with He and then $H_2$/He was admitted to the reactor. No significant change in conversion was observed upon feeding CO/$H_2O$ after the reducing treatment. However, PdO is thermodynamically stable at the conditions of our high-pressure testing[81]. This bulk PdO could decompose and release oxygen to the surface[80]. Consequently, we oxidized the Pd packing at the high partial pressure of oxygen used in the $O_2$/Ar treatment ($P_{O2}$ = 0.03 MPa) and cooled down under inert. The packing was characterized by means of X-Ray Photoelectron Spectroscopy (XPS), XRD and SEM-EDS. XPS results of the as-received Pd-packing samples showed the presence of PdO, but after a brief Ar ion sputter of the surface only metallic Pd was observed. This would suggest that the PdO layer is very thin and likely the result of surface contamination during the handling of the sample. Further, no palladium oxide was detected by the XRD analysis. More relevant are the results of the SEM study. Figure 39 depicts the surface of the fresh palladium pellets and the same pellets after reaction. There is a noticeable roughening of the surface. This roughening is related to the formation of a porous-like structure in the surface of the pellets as observed in the cross-sectional view (Figure 40). Change in the morphology of supported[82] and unsupported[83] palladium films after treatment of the samples in $O_2$-rich environments at elevated temperatures has been reported. Monteiro and coworkers[83] reported an increase in the rate (one order of magnitude) of methane oxidation on Pd-foils after the sample was treated in a $CH_4$-$O_2$ environment (excess methane) at 598 K for less than 3 hr. However, the foils tended to deactivate with time on stream but recovered the original high activity upon repeating the activation treatment. The deactivation was traced to the lost of PdO surface area due to the presence of the water produced in the reaction. Our results, on the contrary, suggest a continuous increase in the activity without any indication of deactivation with time on stream (test were conducted for periods of 6 hr or 24

hr before $O_2$/Ar treatment). As a consequence, the alteration of the surface appears to be stable. A possible explanation of the increase in activity is the observation by Matolin and coworkers[84] that CO interaction with Pd surfaces is enhanced by the presence of defects on the surface. Additionally, the WGSR has been reported to be structure-sensitive. It is not possible, however, to provide a definite explanation at this point. Further, such roughening may seriously affect the integrity of ultra-thin membranes (1-5 microns in thickness.)

### 4.4.2 The Water-Gas Shift Reaction in the Presence of Palladium-Copper packing

The WGSR was also conducted on Pd-Cu alloys. Previous work at NETL has shown that the 80 wt % Pd – 20 wt % Cu alloy displays sulfur tolerance over a wide range of temperature[18], as well as hydrogen permeation approaching pure palladium[20]. Therefore, this alloy could be a potential candidate for membrane reactors under harsh environments[85]. Although the early stage of development of these membranes prevents their application in an actual membrane reactor, a study of the effect of the membrane material on the reaction is pertinent to the long-term development of robust membrane reactors.

The 80 wt % Pd-Cu-packing test was carried out under similar conditions as the Pd-packing test, e.g., surface area, packing shape, inlet concentrations. However, the test was restricted to ambient pressure in order to study the behavior of the alloy at the low residence times likely to be encountered in a practical application of a membrane reactor. Figure 41 displays the conversions in the quartz reactor packed with Pd-Cu. The fresh packing, i.e. without any pretreatment (data set 1), appears to be more active than its Pd counterpart. Moreover, the

fresh packing displayed a slight but clear trend of increasing conversion with time on stream. Several hours elapsed before the steady-state conversions reported on Figure 41 were attained.

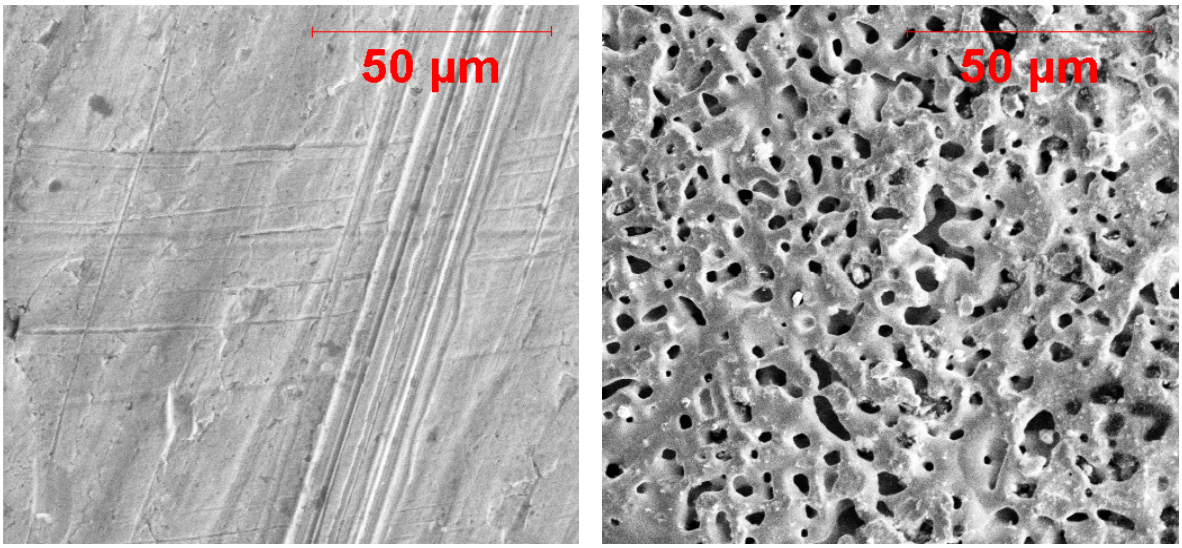


Figure 39. SEM images of the fresh (left) and used (i.e., after reaction studies) Pd packing.

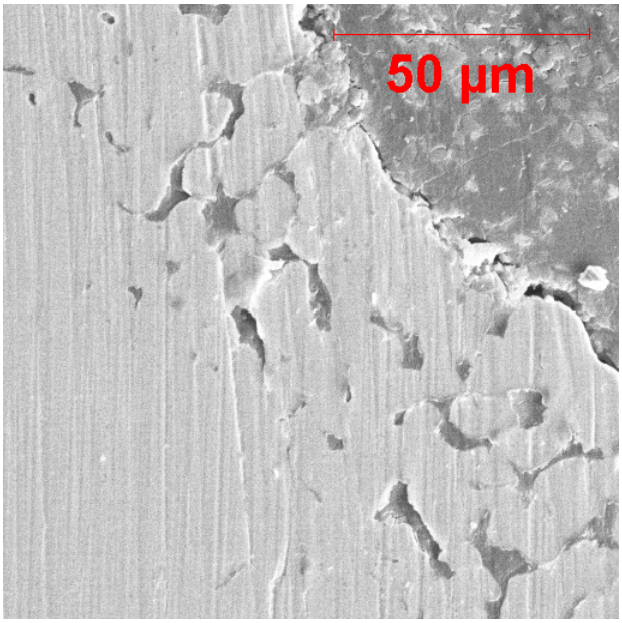


Figure 40. SEM cross-sectional view of the Pd-packing after reaction. The packing was encased in a polymer resin and polished.

Similar to the observations with the Pd-packed reactor, there is a noticeable increase in the activity of the Pd-Cu pellets after the packing was treated with oxygen (data sets 2 and 3). Attempts to reverse the effect of the oxidizing environment by means of an extended reducing treatment ($H_2$/Ar in a dry environment for over 60 hours) did not induce any change in the activity of the packing (data set 4. Finally, continuous operation in the CO/$H_2O$ environment (data sets 4, 5, and 6) did not effect conversions. Although CO conversions obtained in the early stages of testing of the Pd-Cu packing are larger than the conversions in the Pd-packed reactor under similar conditions of time on stream and oxidizing/reducing cycling (i.e. data sets 1 and 2 in Figure 41 and Figure 37, respectively), the difference in conversions in both reactors tended to level-off at longer time on stream.

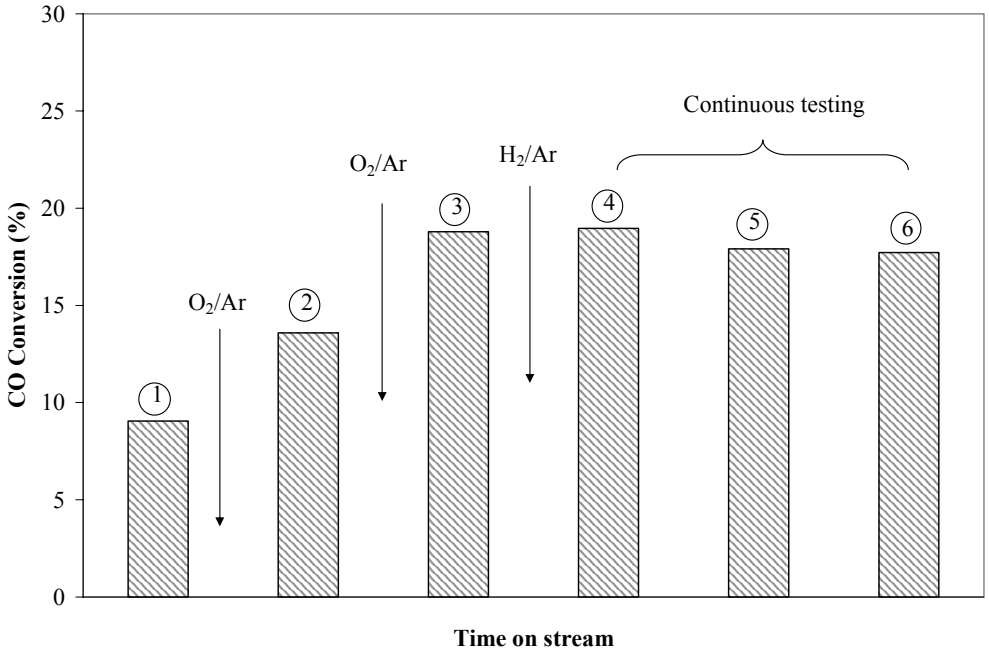


Figure 41. CO conversions for the WGSR in a Pd-Cu-packed, quartz reactor. T, 1123 K. P, 0.1 MPa. $\tau$, 0.25 s. $y_{CO,0}$ ~ 0.75, $y_{H2O,0}$ ~ 0.25. Gas-phase conversions are below 0.3%. CO equilibrium conversion is 35%.

The increase in the activity of the Pd packing was correlated to the change in surface area and morphology of the pellets. The Pd-Cu packing was removed to determine whether such surface changes were evident in the Pd-Cu pellets. Contrary to what was observed with the Pd pellets, where the packing was loose inside the reactor, the Pd-Cu pellets fused together forming a single structure bearing resemblance to a porous media (Figure 42a). Moreover, numerous cracks were found on the surface and internal porosity was noted in the pellets (Figure 42b). Clearly, this macroscopic/microscopic channel network would provide a more favorable environment for a heterogeneous reaction than that offered by the randomly packed solid palladium cylinders. Consequently, a direct comparison between the conversions in both systems is not possible. An attempt to prevent the formation of the macroscopic structure shown in Figure 42a was carried out. Small slabs (10 mm long, 2 mm wide, 1 mm thick) were cut from an 80 wt % Pd-Cu alloy foil and twisted to form small spirals providing a less densely-packed arrangement that would minimize the contact points while having the same exposed geometric surface area. Conversions larger than the gas-phase conversion (e.g. 2.79% versus 0.34%) were attained. However, mass transfer limitations indicated by the relative invariance of conversions with residence time at low flow rates, were significant and could not be circumvented. Moreover, it was found that the spirals fused together into a compact bundle. The tendency of the Pd-Cu packing to fuse together at the high temperature conditions of this work can be traced to the melting point of the alloy. The 80 wt % Pd-Cu alloy has a significantly lower melting point than the pure palladium[86], 1593 K and 1823 K, respectively. Consequently, the larger atomic mobility in the alloy would facilitate adhesion of the pellets.

Characterization of the Pd-Cu pellets was performed by XRD and SEM-EDS. For XRD analysis, one of the pellets was separated from the large agglomerate and pressed into a thin foil that was placed on a quartz plate. The x-ray pattern suggests that the both the bulk and surface of the pellet have the same composition, i.e. 80 wt% Pd 20 wt% Cu. A similar conclusion was reached when comparing the bulk and surface composition by SEM-EDS. However, the SEM analysis revealed an increase in the surface area (Figure 43). The fact that the surface roughening is not as severe as the observed in the Pd pellets is probably due to the lower total time on stream of the Pd-Cu pellets. The roughening of the surface should be considered in the application of a Pd-Cu membrane reactor where oxygen is employed to remove carbon deposits.

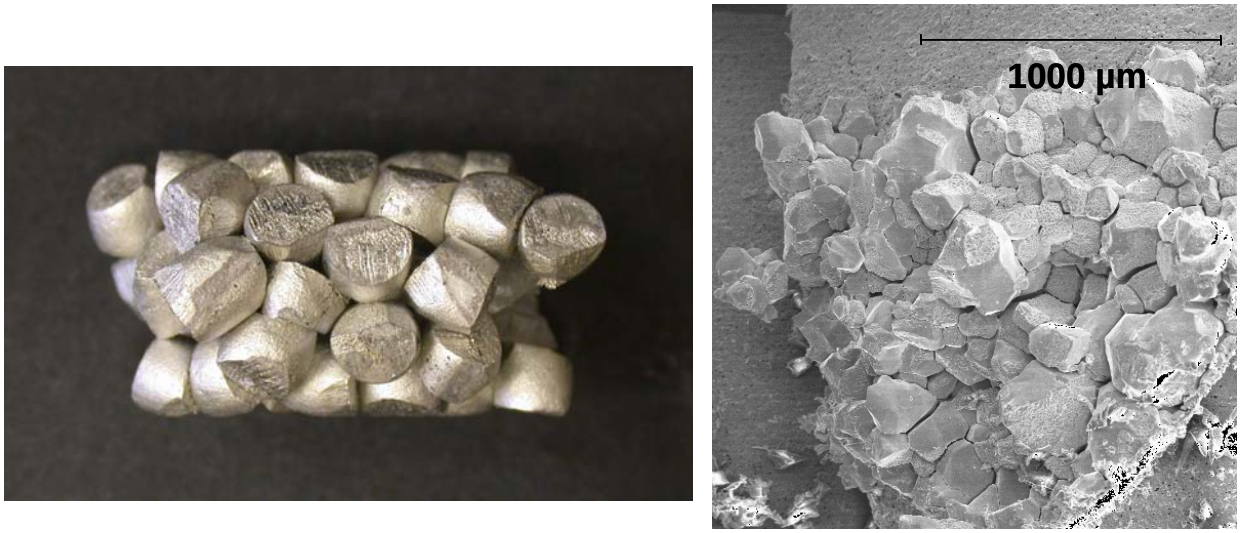


Figure 42. Pd-Cu packing after reaction. (a) Photograph of the packing, (b) SEM picture of the internal structure of a fractured pellet.

Although our experimental results are not suitable for a direct comparison between the WGSR in the presence of Pd and Pd-Cu due to the differences in the gas-solid interactions in the two systems (e.g., total surface area accessible to the gas stream), the larger CO conversion observed with the fresh Pd-Cu catalyst suggests that this material is a better catalyst for the

reaction. The addition of palladium to copper-supported catalysts has been shown to have an enhancing effect on the WGSR at low temperature[87]. The promoting effect of the Pd-Cu pair has also been observed in the elimination of CO and NO on ceria-zirconia-alumina-based catalysts[88]. This effect was partly explained by the formation of a Pd-Cu alloy with low Cu content. Previous theoretical work had suggested a change in the electronic configuration of Pd due to the interaction with Cu[89]. Additionally, studies of the WGSR on single-crystal Cu surfaces have suggested that the high-temperature reaction would follow a surface-redox mechanism described by dissociative adsorption of H2O that would provide the O species that further react with CO[90,91]. The dissociation of H2O, the rate-limiting-step, is favored in less densely packed surface configurations[90,92], e.g. Cu(100) vs Cu(111). Therefore, it is tempting to speculate that the superior performance of the Pd-Cu alloy is due to role played by low content of copper on the surface in the initiation of the reaction.

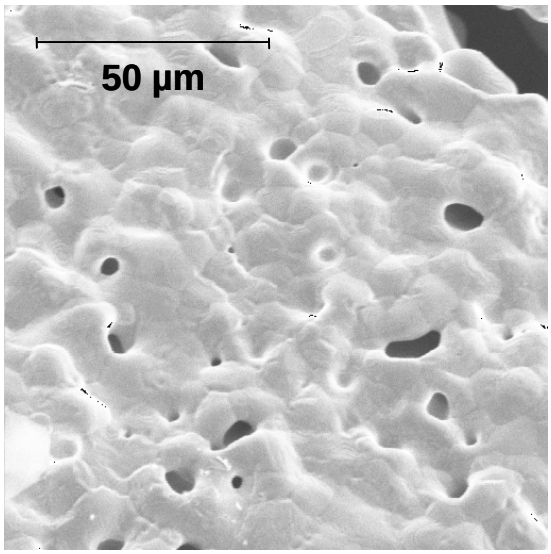


Figure 43. SEM image of the surface of a Pd-Cu pellet after reaction.

# 5.0 THE HIGH-TEMPERATURE, HIGH-PRESSURE WGSR IN A Pd-BASED MEMBRANE REACTOR

## 5.1 EFFECT OF CO AND $H_2O$ ON THE PERMEATION OF HYDROGEN THROUGH PALLADIUM MEMBRANES

CO is a known poison for palladium catalysts. Moreover, a detrimental effect of CO on the permeation of hydrogen through palladium membranes has been reported in literature[28,29]. $H_2O$ has also been found to impact the flux of hydrogen through palladium membranes[28]. However, these studies have been conducted at relatively low temperatures. Further, those reports addressed the effect of relatively small amounts of contaminants on a concentrated hydrogen stream. Similar experiments were conducted in this study under the conditions of high temperature and high concentrations of each contaminant likely to be found in the post-gasifier stream. Specifically, the effect of CO and $H_2O$ was determined by comparing the membrane permeance of 25% $H_2$ / 30% CO / balance He or 20% $H_2$ / 15% $H_2O$ / balance He gas mixtures with that of a 20% $H_2$ / balance He gas mixture. An attempt was made to determine the effect of $CO_2$ as well. However, due to the large conversions of the reverse WGSR in Inconel®600 reactors, the results do not allow for the independent determination of the effect of this component. These investigations were carried out with a pure palladium disk, 1-mm thick, at 1173 K and 1.6 MPa; the membrane was welded to Inconel®600 extension tubes as indicated in

Figure 7. Hydrogen permeance through the membrane, as defined by equation (5-1) –derived from Equation (3-8)–, was chosen as the criterion to determine the influence of the CO and $H_2O$ on the hydrogen flux through the membrane because it accounts for the differences in partial pressure of $H_2$ between the $H_2$/He and $H_2$/CO/He (or $H_2$/$H_2O$/He) experiments.

$$K = \frac{J_{H2}}{(P_{H2,retentate}^{0.5} - P_{H2,permeate}^{0.5})} \qquad (5\text{-}1)$$

where $K$ has units of (mol $H_2$) $m^{-2}$ $s^{-1}$ $Pa^{-0.5}$

Equation (5-1) assumes that the hydrogen flux is controlled by the diffusion of hydrogen through the membrane, i.e. the partial pressure exponent is 0.5. However, mass transfer limitations are known to arise at low concentrations of hydrogen[93]. Moreover, the low Reynolds number and linear velocity present in our experimental set-up (~20 and 0.2 cm/s, respectively) favor the formation of a boundary layer affecting the hydrogen flux from the bulk of the gas phase to the surface of the membrane. This mass transfer resistance may cause the partial pressure exponent to deviate from 0.5[57] resulting in misinterpretation of the experimental results[93]. Therefore, the partial pressure exponent was determined from 30% $H_2$/He gas mixtures. The results (not shown) can be described very well with an exponent value of 0.5. Additionally, the permeance value was in very good agreement with previous studies at NETL with 90 % $H_2$/He mixtures[56]. These results indicate that mass-transfer limitations do not play a significant role in the permeation experiments under the conditions of this study.

Figure 44 displays the effect of CO on the permeance of hydrogen through the palladium membrane. A significant decrease in the hydrogen permeance is observed once CO is fed to the

system. However, after the steep initial decline the permeance increases, eventually achieving the original value. This suggests a physical rather than a chemical effect. In fact, the sudden evolution of methane and carbon dioxide on the retentate side of the Pd membrane (see Figure 44) indicates that the decrease in hydrogen permeance is due to the formation of carbon in the system. Carbon is formed by the Boudouard reaction which is significant in the preheating section. The permeance of hydrogen is fully restored when CO is turned off.

The effect of $H_2O$ on the permeation of hydrogen through palladium membranes at high-temperature and pressure was also assessed. The $H_2O$ concentration was 15.1 ± 4.1%. The variance was due to the difficulties of vaporizing a constant amount of liquid water into the $H_2$/He feed stream. Figure 45 shows that the effect of steam on the permeance is negligible at the temperature studied. The scatter of the results is attributed to the dosing of water.

## 5.2 THE HIGH-TEMPERATURE, HIGH-PRESSURE WGSR IN A Pd/Inconel®600 - MEMBRANE REACTOR

Ma and Lund modeled the high-temperature (<773 K) WGSR in a Pd membrane reactor packed with a commercial iron-chromium catalyst[9]. They found that the performance of the reactor was governed by the reaction rate. The effect of an improved, $CO_2$-tolerant catalyst in enhancing the production of hydrogen is much greater than that of a perfect membrane. In fact, for a 90% $H_2$ yield the use of a perfect catalyst could accomplish a 76% reduction in the reactor volume whereas the use of a perfect membrane (i.e., one that would extract all hydrogen present in the reactor side, yielding $P_{H2} = 0$ throughout the reactor) would reduce the reactor size by 12%.

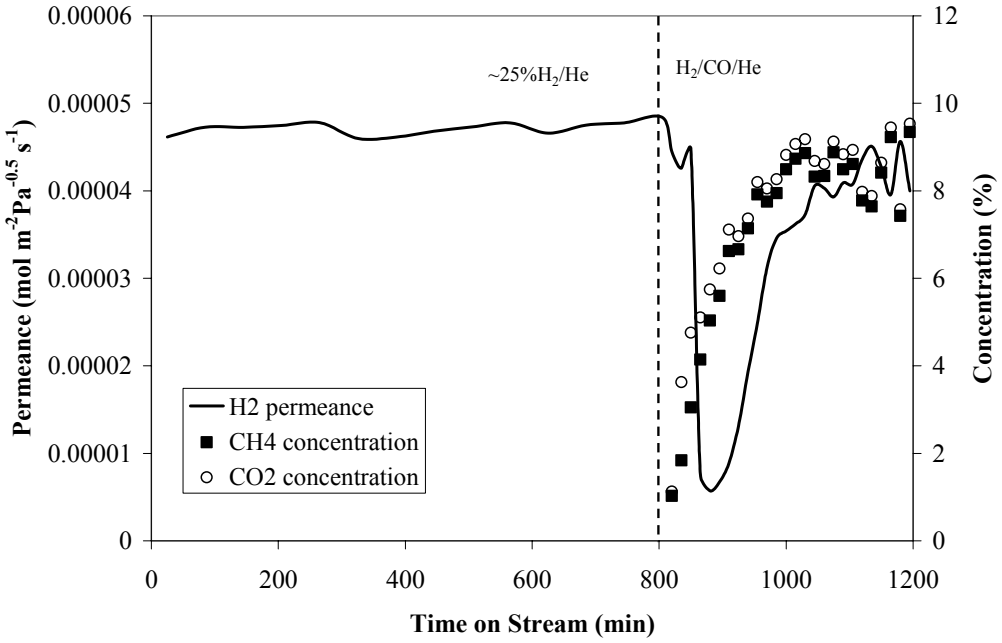


Figure 44. Effect of CO on the hydrogen permeation through a 1-mm thick Pd membrane. T, 1173 K. Permeate pressure (total), 1.6 MPa. Retentate pressure (total), 0.1 MPa.

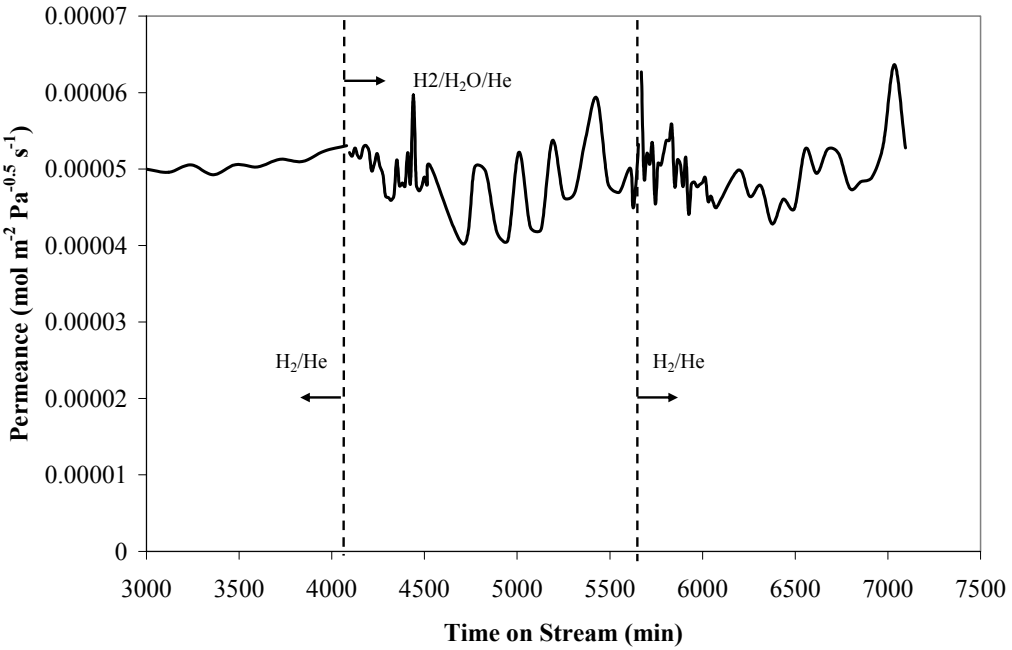


Figure 45. Effect of $H_2O$ on hydrogen permeation through a 1-mm thick Pd membrane. T = 1173 K; permeate pressure (total), 1.6 MPa; retentate pressure (total), 1.0 MPa.

Although the extremely large driving force (6.9 MPa in the reactor side and 0.1 MPa in the sweep) and very-thin membrane (10 μm) assumed in the model could lead to underestimate the importance of the membrane, the results suggest that the WGSR could be kinetic-limited under the high temperature conditions explored in this project, especially in the absence of heterogeneous catalyst particles. Therefore, given the relatively slow kinetics of the gas-phase WGSR, simulations were performed to gain insight on the performance of the membrane reactor as a function of the reaction and permeation rates. The simple reactor model described in Section 3.2.4 was used to estimate the conversions in a lab-scale Pd-membrane reactor. The reactor diameter was set to 3.175 mm OD and the membrane thickness to 100 μm. The gas-phase rate expression derived from the Bradford mechanism was modified to account for the slowing down of the reaction at large conversions (see section 3.2.2). The permeance value for the thin Pd membrane was extracted from experimental work previously conducted at NETL. Figure 46 summarizes the results. Two cases were considered. The effect of the rate of reaction (e.g., rate constant) in a membrane reactor with fixed hydrogen permeance was modeled first. The change in the reaction rate was realized by changing the value of the rate constant while keeping the inlet concentration constant. At the conditions of the figure, the inhibiting effect of the opposing reaction should be small at conversions less than ~30% (see section 3.2.2). Therefore, there is no gain in hydrogen yield at conversions lower than that value (e.g., gas-phase kinetics - base case). Moreover, it is clear from the figure that such a threshold should be surpassed as early as possible in the reactor if the membrane is to be effective. In other words, a large reaction rate is critical to the performance of the membrane reactor, otherwise a very big reactor should be used to ensure large conversions (as a result of the larger residence times) adversely impacting the economics due to the large membrane surface area. The second case

studied was that of the effect of permeation rate on the conversions at constant reaction rate, i.e. the same value of rate constant and inlet reactant concentration. It was found that increasing the permeance of the membrane by a factor of 100, which translates into lower concentration of hydrogen in the reaction side, causes virtually no alteration to the conversion profile regardless of the rate constant value used in the simulation (see figure). This observation indicates that a thin (100 μm) Pd-membrane is capable of efficient removal of the $H_2$ produced in the reaction and stresses the predominance of the reaction rate on the membrane reactor performance.

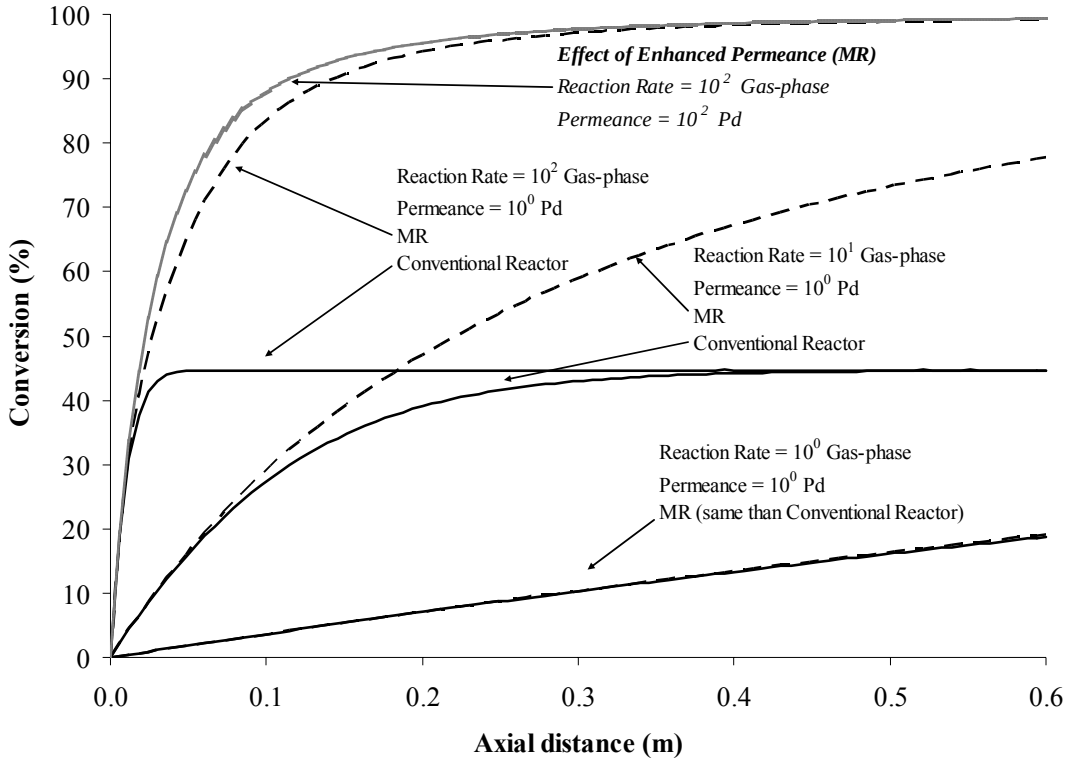


Figure 46. Modeling of a tubular Pd-based membrane reactor - Effect of the reaction rate (constant membrane permeance) and membrane permeance (indicated for the highest reaction rate). Change in reaction rate and permeance is given as orders of magnitude of gas-phase rate constant and Pd-permeance, respectively. $F_{CO,0} = F_{H2O,0} = 50$ sccm, $F_{CO2,0} = F_{H2,0} = 0$. T = 1173 K; P = 1.6 MPa. Reactor diameter, 3.175 mm. Concentration of $H_2$ in the sweep side was assumed to be very low. Conversions in the non-membrane reactor (dashed lines) are included as comparison.

A membrane reactor combining fast-kinetics and low permeation rate (e.g., small membrane area) was built to assess whether such arrangement would suffice to significantly enhance the reactant conversions. Clearly, a design where the amount of the expensive membrane material is minimized would provide the best economic scenario for the deployment of membrane reactors. Consequently, the WGSR was conducted in the same configuration used for the permeance studies, namely a palladium disk was welded to the top of the Inconel®600 tube, as depicted in Figure 6 and Figure 7. In view of the very-large conversions attained, as well as the side-reactions present when the WGSR is carried out in the Inconel®600 reactor, it was not possible to determine the conversions using the rate constant derived for the gas-phase reaction. Therefore, a blank reactor was also constructed to determine the conversions due to the reactor walls. Comparison of the conversions in both reactors would give a clear estimation of the efficacy of the membrane reactor in enhancing the hydrogen yield. The design of the blank reactor was similar to the membrane reactor with the exception that the palladium membrane was backed by a very low permeability material. This design would account for the presence of palladium surfaces (and their catalytic effect) without the loss of hydrogen due to permeation.

The test was also intended to explore the possible complications that could arise in the industrial application of a membrane reactor (e.g., carbon deposition on the membrane), where the gases will most probably encounter metallic surfaces in addition to the membrane itself. Additionally, the extent of the surface alteration of the Pd membrane as a result of the oxidizing treatment used to remove possible carbon deposits and its impact on the long-term performance of the membrane was studied. The use of a thick membrane (1 mm) was preferred to gain mechanical strength and ascertain the behavior of the membrane reactor under low-flux

conditions. Only CO and $H_2O$ were fed to the system; any $CO_2$ and $H_2$ present at the outlet of the reactor would be produced primarily via the WGSR.

The membrane and blank reactors were tested under equivalent experimental conditions (residence time, $CO/H_2O$ ratio, temperature, total pressure), Table 9. Three different pressures in the reaction side were used in the tests. The pressure in the sweep side was 10 - 100 psig lower than that in the reaction side. Each entry in the table compares the CO and $H_2O$ conversions for the same reaction conditions, insofar as possible, in the membrane and blank reactors. Several observations can be drawn from the data. Firstly, both the membrane and blank reactors display a trend of increasing conversion with residence time. This trend could be misleading, however, if not viewed in context. At higher pressures both larger residence times and inlet concentrations are realized. On the other hand, the different $CO/H_2O$ inlet ratios make it difficult to compare the conversions directly. However, the operation of the blank reactor under constant $CO/H_2O$ ratio at two different pressures (first and third entries in Table 9) indicates that equilibrium conversions are not attained at very low residence times, i.e. 0.12 s. Secondly, regardless of the $CO/H_2O$ inlet reactant ratio, CO conversions are significantly larger than the $H_2O$ conversions in both reactor configurations for all conditions studied. This can be attributed to the Boudouard reaction taking place in the preheating section of both systems. Therefore, the performance of the reactor should be judged by the conversion of $H_2O$ rather than by the conversion of CO. In fact, the side-reactions involving CO make it impossible to determine the expected equilibrium conversion in the system because the concentration of CO at the inlet of the *reaction zone* cannot be ascertained.

Table 9. Performance of a Pd-Inconel Membrane Reactor compared with the Inconel Blank Reactor. All experiments were carried out at 1173 K.

| | Membrane Reactor | | | | Blank Reactor | | | |
|---|---|---|---|---|---|---|---|---|
| Pressure (total) | τ (s) | $CO/H_2O$ (inlet) | Conversion (%) CO | Conversion (%) $H_2O$ | τ (s) | $CO/H_2O$ (inlet) | Conversion (%) CO | Conversion (%) $H_2O$ |
| 0.1 MPa | 0.10 | 0.5 | 52.6 | 26.3 | 0.12 | 0.6 | 63.7 | 30.8 |
| 0.1 MPa | 0.29 | 0.9 | 64.4 | 33.4 | 0.27 | 1.3 | 64.1 | 34.5 |
| 0.6 MPa | 1.13 | 1.4 | 81.9 | 50.9 | 0.93 | 0.7 | 69.3 | 39.7 |
| 1.6 MPa | 2.45 | 5.7 | 77.7 | 66.3 | 2.50 | 5.7 | 77.2 | 55.8 |

A noticeable increase in the $H_2O$ conversion is observed when the membrane reactor is operated at elevated pressure. For instance, the conversion in the membrane reactor at 1.6 MPa (66 %) is larger than the conversion attained in the blank reactor (56 %); the similar observation holds when the reactors are operated at 0.6 MPa. Consequently, the use of a membrane reactor allows for enhanced hydrogen production. It is expected that the performance of the membrane reactor will be better at higher total pressure as a result of the higher driving force for hydrogen permeation through the membrane. However, due to the change in residence time, $CO/H_2O$ ratio, and inlet concentrations with total pressure of the system (e.g., low $CO/H_2O$ ratios can only be realized at low total pressure), it is not possible to establish a direct comparison of the reactor performance at different pressures. Therefore, the introduction of the 'hydrogen recovery factor', HRF, defined as the fraction of hydrogen produced in the reaction that has been extracted by the membrane, Equation (5-2), would permit an objective comparison of the reactor performance under different operating conditions. At higher pressure the HRF is larger, e.g. 0.24 at 1.6 MPa versus 0.12 at 0.6 MPa. However, the amount of $CH_4$ in the reactor effluent at high-pressure is significantly larger, e.g. ~4% at 1.6 MPa compared with <1% at 0.1 MPa. Experiments with the Inconel®600 reactor suggested that the methane is formed by the reaction

of carbon and hydrogen. As part of the hydrogen formed in the reaction would be consumed by this side reaction adversely affecting the $H_2$ recovery in the membrane reactor, it is useful to explore conditions that would minimize the deposition of carbon in the reactor and/or on the membrane (e.g., $CO/H_2O$ ratio, residence time).

$$HRF = \frac{F_{H2,sweep}}{F_{H2,sweep} + F_{H2,retentate}} \tag{5-2}$$

The extent of the deposition of carbon via the Boudouard reaction is proportional to the concentration of CO. Moreover, a common practice in industry is to operate at low $CO/H_2O$ ratios to prevent coking of the WGS catalysts. Therefore, the effect of $CO/H_2O$ ratio on the performance of the membrane reactor under constant residence time was addressed. Due to the limitation imposed by the maximum temperature of the feed and effluent lines of the reactor, only relatively low concentrations of $H_2O$ (less than 30%) could be realized at high pressure. Consequently, large variations in the $CO/H_2O$ ratio can only be accomplished at ambient pressure, the span possible at high pressure being much more limited. A side effect of the variation of the $CO/H_2O$ ratio at constant residence time is the change in the amount of $H_2$ produced in the reaction. However, small differences in the concentration of hydrogen in the retentate side should not greatly influence the driving force for permeation. As a result, the performance of the reactor can be evaluated from the HRF. Results are summarized in Table 10. A decrease in the $CO/H_2O$ ratio increases the HRF. Further, under similar HRF values (first and second entries in Table 10), the lower $CO_2/H_2$ ratio at the outlet of the reactor suggests an inhibition of the conversion of CO into carbon and $CO_2$ at low $CO/H_2O$ ratios. It appears that a low $CO/H_2O$ ratio is not enough to prevent the phenomenon completely, however.

Table 10. Effect of the $CO/H_2O$ ratio in the performance on the membrane reactor.

| Pressure | $CO/H_2O$, inlet | $\tau$, s | $CO_2/H_2$, outlet | HRF, % |
|---|---|---|---|---|
| Ambient | 0.60 | 0.29 | 1.28 | 8.95 |
| | 0.85 | 0.29 | 1.41 | 8.65 |
| | 3.24 | 0.28 | 2.08 | 6.46 |

Equilibrium conversions can be attained in Inconel®600 reactors at relatively low residence time (0.5 - 1 s). This suggests an approach to minimize the formation of carbon. Indeed, low residence times could reduce the extent of the Boudouard and/or other carbon-forming reactions. In fact, conversion of CO in the forward WGSR experiments in the Inconel®600 reactor appeared not to be significantly influenced by the Boudouard reaction as indicated by the fact that both the $H_2O$ and CO conversion corresponded to the equilibrium conversions of the WGSR. The lower extent of the Boudouard reaction in those experiments can be attributed to the much lower residence time in the preheating section realized in such reactor configuration. Moreover, low residence times will be required to achieve large throughputs of hydrogen during industrial operation. Therefore, the effect of residence time at constant $CO/H_2O$ ratios was studied in the Pd/Inconel membrane reactor. Table 11 shows that the lowest $CO_2/H_2$ ratio is achieved at the lowest residence time. However, the HRF is also the lowest at such residence time, i.e. less hydrogen is extracted from the reactor. Doubling the residence time (second and third entries) brings no significant change in the $CO_2/H_2$ ratio at the outlet of the reactor. This could indicate that the formation of carbon is somewhat reduced at low residence times. Indeed, a lower $CO_2/H_2$ ratio should be expected at larger HRF if the extent of the Boudouard reaction were similar. From the results presented it is clear, however, that large

residence times (or larger membrane surface area) are required to facilitate the permeation of hydrogen through the membrane.

Table 11. Effect of the $CO/H_2O$ ratio in the performance on the membrane reactor.

| Pressure | $CO/H_2O$, inlet | $\tau$, s | $CO_2/H_2$, outlet | HRF, % |
|---|---|---|---|---|
| 0.1 MPa | 0.54 | 0.10 | 1.14 | 2.17 |
| | 0.59 | 0.16 | 1.34 | 5.16 |
| | 0.60 | 0.29 | 1.28 | 8.95 |

The effect of the WGSR environment and the $O_2$ treatment on the palladium was ascertained by inspection of the surface and cross section of the membrane. The membrane was extracted, cross sectioned and polished for SEM analysis. Results are presented in Figure 47. The roughening of the surface is more significant than that observed with the palladium packing, perhaps as a result of the longer time on stream. The cross-sectional view of the membrane reveals that the membrane surface is being corroded. Although the damage is constrained to the surface and does not appear to compromise the integrity of the membrane, the long-term stability of a thin membrane (e.g., on the order of tens of microns thick) may be a concern when run under conditions where formation of carbon deposits must be minimized by oxidation treatment.

In summary, it has been shown that the hydrogen yield can be increased by the introduction of relatively small membranes provided that the reaction kinetics are fast. However, despite the economic attractiveness of this approach, several issues may impede its development. The extent of carbon deposition on the membrane resulting from side-reactions on the reactor walls hinders the amount of hydrogen that can be extracted from the reactor. Manipulation of

the reactor conditions (e.g., reactant ratio, residence time) appears to be insufficient to prevent the occurrence of these side-reactions or effectively control their extent. Further, the introduction of oxygen to remove the carbon deposits may ultimately create a porous structure that could penetrate thin membranes and cause loss of selectivity. Although other alternatives should be attempted to cope with these side effects (e.g., the use of lower $CO/H_2O$ ratios to minimize the formation of carbon deposits, or the use of $H_2O$ rather than $O_2$ to remove them), a system without these complications would be favored in an industrial setting. Consequently, a Pd membrane reactor with negligible contact with other metallic surfaces (e.g., Inconel®600) was tested. The drawback of this approach is the larger reactor size (and membrane surface area) required to compensate for the slow kinetics. This is the topic of the next section.

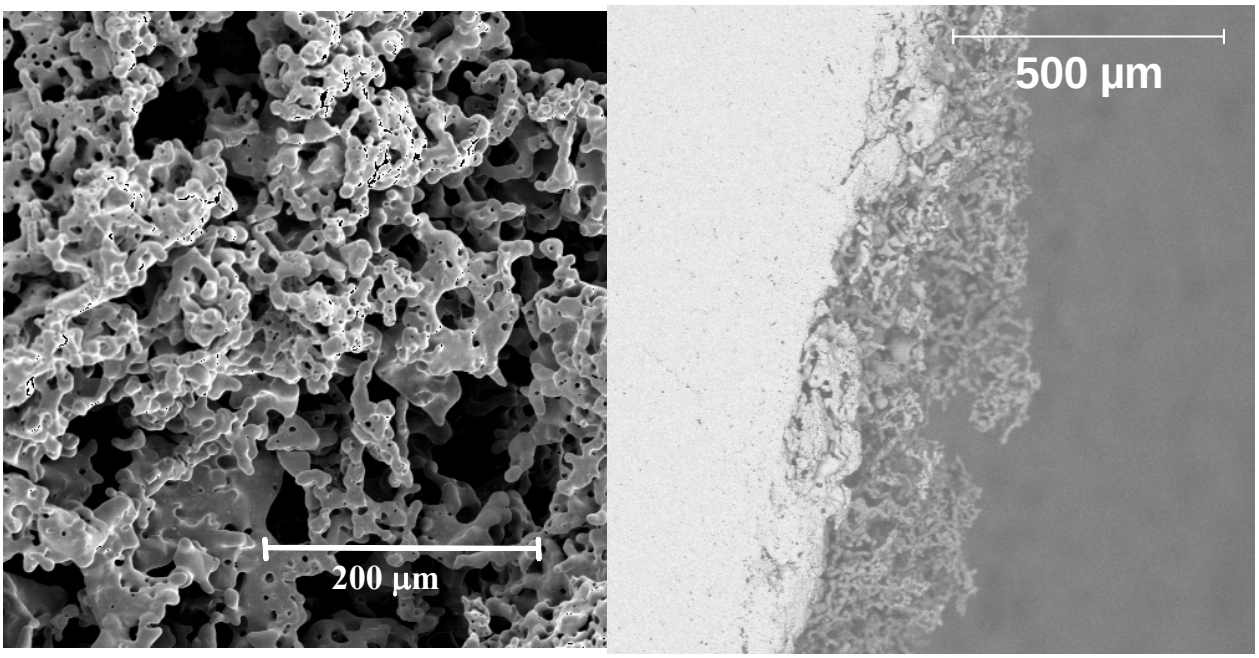


Figure 47. SEM image of the Pd membrane after the WGSR. (a) Surface, (b) Cross-sectional view (backscattered).

## 5.3 THE HIGH-TEMPERATURE, HIGH-PRESSURE WGSR IN A Pd-BASED MEMBRANE REACTOR

Previous experimental investigations of the WGSR in Pd-based membrane reactors have been conducted in reactors with thin supported membranes. This approach minimizes the amount of palladium required while ensuring a large permeation of hydrogen through the membrane. Moreover, a successful commercial application of a Pd-based membrane reactor will depend on the ability to fabricate such membranes and endow them with thermal and mechanical strength. Technologies for preparing thin, defect-free membranes of different geometries and on various supports have improved substantially. Several of these options were considered for this study. The use of a thin Pd film supported on a porous ceramic was discarded in this project due to the difficulties in obtaining a gas-tight seal between the ceramic component and the metallic stainless steel tubing. Even though the use of porous metallic tubes is an option to circumvent that problem, surface characterization of the Pd-disk used in Section 5.2 showed significant intermetallic diffusion between the palladium membrane and the porous Hastelloy support despite the presence of a diffusion barrier at the interface. Intermetallic diffusion may seriously impair the performance of thin membranes[12]. Therefore, a thin-wall (125 μm), unsupported, 3.175 mm OD, 60 cm length, pure palladium (>99.9%, Johnson Matthey) tube was selected as the membrane for the Pd-based membrane reactor tests. The tubing was coiled to a total length of 15 cm (corresponding to the length of the heating element within the oven in Figure 6) and placed inside a 3.175 cm ID Inconel®600 tube, as shown schematically in Figure 48. This configuration would maximize the reaction volume and membrane surface area within the heated region. Two thermocouples were used to monitor and control the reaction temperature. This

was essential due to the large temperature gradient present in the heated zone (see below). The sweep and reacting gases were fed in counter-current mode. Argon was chosen as the sweep gas and was flowed in the annular space while the reaction would take place inside the palladium tubing. A quartz support was built to prevent the direct contact of the palladium with the Inconel®600 walls which could lead to intermetallic diffusion, Figure 49. A small total pressure gradient across the thin, unsupported film was accomplished by controlling the pressure in the reaction and permeation sides.

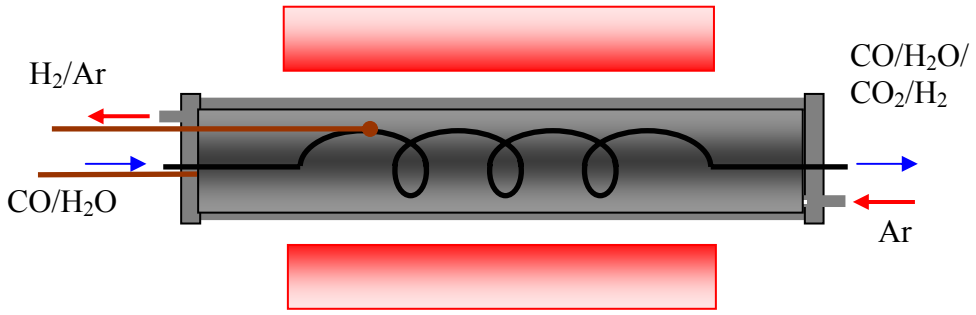


Figure 48. Schematic representation of the membrane reactor configuration. Not at scale. Total length of the heater is 15 cm.

Figure 49. Photograph of the palladium membrane reactor and quartz support. Outside diameter of the coil was less than 3.175 cm.

The presence of a temperature gradient inside the quartz reactor was detected while conducting the experiments on the kinetics of the gas-phase WGSR. The difference in temperature between the top and bottom of the reactor was small and could be attributed to the proximity of the inlet of the reactor to the edge of the heater (i.e., the temperature was found to fall sharply outside the heated zone). However, the reduced dimensions of that reactor (less than 1.5 cm long) as well as the smaller HMT unit used in the kinetic study suggest that the temperature profile may be significant over longer reactor length and oven size. Therefore, a simple experiment was conducted to determine the temperature profile over the length of the heating element of the HMT unit used in the membrane reactor experiments. An empty 2.54 cm OD Inconel®600 pipe was placed inside the heating element (i.e., Figure 48 with the coil absent). The heating element is contained within a purged vessel as described previously. A type-K thermocouple placed inside the tube and positioned approximately in the middle of the heated zone was used as input for the temperature controller. The thermocouple was not in contact with the walls of the tube. Once the temperature reached 1173 K, the power output of the heater was kept constant and the thermocouple was moved along the pipe axis under an Ar flow. Steady-state temperatures at each point were recorded. The effect of the direction of the argon flow and total flow rate on the temperature profile was also determined. The temperature profile was carried out for the length of the containment vessel (50 cm). Results are shown in Figure 50. The temperature gradient is skewed towards the pipe inlet perhaps as a result of uneven distribution of the insulation material inside the purged vessel (no significant effect of the direction and flow rate of argon on the temperature profile was found). Provided that the controlling thermocouple is placed in the same absolute position with respect to the heater, the temperature profile depicted in Figure 50 appears to be valid for the larger tube used during the

Pd-coil test, i.e. the temperature recorded at two separate points matches that of the temperature profile. If instead of being centered with respect to the heating element, i.e. the center of the reactor would be located in the '0' x-axis coordinate, the reactor is moved 2" towards the pipe inlet (to the left in Figure 50), the center of the reactor would coincide with the maximum temperature resulting in a symmetric profile, i.e. the temperatures at the reactor inlet and outlet are approximately the same. This approach, shown schematically in Figure 50, was used in all experiments in the series.

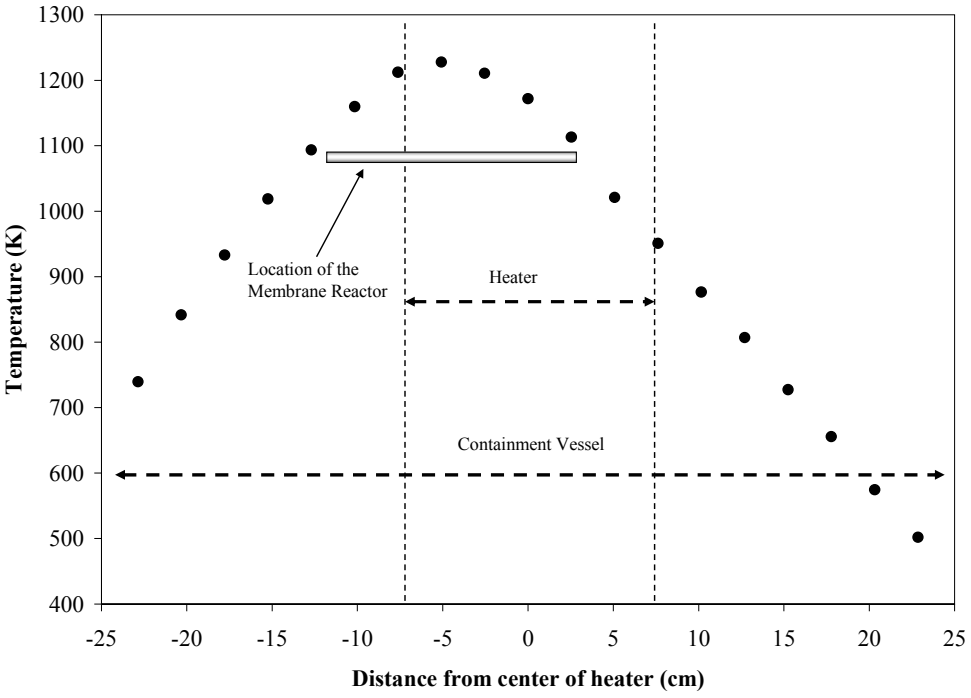


Figure 50. Temperature profile in the HMT unit utilized in the Pd-coil membrane reactor tests. Placement of the reactor (15 cm long) with respect to the heater is illustrated.

Clearly, the presence of the large temperature gradient makes it more difficult to interpret the results with the membrane reactor. Reaction rate and permeation will be higher in the center of

the reactor as opposed to the inlet and outlet sections. However, the use of a smaller reactor to achieve a more uniform temperature profile would adversely impact the residence time and the area available for permeation. Therefore, a non-permeable reactor of similar geometry and palladium surface area was built to serve as a base line for the Pd-membrane reactor test. The base line test was also used to validate a simple model of the influence of the temperature gradient and/or heat transfer effects on the reaction rate of the gas-phase WGSR. Specifically, the model was intended to give insight on the combined effect of the heat released by the reaction at high conversions and the external temperature gradient on the reaction kinetics; details are given in APPENDIX B. The base-line reactor consisted of a quartz coil of similar dimensions as the Pd-coil. A pressure equalization fluid, e.g. stagnant CO, was used to prevent a large pressure drop across the quartz tube wall. The presence of palladium was achieved by packing the quartz coil with small spirals (approximately 10 mm long, 3 mm diameter) made from palladium wire (diameter, 0.25 mm). This would ensure the same total exposed area of palladium with a minimum pressure drop while at the same time preventing the effect of hydrogen permeation. This blank test will be referred to as 'Pd-packed quartz coil' to distinguish it from the 'Pd-coil membrane reactor'. Placement of the reactor and reactant feed flow rates were similar in the blank and membrane reactors. However, it was not possible to match the temperature of the two tests. The temperature of the Pd-packed quartz coil was approximately 30 K lower. It was observed that the temperature profile changed proportionally, e.g. temperatures in Figure 50 shifted to lower temperatures by a factor of 30 K. Consequently, the results of the Pd-packed quartz coil were used to validate the reactor model under the same temperature profile.

Previous results with the Pd-packed quartz reactor, Section 4.4.1, suggested that fresh palladium, i.e. before being treated in the presence of $O_2$, displays negligible activity towards the WGSR. Therefore, conversions in the Pd-packed quartz coil reactor should be similar to the conversions predicted from the gas-phase reaction. Consequently, the reaction was modeled as taking place in a straight tubular reactor of the same diameter and reactor volume as the coil. The gas-phase kinetic correlation derived in section 3.2.2 was used to determine the conversions. The effect of the temperature rise on the reaction rate due to the exothermic character of the reaction was also considered. The reactor was contained in a larger circular tube where the temperature gradient was imposed on the wall. Heat transfer was assumed to occur primarily via natural convection, i.e. the pressure equalization fluid (CO) is stagnant. The reaction was modeled at conditions similar to the Pd-packed quartz coil experiments, namely, inlet flow rates of CO and $H_2O$, temperature gradient, pressure, and geometry. The conversion predicted from the model (20.64%) was significantly larger than the observed experimentally (~12%). The fact that the model does not capture the behavior of the system could possibly be attributed to the heat transfer effects occurring in the system. The estimated heat transfer coefficient inside the tube is very large (~180 W $m^2$ $K^{-1}$, as evaluated from correlations for forced convection in laminar flow) compared with the coefficient at the outside (~2.5 W $m^2$ $K^{-1}$, as evaluated from correlations for free convection in an annular space). Consequently, the overall heat transfer coefficient will be relatively small and the heat of reaction would not be efficiently dissipated. Further, the temperature rise would increase the rate constant explaining the larger conversions. However, this analysis does not take into account the large thermal mass provided by the quartz. In fact, the quartz walls can absorb the heat generated in the reaction without significant alteration of the surface temperature (e.g. the change in average temperature is less than 2 K).

Therefore, the reaction in the Pd-packed quartz coil would occur at a temperature close to the external temperature profile. Once this modification is introduced in the model, conversions predicted are in very good agreement with the experimental observations, 14.4% and 12%, respectively. Therefore, the non-isothermal model is adequate for determining the base line conversions in the non-membrane tubular reactor.

The heat transfer could play an important role in the Pd-coil membrane reactor, however, due to the much thinner wall and the lower heat capacity of the palladium. Moreover, the geometry of the reactor could influence the heat transfer. Coiled wires are commonly used to enhance the heat transfer from the walls to the bulk of a fluid inside straight circular tubes[94]. Further, heat transfer by natural convection outside helical coils occurs at faster rates than in straight tubes[95]. In addition, the heat transfer coefficient (forced convection in laminar regime) inside coiled tubes is larger than that obtained in straight tubes under certain circumstances, e.g. Prandtl and Dean numbers larger than 0.7 and 30, respectively[96]. However, very little experimental work has been performed in the heat transfer by forced convection outside coiled geometries. Dietrich and coworkers[97] suggested that straight wires perform better than coiled wires in the heat transfer by forced convection in a laminar regime. It is not clear, however, if their results (obtained for cross-flow) are applicable to the conditions of the present study. Nonetheless, it is possible that the correlations utilized in the model to calculate the heat transfer coefficient on the sweep side could lead to over-estimating its value. Therefore, additional simulations were conducted to determine the effect of the heat transfer coefficient on the expected conversions of the gas-phase WGSR in a tubular reactor.

The conditions used in the simulation were chosen to match the experiments conducted in the Pd-coil membrane reactor. The temperature profile outside the reactor was that indicated for the placement of the reactor in Figure 50, i.e. a parabolic temperature distribution with inlet and outlet temperature of 1100 K and maximum temperature of 1225 K. CO and $H_2O$ were fed to the reactor at an equal flow rate of 50 sccm giving a residence time of about 12 s (reactor dimensions, i.e. diameter and volume, were the same as in the experiments). The effect of the overall heat transfer coefficient, U, on the temperature inside the reactor and reactant conversion was determined. The heat transfer coefficient was varied from zero (adiabatic reactor) to infinity (reactor temperature equal to the temperature profile outside the reactor). Figure 51 depicts the temperature inside the reactor as a function of the heat transfer coefficient. With the exception of the adiabatic case (U = 0) where there is no heat exchange with the surroundings, all curves display a maximum in the temperature inside the reactor. Further, the location of the maxima moves to an earlier position in the reactor when the overall heat transfer coefficient is increased. At large values of U, the curve approaches the 'isothermal' case, i.e. the temperature inside the reactor is the same as the external temperature profile. The behavior illustrated in Figure 51 can be explained by the combined effect of the temperature profile and the heat released in the reaction. The temperature of the reaction mixture increases in the first part of the reactor due to the external temperature profile. As a consequence, the reaction rate constant and reaction rate increase. The larger rate translates into a further increase in the temperature inside the reactor and a further increase in the reaction rate. However, the elevation in temperature inside the reactor is accompanied by an increase in the heat loss to the surroundings. The trade-off between heat generation and heat loss ultimately leads to cooling down of the reacting mixture due to the slow down of the reaction stemming from the approach to equilibrium. Indeed, as

Figure 52 shows, the inflection point in the temperature curve can be correlated very well to the achievement of a quasi-plateau in conversion. Clearly, it can be expected that such a thermodynamic limitation (if present) would be less severe in the Pd-based membrane reactor used in this study. Finally, if the heat transfer coefficient is very large the heat released by the reaction will be readily exchanged to the surroundings without any gain in reaction rate and conversion. Although a quantitative extrapolation of the simulation of the non-membrane, reactor to the Pd-coil membrane reactor test is not possible, it is expected that the latter will follow a similar qualitative behavior.

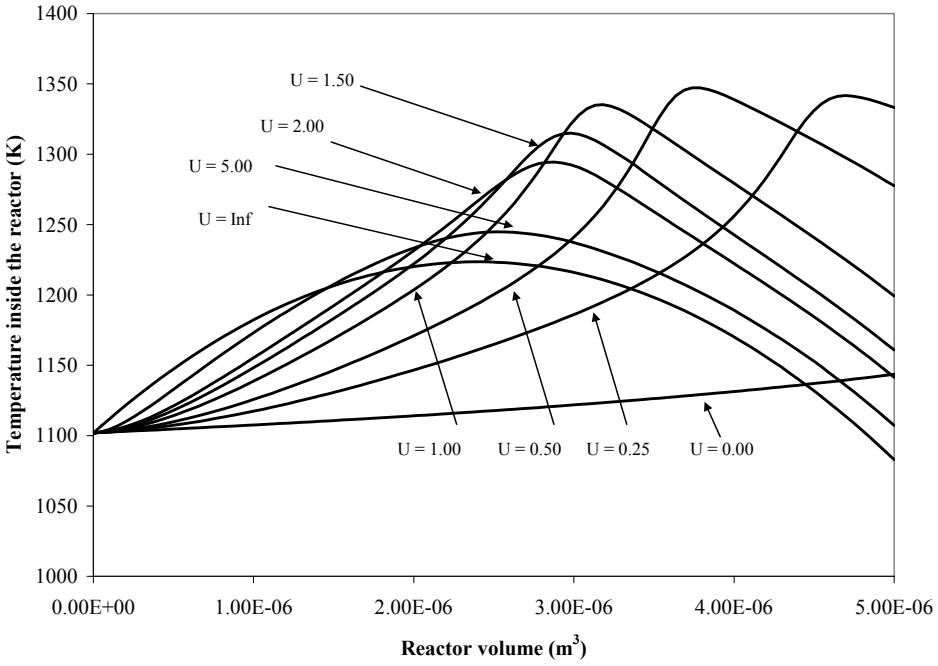


Figure 51. Modeling of the WGSR in a non-isothermal tubular reactor under the same conditions as the Pd-based membrane reactor - Effect of the overall heat transfer coefficient on the temperature inside the reactor.

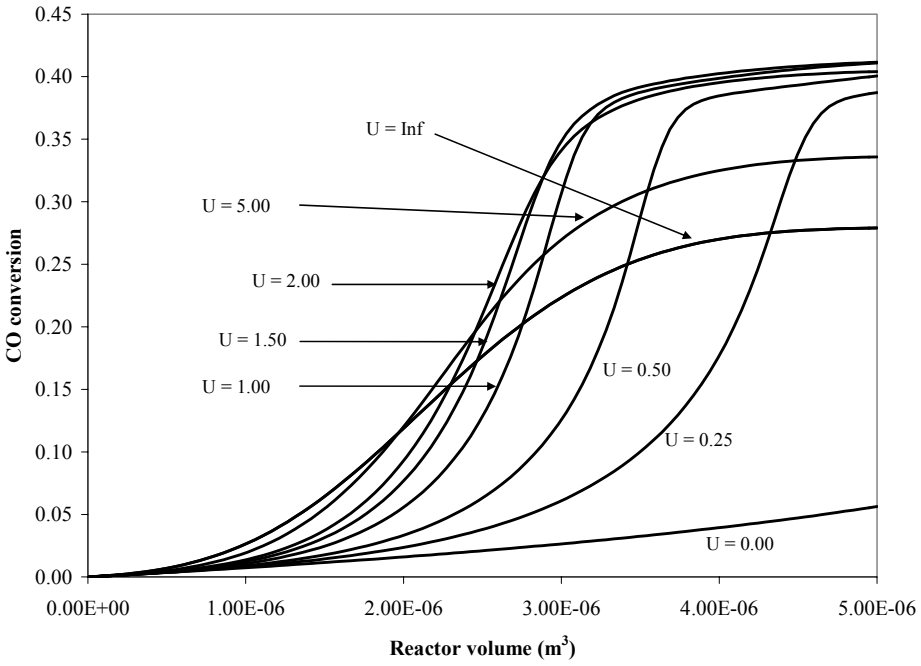


Figure 52. Modeling of the WGSR in a non-isothermal tubular reactor under the same conditions as the Pd-based membrane reactor - Effect of the overall heat transfer coefficient on conversions.

The Pd-coil membrane was evaluated by feeding a $H_2$-rich mixture (90% $H_2$/10% He) at 1.6 MPa. The pressure in the sweep side was kept at 1.5 MPa by flowing argon in counter-current mode. The membrane was heated up under helium until the temperature profile indicated in Figure 50 was attained as confirmed by the temperature difference in two thermocouples separated by approximately 5 cm. Determination of the hydrogen permeance of the membrane was attempted. The driving force for permeation was evaluated as the logarithm mean of the driving force at each end of the membrane. Results for the hydrogen permeance, 2.25E-05 mol $m^{-2}$ $s^{-1}$ $Pa^{-0.5}$, are one order of magnitude lower than expected for thin Pd membranes. This is likely due to the non uniform hydrogen flux through the membrane as hydrogen is being depleted from the feed side. Further, a modification of the membrane reactor model described in Section 3.2.4 to account for the temperature profile suggests that the recovery of hydrogen in the

sweep stream should be larger than that observed experimentally, e.g. 80+% of the hydrogen in the inlet stream was recovered in the permeate stream for a sweep flow rate of 200 sccm at a pressure of 1.6 MPa. This would suggest that mass transfer limitations on the sweep side cannot be neglected. However, such mass transfer limitations should be less important at higher sweep flow rates. The membrane was defect-free as indicated by the fact that only hydrogen permeated through it.

CO and $H_2O$ were then fed to the Pd-coil membrane reactor. The effect of sweep flow rate at constant residence time was determined, Figure 53. As expected, an increase in sweep rate induces an increase in conversion by allowing an increase in hydrogen extraction: the conversion increases from 35% to 38% when the sweep flow rate is increased from 200 to 400 sccm. These conversions can be compared with the value obtained from the tubular membrane reactor model under the assumption that the temperature inside the reactor is similar to the external temperature profile, i.e. an 'isothermal' membrane reactor, 32.3%. Further, the experimental conversions are just slightly higher than the conversion predicted in a non-membrane tubular reactor with the same temperature gradient inside the reactor, 27.9%. Therefore, it appears than only a modest enhancement in reactor performance is gained by the introduction of the Pd membrane. Moreover, conversions are still below the equilibrium limitation (equilibrium conversion ~50%). However, the impact of the sweep flow rate appears to be more significant at the highest flow rate tested. In fact, conversion is almost doubled when the sweep flow rate is increased from 400 to 500 sccm. Several experimental factors could cause this difference. Firstly, the tests with the high sweep rate, e.g. 500 sccm, were conducted after those at lower sweep flow rates. Experiments with the Pd-packed quartz coil reactor did not show an increase of conversion with

time on stream, though. Secondly, an intermediate treatment in $H_2$/He was performed between the experiments conducted at 400 and 500 sccm. Although the treatment of Pd pellets in the presence of hydrogen during the kinetic study of the fWGSR (Section 4.4.1) did not bring about any increase in the activity of the material, the differences in time scale and concentration between the two tests make it difficult to establish a clear correlation. Indeed, the concentration of the hydrogen stream was significantly higher in the Pd-coil test, e.g. 90% with respect to 1% in the quartz reactor packed with Pd-pellets. Unfortunately, the effect of such a large concentration of hydrogen on the conversion of the Pd-packed quartz coil reactor could not be determined because the reactor failed when performing the treatment in the $H_2$-rich stream. However, SEM analysis of the packing in the Pd-coil membrane reactor after testing did not reveal any surface alteration that could be linked to the increase in conversion. These arguments suggest, therefore, that the variation in conversion is due solely to the interaction of the sweep gas with the Pd membrane. Two additional observations give support to this interpretation. Firstly, in switching from low to high sweep flow rate an initial spike in conversion and hydrogen flow rate in the sweep side was observed. The spike was followed by a slow decline in both variables. On the contrary, at low sweep rate there is a slight trend of increasing hydrogen flow rate and conversion with time on stream. Secondly, an oscillatory behavior of the production of hydrogen was observed, this effect being more notable at the high sweep flow rate, Figure 54. Production of hydrogen increases noticeably over a short period of time and then decreases steadily until the next cycle where the maxima of the curves is displaced to higher values. This oscillatory behavior could not be studied over a longer period of time because the test was truncated by a leak developing in the reactor after sudden depressurization of the sweep side.

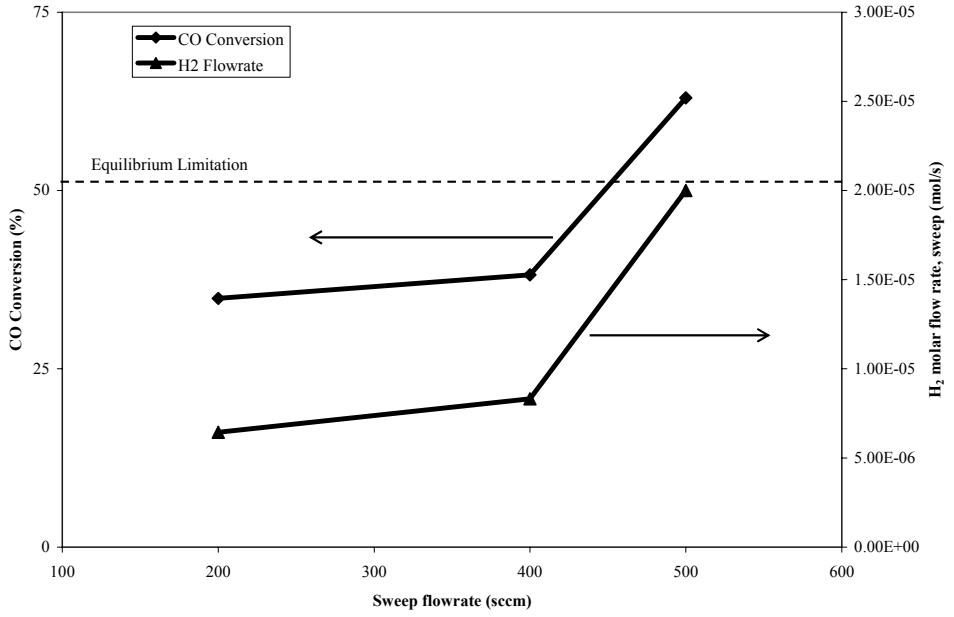


Figure 53. Performance of the Pd-coil quartz reactor in the production of hydrogen via the gas-phase WGSR. Equilibrium limitation is defined with respect to the outlet temperature.

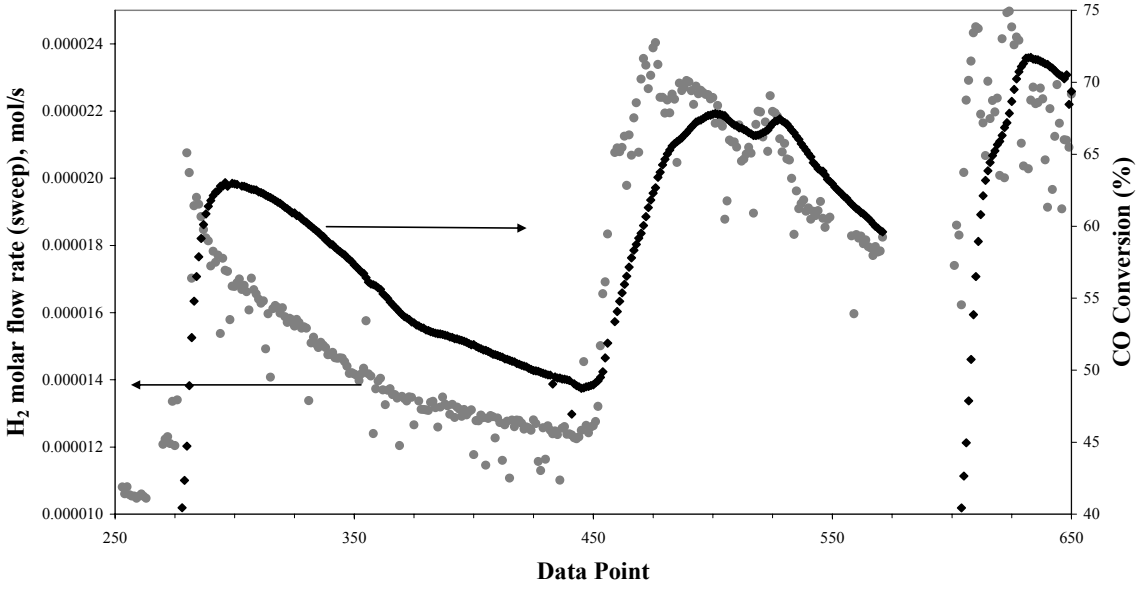


Figure 54. Dependence of the reaction conversion and hydrogen extraction with time on stream. There is a time lag between the curves due to the presence of the water trap. Samples taken at 15 or 30 minutes intervals. Sweep flow rate, 500 sccm. Residence time in reaction side, 13 s. Pressure, 1.6 MPa (reaction side), 1.5 MPa (sweep side). Equilibrium conversion is slightly above 50%. Expected conversion for a non-membrane reactor under the same external temperature profile is around 30%.

The simulations of heat transfer effects in the tubular reactor suggested that conversions are heavily dependent on the overall heat transfer coefficient, which in turn is determined by the heat transfer coefficient at the sweep side of the reactor. Further, the major resistance to heat transfer is given by the film adjacent to the gas-metal interface. The fact that at low conversions the results of the membrane reactor are similar to the predictions of the model when 'isothermal' conditions are assumed suggests that the $H_2$-rich boundary layer likely to be present at low sweep flow rates may be playing a significant role in the heat transfer. Indeed, the thermal conductivity of hydrogen is significantly larger than that of any other gas present, including that of argon. As a result, the heat transfer coefficient of a $H_2$-rich stream is several times larger than the value of the heat transfer coefficient of a $H_2$-depleted stream. Consequently, the heat released by the reaction would be readily transferred to the surroundings if the thermal boundary layer is $H_2$-rich. On the contrary, at high sweep rates the lower concentration of $H_2$ in the film would ensure a lower heat transfer coefficient, higher reaction temperature and, therefore, increased conversion. Further, the increase in the concentration of $H_2$ in the reaction side stemming from the aforementioned mechanism would increase its concentration in the sweep side of the membrane, augmenting the heat transfer coefficient leading to a slow cooling down of the reacting stream. Finally, the production rate of hydrogen would eventually fall to a level low enough to allow a more efficient sweep of the hydrogen present on the surface of the membrane, triggering a new cycle.

A comparison between the performance of the Pd-coil and Pd/Inconel membrane reactors can be established in terms of the hydrogen recovery factor. The HRF is significantly larger for the Pd-coil case, $0.89 \pm 0.04$, indicating that the reactor is kinetic-limited. In fact, the HRF was

approximately constant throughout the duration of the test, i.e. no correlation between the HRF and hydrogen production permeation rate was found. On the other hand, the much lower HRF obtained in the Pd/Inconel case suggests that the reactor is diffusion-limited. However, the membrane area and permeance are much lower with this configuration. In fact, membrane *permeability* is a function of the material and operating temperature only whereas membrane *permeance* depends on the thickness of the membrane. Therefore, if the HRF is assumed to be directly proportional to the surface area and inversely proportional to the membrane thickness it can be expected that the use of a thin Pd-foil, e.g. 100 μm, in the Pd/Inconel configuration could increase the HRF to values similar to those observed in the Pd-coil membrane reactor. Consequently, a large HRF would be attained with lower amounts of expensive palladium. However, the extent of side reactions and possible intermetallic diffusion between the thin membrane and its porous support need to be addressed.

# 6.0 SUMMARY AND OUTLOOK

## 6.1 SUMMARY

The intention of this work was to provide the fundamental background information required to determine whether the high-temperature, high-pressure water-gas shift reaction in a Pd-based membrane reactor has potential for the efficient production of hydrogen. The gas-phase reaction rate was obtained in an effort to assess if the reaction can proceed at rates high enough to preclude the need for an added catalyst. Further, the influence of construction and membrane materials on the extent of the reaction was determined. Next, the reaction was conducted in a Pd-based membrane reactor. Different configurations were studied and their advantages and disadvantages were discussed.

The rate of reaction of the homogeneous, reverse water-gas shift reaction was evaluated in an empty quartz reactor at elevated temperature (1148-1198 K), and low and high pressure conditions in the absence of a diluent gas. The low-pressure (0.1 MPa) results were consistent with the previously published, low-pressure rate expression of Graven and Long[49], but the resulting rates were roughly four times greater than reaction rates reported by Tingey[50] and by Kochubei and Moin[51]. CFD simulation results indicated that differences in reactor geometry were not responsible for these differences. Further, oxygen, which is known to catalyze the

reverse WGS reaction, was maintained at a concentration of less than 1 ppm in our reactor. The importance of an initial induction period in which the concentration of the chain carriers increases steadily with time was confirmed and the discrepancies between the different studies could be related to this effect. The simple gas-phase mechanism proposed by Bradford was found to satisfactorily describe the reaction. A pressure-equilibrated quartz reactor was also used to study the homogeneous rate of reaction for the first time under high-temperature, high-pressure conditions (up to 1.6 MPa). The rate constant, correlated by the low-pressure and high-pressure Arrhenius expressions were in good agreement over the 1148 – 1198 K temperature range, indicating that there was no significant effect of elevated pressure on the rate constant.

The rate of reaction of the homogeneous gas-phase forward water-gas shift reaction was studied at high-temperature (1070 – 1198 K) and both low (0.1 MPa) and high-pressure (1.6 MPa) conditions. The rate expression was consistent with the proposed gas-phase mechanism of the reaction. Further, the effect of the high-pressure conditions on the reaction rate was negligible. However, the pre-exponential factor and energy of activation predict rate constant values that are larger than those evaluated from the gas-phase mechanism and lower than those determined from the only available gas-phase, low-pressure correlation of Graven and Long[49]. Formation of carbon inside the reactor leading to a steady increase in the reaction rate was observed. However, the carbon deposits were minimized by flowing $O_2$ at high-temperature between the kinetic experiments. Therefore, the slightly larger rate constants of this study cannot be attributed to this effect. However, small deposits of carbon in the preheating section could not be removed with the oxygen treatment. Further, characterization of these deposits revealed the presence of trace amounts of nickel dispersed in the carbon. The carbon was probably formed by

the Boudouard reaction whereas the nickel was extracted from the stainless steel inlet tubing via the formation and decomposition of nickel carbonyl. The presence of the small amounts of nickel would account both for the absence of a kinetic induction period and the larger rate constant values.

Conversions attained in an Inconel®600 reactor were approximately two orders-of-magnitude greater than those attained in the quartz reactor for residence times of 0.1 – 0.5 seconds. Further, equilibrium conversions were attained at low-pressure conditions and temperatures as low as 973 K for the fWGSR at residence times lower than 1 s. This increase in conversion suggested that the Inconel®600 surfaces catalyzed the WGSR. Therefore, the use of intrinsic kinetic results based on quartz reactors in the design of a reverse WGS Inconel®600 reactor will lead to overestimates of the volume required to attain a specified level of conversion. Characterization of the reactor walls indicated the formation of a chromium oxide surface layer in the reaction zone. In addition, nickel extraction from the preheating section through metal dusting was observed. Production of methane was also found to occur in the Inconel®600 reactor.

The gas-phase reaction was enhanced by the presence of Pd or Pd-Cu packing. However, the catalytic effect was moderate when compared to Inconel®600, i.e. equilibrium conversions were not achieved when the reaction was conducted in the presence of Pd or Pd-Cu pellets with geometric surface area equal to the Inconel®600 reactor. The cycling between oxidizing and reducing environments significantly increased the conversions attained with the two materials. A likely explanation for the large conversions is the change in surface morphology (for Pd and

Pd-Cu) and/or the creation of porous structures inside the packing (for Pd-Cu). Fresh Pd-Cu appears to be a better catalyst than fresh Pd as indicated by the initial rates of reaction observed for each material.

CO and $H_2O$, two of the major components present in a post-gasifier stream, were found not to poison the palladium membrane with regard to the permeation of hydrogen at the very high-temperature of this study.

The performance of a membrane reactor is governed by the kinetics and the permeation rate. Therefore, two different membrane reactor configurations were studied, namely a high-reaction rate / low permeation rate and a high-permeation rate / low reaction rate membrane reactor. The former featured a relatively small, thick Pd-membrane within an Inconel®600 reactor and the latter a thin, long Pd-tube. It was found that both configurations suffice to obtain conversions in excess of the equilibrium limitation. The Hydrogen Recovery Factor is significantly larger in the Pd-tube membrane reactor. However, if the available membrane area is used as a base for comparison, the performance of the Pd/Inconel membrane reactor is better. Side-reactions on the Inconel walls are significant and have to be addressed, however. The heat released by the reaction in the Pd-tube membrane reactor appears to have a significant effect on the reaction conversions. This effect needs to be further studied.

## 6.2 OUTLOOK

The strong catalytic effect of the Inconel®600 walls on the WGSR has a large potential if the side-reactions can be minimized. Ways to accomplish this should be explored. In particular, investigating alloys with high chromium and low nickel content may be valuable. Such alloys would combine the suspected catalytic effect of chromium for the WGSR while minimizing the catalyzing effect of nickel on the formation and deposition of carbon. Additionally, alternatives to remove carbon deposited on the surface of the membrane other than oxidation would allow the use of thin membranes in the Pd/Inconel®600 membrane reactor configuration. Finally, the use of a thin Pd membrane (~100 μm) in a Pd/Inconel®600 membrane reactor configuration should be pursued. This configuration would benefit from high reaction and permeation rates.

The suggested effect of the heat transfer coefficient on the performance of the Pd-tube membrane reactor should be validated with experimental measurements and/or detailed simulations. Such simulations should also account for mass-transfer effects on the reaction. Optimum reaction conditions ($CO/H_2O$ ratio, temperature, pressure) could be devised prior to conducting experiments. Further, the membrane reactor configuration can be varied to optimize the surface/volume ratio of the reactor. Finally, Pd-Cu alloys should be explored as membrane reactor materials to determine the viability of the membrane reactor concept in the presence of sulfur-laden streams.

# APPENDIX A COMPUTATIONAL FLUID DYNAMICS NUMERICAL SIMULATIONS

The steady-state flow of the gases through the empty quartz reactor used in this study was modeled using Computational Fluid Dynamics (CFD). Similar computations were also performed for the reactors described by Graven and Long[49], Tingey[50], and Kochubei and Moin[51]. The objective of these computations was to determine whether the reactor geometry could have influenced the kinetic results. Mixing within the reactor was assessed using residence time distribution plots that were determined by simulating the effluent concentration of a gas (hydrogen) that was pulsed into the feed stream (nitrogen). Additionally, the rWGSR was modeled in each reactor under the same conditions of temperature, pressure, residence time, and rate constant expression to elucidate the effect of the non-ideal flow on the kinetic results. A commercial CFD software package (Fluent, 2003), was used for all the numerical simulations.

## A.1 FLOW FIELD

The geometries were generated and meshed by using Gambit 2.0 software (Fluent). Axisymmetric two-dimensional geometries that incorporated a mesh of quads were used for the quartz reactor used in this project and the Tingey[50] reactor. Three-dimensional geometries that incorporated a mesh of hexahedral/tetrahedral hybrid grids were used for the Graven and Long[49]

reactor and the Kochubei and Moin[51] reactor. Finer grids were applied at the reactor inlet, reactor outlet and near the reactor walls in all cases.

The governing equations that were solved in order to describe the flow of gas through the isothermal reactors consisted of the continuity equation and the Navier-Stokes equations. The continuity equation can be expressed in the following form:

$$\frac{\partial \rho}{\partial t} + \nabla.\left(\rho \vec{v}\right) = 0 \qquad \text{(A-1)}$$

where $\rho$ is the density, $t$ is time, and $\vec{v}$ is the velocity vector. The conservation of momentum equation is described as:

$$\frac{\partial}{\partial t}(\rho \vec{v}) + \nabla.(\rho \vec{v}\vec{v}) = -\nabla p + \nabla.(\bar{\bar{\tau}}) \qquad \text{(A-2)}$$

where $p$ is the pressure and $\bar{\bar{\tau}}$ is the stress tensor given by

$$\bar{\bar{\tau}} = \mu\left[(\nabla \vec{v} + \nabla \vec{v}^{T}) - \frac{2}{3}\nabla.\vec{v}I\right] \qquad \text{(A-3)}$$

where $\mu$ is the molecular viscosity, $I$ is the unit tensor, the superscript T means transposed matrix, and the second term on the right hand side is the effect of volume dilation. Because the flow is laminar in the reactors, no turbulence model has been included.

For steady-state calculations, the time derivative terms vanished. The governing equations were discretized by using a control-volume technique in which the algebraic equations were integrated on each control volume yielding discrete equations that conserved each quantity on a control-volume basis. Second order upwind schemes were used for spatial discretizations. The solutions were converged quickly and the residuals were kept under 1.0E-06.

## A.2 SIMULATION OF A TRACER INPUT

This simulation is an unsteady-state calculation, therefore time derivative terms were included. A first order implicit method was applied to discretize the governing equations. In this simulation, the species transport scalar equations were solved in order to trace the evolution of the species. The species transport scalar equation can be written in the following form:

$$\frac{\partial}{\partial t}(\rho Y_i) + \nabla.(\rho \vec{v} Y_{i)} = -\nabla.\vec{J}_i + R_i + S_i \qquad \text{(A-4)}$$

where $Y_i$ is the local mass fraction of species $i$, $\vec{J}_i$ is the diffusion flux of species $i$, $R_i$ is the net rate of production of species $i$ by chemical reaction, and $S_i$ is the rate of reaction by addition from the dispersed phase plus any user-defined source.

The diffusion flux of species $i$ was formulated as:

$$\vec{J}_i = \rho D_{i,m} \nabla Y_i \tag{A-5}$$

where $D_{i,m}$ is the diffusion coefficient for species $i$.

The two components used in the tracer simulation were non-reactive, therefore the last two terms in the species transport equation, Equation (A-4), were neglected. The flow rate at the inlet of the reactor was calculated corresponding to a residence time of 0.5 s. The inlet conditions were specified as to simulate a pulse of hydrogen into a stream of nitrogen flowing to the reactor:

$t \leq 0$ s and $t > 0.01$ s, only $N_2$ flows into the reactor.

$0 < t \leq 0.01$ s, a pulse of dilute $H_2$ (mole fraction = 0.01) is introduced.

## A.3 SIMULATION OF THE CONVERSIONS INSIDE THE REACTOR

When reactions are involved, the net source of chemical species $i$ due to reaction $R_i$ in the species transport scalar equation can be computed as the sum of the reaction source over the $N_R$ reactions that the species participate in:

$$R_i = M_{w,i} \sum_{r=1}^{N_R} \hat{R}_{i,r} \tag{A-6}$$

where $M_{w,i}$ is the molecular weight of species $i$ , $N_R$ is the number of the reactions, and $\hat{R}_{i,r}$ is the molar rate of creation/destruction of species $i$ in reaction.

The molar rate of creation/destruction of species $i$ in reaction $r$ is given by

$$\hat{R}_{i,r} = (\nu''_{i,r} - \nu'_{i,r})(k_{f,r}\prod_{j=1}^{N_r}\left[C_{j,r}\right]^{\eta'_{j,r}} - k_{b,r}\prod_{j=1}^{N_r}\left[C_{j,r}\right]^{\eta''_{j,r}} \qquad \text{(A-7)}$$

where

$\nu'_{i,r}$ = stoichiometric coefficient for reactant $i$ in reaction $r$

$\nu''_{i,r}$ = stoichiometric coefficient for product $i$ in reaction $r$

$N_r$ = number of chemical species in reaction $r$

$C_{j,r}$ = molar concentration of reactant and product species $j$ in reaction $r$ (kgmol/m$^3$)

$\eta'_{j,r}$ = forward rate exponent for each reactant and product species $j$ in reaction $r$

$\eta''_{j,r}$ = backward rate exponent for each reactant and product species $j$ in reaction $r$

For the low conversions observed in this study, the rate of reaction can be expressed as Equation (2-7). The parameters for the rate constant, Equation (2-8), were evaluated by determining the temperature dependence of Equation (2-6) using values available from the up-dated and comprehensive kinetic GRI database[58] for each of the elementary reactions. The

resultant parameters were $k_0$ = 3.52E+11 $(m^3/mol)^{0.5}$ $s^{-1}$ and $E_a$ = 3.27E+05 (J/mol). The residence time was set at 0.5 second for a stoichiometric feed of hydrogen and carbon dioxide.

# APPENDIX B SIMULATION OF THE GAS-PHASE WGSR TUBULAR REACTORS – MEMBRANE AND HEAT TRANSFER EFFECTS

## B.1 THE HIGH-TEMPERATURE, HIGH-PRESSURE GAS-PHASE WGSR IN A TUBULAR MEMBRANE REACTOR

The gas-phase WGSR was modeled in a tubular membrane reactor with a thin, unsupported Pd membrane. The reaction was assumed to take place inside the tube while the hydrogen permeated through the membrane was removed by a sweep gas flowing in the shell side. Three different cases were considered, namely, a very large sweep flow rate (i.e., a zero partial pressure of hydrogen in the sweep side), counter-current, and co-current flow of the sweep gas. The basic assumptions of the model are as follows,

- Tube side performs like an isothermal PFR.
- Laminar regime (this assumption is consistent with the flow capabilities of the system).
- One-dimensional model.
- Steady State (i.e. flux through the mass transfer boundary layer is equal to the flux through the membrane).

- Mass transfer resistance, if any, is concentrated in the boundary layer in the tube side (sweep gas flow rate can be varied at ease).
- Infinite membrane selectivity (i.e. only hydrogen diffuses through the membrane); transport through the membrane is *diffusion-limited*.
- Gas-phase kinetics described by using Equation (3-10); catalytic effects of the membrane can be accounted for by increasing the rate constant in the gas-phase rate expression (for qualitative estimations).

The change in concentrations in the reaction side depends on the rate of reaction and, for hydrogen, on the rate of permeation through the membrane. Therefore, a system of five ODE was written to describe the concentration of CO, $H_2O$, $CO_2$, and $H_2$ in the reaction side, and the concentration of $H_2$ in the permeation side as a function of reactor lenght. Numerical solution was accomplished with MatLab®. Equations used in the model are included below.

- Tube side – gas-phase reaction and diffusion of hydrogen through the membrane:

$$\begin{aligned} u_z \frac{dP_{H2}}{dz} - r_{H2} - J_{H2} &= 0 \\ u_z \frac{dP_{CO2}}{dz} - r_{H2} &= 0 \\ u_z \frac{dP_{CO}}{dz} + r_{H2} &= 0 \\ u_z \frac{dP_{H2O}}{dz} + r_{H2} &= 0 \end{aligned} \qquad \text{(B-1)}$$

Where,

$u_z$ = linear velocity in the tube side (m/s)

$P_i$ = partial pressure of component i (tube side), (Pa)

$z$ = axial coordinate (m)

$r_{H2}$ = rate of reaction (mol $m^{-3}$ $s^{-1}$)

$J_{H2}$ = flux of hydrogen through the membrane (mol $m^{-2}$ $s^{-1}$)

- Tube side - hydrogen flux through the boundary layer:

$$J_{H2BL} = \frac{Kmass}{RT}(P_{H2bulktube} - P_{H2wall})$$
$$J_{H2BL} = J_{H2membrane} \qquad \text{(B-2)}$$

Where,

$K_{mass}$ = Mass transfer coefficient (m/s), determined from the Chilton-Colburn analogy[98]

$J_{H2BL}$ = Hydrogen flux from the bulk to the membrane surface (mol $m^{-2}$ $s^{-1}$)

$J_{H2membrane}$ = Hydrogen flux through the membrane (mol $m^{-2}$ $s^{-1}$)

$P_{H2bulktube}$ = Hydrogen partial pressure away from the surface (bulk) (Pa)

$P_{H2wall}$ = Hydrogen partial pressure on the surface (tube side) (Pa)

$P_{H2bulktube}$ and $J_{H2membrane}$ correspond to $P_{H2}$ and $J_{H2}$ in Equation (B-1), respectively.

- Membrane – diffusion of hydrogen through the membrane:

$$J_{H2} = \frac{K_{diffusion}}{l}(P_{H2in}^{0.5} - P_{H2out}^{0.5}) \quad \text{(B-3)}$$

Where,

$K_{diffusion}$ = Permeability hydrogen in Pd (mol $m^{-1}$ $s^{-1}$ $Pa^{-0.5}$)

$l$ = membrane thickness (m)

$P_{H2in}$ = Hydrogen partial pressure on the membrane surface (tube side) (Pa)

$P_{H2out}$ = Hydrogen partial pressure on the membrane surface (sweep side) (Pa)

$P_{H2in}$ corresponds to $P_{H2wall}$ in Equation (B-2).

- Sweep side – diffusion of hydrogen from the membrane:

$$u_{z,shell}\frac{dP_{H2,shell}}{dz} + J_{H2} = 0 \quad \text{(B-4)}$$

Where,

$u_{zshell}$ = linear velocity in the shell side (m/s)

$P_{H2,shell}$ = partial pressure of $H_2$ (shell side), (Pa)

$J_{H2}$ = flux of hydrogen through the membrane (mol $m^{-2}$ $s^{-1}$)

## B.2 HEAT TRANSFER EFFECTS IN A TUBULAR REACTOR WITHOUT A MEMBRANE

The WGSR is slightly exothermic. A temperature rise should be expected at large conversions if the heat of reaction is not efficiently removed. The increase in temperature will translate into a further increase in the reaction rate. Although the larger reaction rate would be desirable so to minimize the reactor volume in a conventional reactor, the decrease in equilibrium conversion would eventually result into lower conversions than if the reaction were carried out isothermally. On the contrary, the temperature rise would favor the operation of a membrane reactor provided the final temperature does not exceed the capabilities of the membrane itself. Therefore, a simple model to evaluate the temperature increase in a tubular, non-membrane reactor was written. The model was not intended to provide a detailed quantitative description of the experiments. Rather, the effect of the relevant parameters (i.e. overall heat transfer coefficient) on the performance of the traditional reactor would permit to gain some insight on the expected behavior of the membrane reactor.

The reactor was modeled as a PFR inside a larger tube, i.e. a tube-and-shell heat exchanger configuration. The temperature of the bulk of the stream flowing in the shell was considered to be constant, what seems to be supported for the significantly larger sweep flow rate used in the experiments. Therefore, only the temperature inside the reactor was modeled. In addition, equal molar feed inlet was assumed which allows a simplification of Equation (3-10).

Heat transfer effects were accounted by the introduction of the overall heat transfer coefficient. The heat transfer balance (Equation (B-5)) must be solved simultaneously with the

mass balance (Equation (B-6)) balance to account for the interplay between reactor temperature, reaction rate, and conversion[55].

$$\frac{dT}{dV} = \frac{Ua(Ta - T) + (-ra)(-\Delta H)}{F_{A0}(\overline{C}_{pA} + x\Delta Cp)} \qquad \text{(B-5)}$$

$$\frac{dx}{dV} = \frac{1}{F_{A0}}( - kC_{A0}{}^{3/2}(1 - x)^{3/2})(\frac{To}{T})^{3/2}(1 - \beta) \qquad \text{(B-6)}$$

Where,

$T$ = reactor temperature (K)

$x$ = conversion

$C_{A0}$ = inlet concentration of CO (or $H_2O$), mol/$m^3$

$F_{A0}$ = inlet molar flow rate of CO (or $H_2O$), mol/s

$C_{pA}$ = average heat capacity reactant inlet (J $mol^{-1}$ $K^{-1}$)

$\Delta C_p$ = combined heat capacity reactant mixture (J $mol^{-1}$ $K^{-1}$)

$T_0$ = inlet reactor temperature (K)

$T_a$ = temperature outside reactor (K)

$Ua$ = overall heat transfer coefficient per unit volume (J $m^{-3}$ $s^{-1}$ $K^{-1}$)

$k$ = rate constant ($m^{-3}$ mol)$^{0.5}$ $s^{-1}$

$ra$ = reaction rate (mol $m^{-3}$ $s^{-1}$)

$\Delta H$ = heat of reaction (J/mol)

$(1-\beta)$ = approach-to-equilibrium factor (Equation (3-11))

## BIBLIOGRAPHY


1. Collot, A.G., "Prospects for Hydrogen from Coal," The Clean Coal Centre, IEA Coal Research, March 2004.

2. National Vision of America's Transition to a Hydrogen Economy – To 2030 and Beyond," U.S. Department of Energy, February 2002.

3. Ogden, J., "Hydrogen Energy Systems Studies," Center for Energy and Environmental Studies, Princeton University, 1999.

4. Armor, J., "The Multiple Roles for Catalysis in the Production of $H_2$," Applied Catalysis A, Vol. 176, No. 2 (1999), pp. 159-176.

5. Srivastava, R., and H. McIlvried, "Hydrogen Production Review of Available Technologies," Burns and Roe Services Corporation. Report to DOE, Contract DE-AC22-94PC92100 (1996).

6. Czuppon, T.A., S.A. Knez, and D.S. Newsome, "Hydrogen." In: *Encyclopedia of Chemical Technology*, Kirk, R.E., and D.F. Othmer (eds), 4th edition (1995), Vol. 13, pp. 838-894.

7. Maxwell, R., "Gasification Technologies," Presentation to NETL - Hydrogen Separation Team, January 29, 2002

8. Parsons Infrastructure & Technology Group, "Hydrogen Production Facilities – Plant Performance and Cost Comparisons," Final Report to DOE, Contract No. DE-AM26-99FT40465 (2002).

9. Ma, D, and C.R. Lund, "Assessing High-Temperature Water-Gas Shift Membrane Reactors," Industrial and Engineering Chemistry Research, Vol. 42, No. 4 (2003), pp. 711-717.

10. Kreutz, T.G., R.H. Williams, R.H. Socolow, P. Chiesa, and G. Lozza, "Production of Hydrogen and Electricity from Coal with $CO_2$ Capture," 6th International Conference on Greenhouse Gas Control Technologies, September 30-October 4, 2002, Kyoto Japan

11. Steward, S.A. "Review of Hydrogen Isotope Permeability Through Materials," Lawrence Livermore National Laboratory, August 15, 1983.

12. Rothenberger, K.S., A.V. Cugini, B.H. Howard, R.P. Killmeyer, M.V. Ciocco, B.D. Morreale, R.M. Enick, F. Bustamante, I.P. Mardilovich, and Y.H. Ma. "High Pressure Hydrogen Permeance of Porous Stainless Steel Coated with a Thin Palladium Film via Electroless Plating," Journal of Membrane Science, *In press*.

13. Paglieri, S.N., and J.D. Way. "Innovation in Palladium Membrane Research," Separation and Purification Methods, Vol. 31, No. 1 (2002), pp. 1-170.

14. Rothenberger, K.S., B.H. Howard, R.P. Killmeyer, A.V. Cugini, R.M. Enick, F. Bustamante, M.V. Ciocco, and B.D. Morreale. "Evaluation of Tantalum-Based Materials for Hydrogen Separation at Elevated Temperatures and Pressures," Journal of Membrane Science, Vol. 218, No. 1-2 (2003), pp. 19-37.

15. Nam, S.E., and K.H. Lee, "Hydrogen Separation by Pd Alloy Composite Membranes: Introduction of Diffusion Barrier," Journal of Membrane Science, Vol. 192, No. 1-2 (2001), pp. 177-185.

16. McBridge, R.B., and D.L. McKinley, "A New Hydrogen Recovery Route," Chemical Engineering Progress, Vol. 61, No. 3 (1965), pp. 81-86.

17. Antonizaai, A.B., A.A. Haasz, and P.C. Strangeby, "The Effect of Adsorbed Carbon and Sulphur on Hydrogen Permeation Through Palladium," Journal of Nuclear Materials, Vol. 162-164 (1989), pp. 1065-1070.

18. Morreale, B.D., M.V. Ciocco, B.H. Howard, R.P. Killmeyer, A.V. Cugini, and R.M. Enick, "Effect of Hydrogen-Sulfide on the Hydrogen Permeance of Palladium-Copper Alloys at Elevated Temperatures," Journal of Membrane Science, *In press*.

19. McKinley, D.L., "Metal Alloy for Hydrogen Separation and Purification," US Patent 3,350,845 (1967).

20. Howard, B.H., R.P. Killmeyer, K.S. Rothenberger, A.V. Cugini, B.D. Morreale, R.M. Enick, and F. Bustamante, "Hydrogen Permeance of Palladium-Copper Alloy Membranes over a Wide Range of Temperatures and Pressures," Journal of Membrane Science, *In press*.

21. Kamakoti P, and D.S. Sholl, "A Comparison of Hydrogen Diffusivities in Pd and CuPd Alloys Using Density Functional Theory," Journal of Membrane Science, Vol. 225, No. 1-2 (2003), pp. 145-154.

22. Alfonso, D., A.V. Cugini, and D.S. Sholl, "Density Functional Theory Studies of Sulfur Binding on Pd, Cu and Ag and Their Alloys," Surface Science, Vol. 546, No. 1 (2003), pp. 12-26.

23. Sanchez Maracano, J. G., and T.T. Tsotsis, "Catalytic Membranes and Membrane Reactors," Wiley-Vch Verlag GmbH, Weinheim, Germany (2002).

24. Knapton, A.G, "Palladium Alloys for Hydrogen Diffusion Membranes – A review of High Permeability Materials," Platinum Metals Review, Vol. 21 (1977), pp. 44-55.

25. Grashoff, G.J., C.E. Pilkington, and C.W Corti, "The Purification of Hydrogen - A Review of the Technology Emphasizing the Current Status of Palladium Membrane Diffusion," Platinum Metals Review, Vol. 27, No. 4 (1983), pp. 157-165.

26. Gryaznov, V. "Membrane Catalysis," Catalysis Today, Vol. 51, No. 3-4 (1999), pp. 391-395.

27. Oklany, J.S., H. Hou, and R. Hughes, "A simulative comparison of dense and microporous membrane reactors for the steam reforming of methane," Applied Catalysis A, Vol. 170, No. 1 (1998), pp. 13-22.

28. Li, A., W. Liang, and R. Hughes, "The Effect of Carbon Monoxide and Steam on the Hydrogen Permeability of a Pd/Stainless Steel Membrane," Journal of Membrane Science, Vol. 165, No. 1 (2000), pp. 135-141.

29. Amandusson, H., L.G. Ekedahl, and H. Dannetun, "The effect of CO and $O_2$ on Hydrogen Permeation Through a Palladium Membrane," Applied Surface Science, Vol. 153, No. 4 (2000), pp. 259-267.

30. Amano, M., C. Nishimura, and M. Komaki, "Effects of High Concentration of CO and $CO_2$ on Hydrogen Permeation Through the Palladium Membrane," Materials Transactions JIM, Vol. 31, No. 5 (1990), p. 404.

31. Saracco, G., and V. Specchia, "Catalytic Inorganic-Membrane Reactors: Present Experience and Future Opportunities," Catalysis Reviews: Science and Engineering , Vol. 36, No. 2 (1994), pp. 305-384.

32. Julbe, A., D. Farrusseng, and C. Guizard, "Porous Ceramic Membranes for Catalytic Reactors – Overview and New Ideas," Journal of Membrane Science, Vol. 181, No. 1 (2001), pp. 3-20.

33. Saracco, G., H. Neogamus, C. Versteeg, and W. Van Swaaij, "High-Temperature Membrane Reactors: Potential and Problems," Chemical Engineering Science, Vol. 54, No. 13 (1999), pp. 1997-2017.

34. Shu, J., B. Grandjean, A. Van Neste, and S. Kaliaguine, "Catalytic Palladium-Based Membrane Reactors: A Review," Canadian Journal of Chemical Engineering, Vol. 69, No. 5 (1991), pp. 1036-1060.

35. Kikuchi, E., S. Uemiya, N. Sato, H. Inoue, H. Ando, and T. Matsuda, "Membrane Reactor Using Microporous Glass-Supported Thin Film of Palladium. 1) Application to the Water-Gas Shift Reaction," Chemistry Letters, (1989), p. 489.

36. Uemiya, S., N. Sato, H. Ando, and E. Kikuchi, "The Water-Gas Shift Reaction Assisted by a Palladium Membrane Reactor," Industrial and Engineering Chemistry Research, Vol. 30, No. 3 (1991), pp. 585-589.

37. Basile, A., E. Drioli, F. Santella, V. Violante, G. Capannelli, and G. Vitulli, "A Study on Catalytic Membrane Reactors for the Water-Gas Shift Reaction," Gas Separation and Purification, Vol. 10, No. 1 (1996), 53-61.

38. Basile, A., A. Criscuoli, F. Santella, and E. Drioli, "Membrane Reactor for Water-Gas Shift Reaction," Gas Separation and Purification, Vol. 10, No. 4 (1996), 243-254.

39. Criscuoli, A., A. Basile, and E. Drioli, "An Analysis of the Performance of Membrane Reactors for the Water-Gas Shift Reaction Using Gas Feed Mixtures," Catalysis Today, Vol. 56, No. 1-3 (2000), pp. 53-64.

40. Basile, A., G. Chiappetta, S. Tosti, and V. Violante, "Experimental and Simulation of Both Pd and Pd/Ag for a Water-Gas Shift Membrane Reactor," Separation and Purification Technology, Vol. 25, No. 103 (2001), pp. 549-571.

41. Damle, A., S. Ganwal, and V. Venkataram, "A Simple Model for a Water-Gas Shift Membrane Reactor," Gas Separation and Purification, Vol. 8, No. 2 (1994), pp. 101-106.

42. Newsome, D. "The Water-Gas Shift Reaction," Catalysis Reviews: Science and Engineering, Vol. 21, No. 2 (1980), pp. 275-381.

43. Helling, R.K., and J.W. Tester, "Oxidation Kinetics of Carbon Monoxide in Supercritical Water," Energy & Fuels, Vol. 1, No. 5 (1987), pp. 417-423.

44. Holgate, R.H., P.A. Webley, J.W. Tester, and R.K. Helling, "Carbon Monoxide Oxidation in Supercritical Water: The Effects of Heat Transfer and the Water-Gas Shift Reaction on Observed Kinetics," Energy & Fuels, Vol. 6 No. 5 (1992), pp. 586-597.

45. Holgate, H.R., and J.W. Tester, "Oxidation of Hydrogen and Carbon Monoxide in Sub- and Supercritical Water: Reaction Kinetics, Pathways, and Water-Density Effects. 1. Experimental Results," Journal of Physical Chemistry, Vol. 98, No. 3 (1994), pp. 800-809.

46. Holgate, H.R., and J.W. Tester, "Oxidation of Hydrogen and Carbon Monoxide in Sub- and Supercritical Water: Reaction Kinetics, Pathways, and Water-Density Effects. 2. Elementary Reaction Modeling," Journal of Physical Chemistry, Vol. 98, No. 3 (1994), pp. 810-822.

47. Rice, S.F., R.S. Steeper, and J.D. Aiken, "Water-Density Effects on Homogeneous Water-Gas Shift Reaction Kinetics," Journal of Physical Chemistry A, Vol. 102, No. 16 (1998), pp. 2673-2678.

48. Bradford, B.W., "The Water-Gas Reaction in Low-pressure Explosions," Journal of the Chemical Society, (1933), p. 1557.

49. Graven, W., and J. Long, "Kinetics and Mechanisms of the Two Opposing Reactions of the Equilibrium $CO + H_2O = CO_2 + H_2$," Journal of the American Chemical Society, Vol. 76 (1954), pp. 2602-2607, 6421.

50. Tingey, G., "Kinetics of the Water-Gas Equilibrium Reaction. I. The Reaction of Carbon Dioxide with Hydrogen," Journal of Physical Chemistry, Vol. 70, No. 5 (1966), pp. 1406-1412.

51. Kochubei, V., and F. Moin, "Kinetics of the Reaction of $CO_2$ with Hydrogen," Kinetika i Kataliz, Vol. 10 (1969), p. 1203.

52. Karim, G.A., and D. Mohindra, "A Kinetic Investigation of the Water-Gas Shift Reaction in Homogeneous Systems," Journal of the Institute of Fuel, (Dec. 1974), p. 219.

53. Hadman,, G., H.W. Thompson, and C.N. Hinshelwood, "The Oxidation of Carbon Monoxide," Proceedings of the Royal Society of London – Series A, Vol. 137, No. 831 (1932), pp. 87-101.

54. Long, F.J., and K.W. Sykes, "The Catalysis of the Carbon Monoxide-Steam Reaction," Proceedings of the Royal Society of London – Series A, Vol. 215, No. 1120 (1952), pp. 111-119.

55. Fogler, H.S., "Elements of Chemical Reaction Engineering," 3rd ed., Prentice Hall, Upper Saddle River (1997).

56. Morreale, B.D., M.V. Ciocco, R.M. Enick, B.I. Morsi, B.H. Howard, A.V. Cugini, and K.S Rothenberger, "The permeability of Hydrogen in Bulk Palladium at Elevated Temperatures and Pressures," Journal of Membrane Science, Vol. 212, No. 1-2 (2003), pp. 87-97.

57. Ward, T., and T. Dao, "Model of Hydrogen Permeation Behavior in Palladium Membranes," Journal of Membrane Science, Vol. 153, No. 2 (1999), pp. 211-231.

58. GRI-Mech 3.0, *http://www.me.berkeley.edu/gri_mech/* (2000).

59. Baulch, D.L., C.J. Cobos, R.A. Cox, C. Esser, P, Frank, Th. Just, J.A. Kerr, M.J. Pilling, J. Tore, R.W. Walker, and J. Warnatz, "Evaluated Kinetic Data for Combustion Modelling," Journal of Physical and Chemical Reference Data, Vol. 21 No. 3 (1992), pp. 411-734.

60. Tsang W., and R.F. Hampson, "Chemical Kinetic Data Base for Combustion Chemistry. Part I. Methane and Related Compounds," Journal of Physical and Chemical Reference Data, Vol. 15 No. 3 (1987), p. 1087.

61. Singh, C.P., and D.N. Saraf, "Simulation of High-Temperature Water-Gas Shift Reactors," Industrial and Engineering Process Design and Development, Vol. 16, No. 3 (1977), pp. 313-319.

62. Biermann, H.W., C. Zetzsch, and F. Stuhl, "On the Pressure Dependence of the Reaction of OH with CO," Ber. Bunsenges. Phys. Chem., Vol. 82 (1978), p. 633.

63. Fulle, D., H.F. Hamann, H. Hippler, and J. Troe, "High Pressure Range of Addition Reactions of OH. II. Temperature and Pressure Dependence of the Reaction HO + CO $\leftrightarrow$ HOCO $\rightarrow$ H+ $CO_2$," Journal of Chemical Physics, Vol. 105 (1996), pp. 983-1000.

64. Troe, J., "Modeling the Temperature and Pressure Dependence of the Reaction HO + CO $\leftrightarrow$ HOCO $\leftrightarrow$ H+ $CO_2$," Symposium International on Combustion, The Combustion Institute, (1998), p. 167.

65. Aghalayam, P., P. Bui, and D. Vlachos, "The Role of Radical Wall Quenching in Flame Stability and Wall Heat Flux: Hydrogen-Air Mixtures," Combustion Theory and Modelling, Vol. 2, No. 4 (1998), pp.515-530.

66. Ingles, O.G., "The Water Gas Shift Reaction in Fuel Systems. Part 1. The Water Gas Shift Reaction on Carbon," Transactions of the Faraday Society, Vol. 48 (1952), p. 706.

67. Kondratjev, V., and M. Ziskin, "On the Reaction of Water Gas Conversion in Quartz Vessels," Acta Physicochimica, Vol. 18 (1943), p. 197.

68. Long, F.J., and K.W. Sykes. "The Mechanism of the Steam-Carbon Reaction," Proceedings of the Royal Society of London – Series A, Vol. 193, No. 1034 (1948), pp. 377-399.

69. Zhu, Z.H., J. Finnerty, G.Q. Lu, M.A. Wilson, and R.T. Yang, "Molecular Orbital Theory Calculations of the $H_2O$-Carbon Reaction," Energy & Fuels, Vol. 16, No. 4 (2002), pp. 847-854.

70. Ridler, D.E. and M.V. Twig, "Steam Reforming." In: *Catalyst Handbook*, 2nd ed. M.V. Twig, ed., (1996).

71. Miksa, D., and T. Brill, "Spectroscopy of Hydrothermal Reactions 17. Kinetics of the Surface-Catalyzed Water-Gas Shift Reaction with Inadvertent formation of $Ni(CO)_4$," Industrial and Engineering Chemistry Research, Vol. 40, No. 14 (2001), pp. 3098-3103.

72. Sykes, M.L., I.A.S. Edwards, and K.M. Thomas, "Metal Carbonyl Decomposition and Carbon Deposition in the Advanced Gas-Cooled Nuclear Reactor," Carbon, Vol. 31, No. 3 (1993), pp. 467-472.

73. Figuereido, J.L., and D.L. Trimm, "Gasification of Carbon Deposits on Nickel Catalysts," Journal of Catalysis, Vol. 40, No. 2 (1975), p. 154-159.

74. Klower, J., H.J. Grabke, and E.M. Muller-Lorenz, "Metal Dusting of Nickel-Base Alloys," Materials and Corrosion, Vol. 49 (1998), p. 328.

75. Baker, B.A., G.D. Smith, and S.A. McCoy, "Selection of Nickel-Base Alloys for Metal Dusting Resistance," Ammonia Technical Manual, (2002), p. 257.

76. King, P.J., and D.M. Doyle, "High Temperature Gaseous Oxidation for Passivation of Austenitic Alloys," US Patent 6,488,783 (2002).

77. Bunluesin T., R.J. Gorte, and G.W. Graham, "Studies of the Water-Gas-Shift Reaction on Ceria-Supported Pt, Pd, and Rh: Implications for Oxygen-storage Properties," Applied Catalysis B, Vol. 15, No. 1-2 (1998), pp. 107-114.

78. Voogt, E.H., A.J.M. Mens, O.L.J. Gijzeman, and J.W. Geus, "Adsorption of Oxygen and Surface Oxide Formation on Pd(111) and Pd Foil Studied with Ellipsometry, LEED, AES and XPS," Surface Science, Vol. 373, No. 2-3 (1997), pp. 210-220.

79. Veser, G., A. Wright, and R. Caretta, "On the Oxidation-Reduction Kinetics of Palladium," Catalysis Letters, Vol. 58, No. 4 (1999), pp.199-206.

80. Wolf, M.M., H. Zhu, W.H. Green, and G. S. Jackson, "Kinetic Model of Polycrystalline Pd/PdOx in Oxidation/Reduction Cycles," Applied Catalysis A, Vol. 244 No. 2 (2003), pp. 323-340.

81. Peuckert, M., "Study on Surface and Bulk Palladium Oxide, its Thermal Stability, and a Comparison with Other Noble Metal Oxides," Journal of Physical Chemistry, Vol. 89, No. 12 (1985), pp. 2481-2486.

82. Aggarwal, S., A.P. Monga, S.R. Perusse, R. Ramesh, V. Ballarotto, E.D. Williams, B.R. Chalamala, Y. Wei, and R.H. Reuss, "Spontaneous Ordering of Oxide Nanostructures," Science, Vol. 287 No. 5461 (2000), pp. 2235-2237.

83. Monteiro R.S., D. Zemylanov, J.S. Storey, and F.H. Ribeiro, "Surface Area Increase on Pd Foils After Oxidation in Excess Methane," Journal of Catalysis, Vol. 201, No. 1 (2001), pp. 37-45.

84. Matolin, V, M. Rebholz, and N. Kruse, "Defect-Induced Dissociation of CO on Palladium," Surface Science, Vol. 245, No. 3 (1991), pp. 233-243.

85. Enick, R.M., A.V. Cugini, R.P. Killmeyer, B.H. Howard, M.V. Morreale, B.F. Ciocco, and F. Bustamante, "Towards the Development of Robust Water-Gas Shift Reactors," ACS Preprints – Fuel Chemistry Division, Vol. 226 (2003), pp. 146-147.

86. Okamoto, H., "Desk Handbook Phase Diagrams for binary Alloys," ASM International (2000).

87. Bickford, E.S., S. Velu, and C. Song., "Ceria-supported Cu-Pd Bimetallic Catalysts for Oxygen-Assisted Water-Gas-Shift Reaction for Proton-Exchange Membrane Fuel Cells," ACS Preprints – Fuel Chemistry Division, Vol. 48 No. 2 (2003), pp. 810-811.

88. Hungria, A.B., A. Iglesias-Juez, A. Martinez-Arias, M. Fernandez-Garcia, J.A. Anderson, J.C. Conesa, and J. Soria, "Effects of Copper on the Catalytic Properties of Bimetallic Pd-Cu(Ce,Zr)$O_x$/$Al_2O_3$ and Pd-Cu(Ce,Zr)$O_x$ Catalysts for CO and NO Elimination," Journal of Catalysis, Vol. 206, No. 2 (2002), pp. 281-294.

89. Fernandez-Garcia, M., J.C. Conesa, A. Clotet, J.M. Ricart, N. Lopez, and F. Illas, "Study of the Heterometallic Bond Nature in PdCu(111) Surfaces," Journal of Physical Chemistry B, Vol. 102, No. 1 (1998), pp. 141-147.

90. Jakdetchai, O., and T. Nakajima, "Mechanism of the Water-Gas Shift Reaction Over Cu(110), Cu(111) and Cu(100) Surfaces: an AM1-d Study," Journal of Molecular Structure (Theochem), Vol. 619 (2002), pp. 51-58.

91. Fishtik, I., and R. Datta, "A UBI-QEP Microkinetic Model for the Water-Gas Shift Reaction on Cu(111)," Surface Science, Vol. 512, No. 3 (2002), pp. 229-254.

92. Wang, G., L. Jiang, Z. Cai, Y. Pan, X. Zhao, W. Huang, K. Xie., Y. Li, Y. Sun, and B. Zhong, "Surface Structure Sensitivity of the Water-Gas Shift Reaction on Cu(hkl) Surfaces: A Theoretical Study," Journal of Physical Chemistry B, Vol. 107, No. 2 (2003), pp. 557-562.

93. Hou, K, and R. Hughes, "Preparation of Thin and Highly Stable Pd/Ag Composite Membranes and Simulative Analysis of Transfer Resistance for Hydrogen Separation," Journal of Membrane Science, Vol. 214, No. 1 (2003), pp. 43-55.

94. Incropera, F.P. and D.P. DeWitt, "Introduction to Heat Transfer," 3rd ed., John Wiley & Sons, New York (1996).

95. Ali, M.E., "Laminar Natural Convection from Constant Heat Flux Helical Coiled Tubes," International Journal of Heat and Mass Transfer, Vol. 41, No. 14 (1998) pp. 2175-2182.

96. Shah, R.K., and S.D. Joshi, "Convective Heat Transfer in Curved Ducts." In: *Handbook of Single-Phase Convective Heat Transfer*, S. Kadac, R. Shah, and W. Aung, eds., Wiley-Interscience, New York (1987).

97. Dietrich, M., R. Blöchl, and H. Müller-Steinhagen, "Heat Transfer for Forced Convection Past Coiled Wires," Journal of Heat Transfer, Vol. 112 (1990), pp. 921-925.

98. Welty, J., C.E. Wicks, and R.E. Wilson, "Fundamentals of Momentum, Heat, and Mass Transfer," 2nd ed., John Wiley & Sons, New York (1976).